5 RESEARCH ACTIVITIES

5.1 NUCLEAR PHYSICS

N. Madhavan

Indian National Gamma Array (INGA) facility, set up once again at IUAC using pooled Clover germanium detectors from various Indian institutes, has been used in several experiments using beams from Pelletron accelerator. With an extended campaign of nearly six months, most of the students' theses related high spin studies using stand-alone INGA have been performed. Some of the physics studies addressed include shape coexistence, magnetic and anti-magnetic rotations, search for chirality, extending high spin data up to band termination, short life-time isomers, etc.

HYbrid Recoil mass Analyzer (HYRA) facility was operated with its first stage in vacuum, momentum achromat mode in an experiment looking for clustering vs. pairing effects in light nuclei. The experiment could be performed successfully by making several crucial changes in the facility and adding 6 neutron detectors at forward angles. Heavy Ion Reaction Analyzer (HIRA) platform has been re-levelled, the beam-line has been modified and sub-barrier fusion experiments have been performed successfully, subsequently.

General Purpose Scattering Chamber (GPSC) was used in experiments measuring fission fragment mass and/or angular distributions and quasi-elastic back-scattering. HYRA and National Array of Neutron Detectors (NAND) will be used to perform students' theses related experiments using Pelletreon + SC-LINAC beams over a period of half year (April to September, 2017). The addition of diagnostic chamber upstream of NAND target location is expected to make the LINAC tuning easier as per the required energy and timing spreads.

Several earlier experimental data have been analysed and published in journals, new proposals have been successfully defended by a number of new as well as existing IUAC users and work is progressing in adding ancillary facilities to enhance the capabilities of existing ones.

During the past year, Ms. Priya Sharma (Research scholar, Panjab University) won one of the best poster awards in "DAE Symposium on Nuclear Physics (2016)" held at SINP, Kolkata for her work using HYRA + TIFR Spin Spectrometer, Dr. Vijay Raj Sharma (RA, IUAC) won the best poster award in "FUSION17" held in Australia for his work on incomplete fusion reactions and Mr. Saneesh (IUAC) won one of the best poster awards in International conference on "Nuclear Physics with Energetic Heavy Ion Beams" held at Panjab University for his work related to NAND facility.

5.1.1 Lifetime measurements of ^{139}Pm

S. S. Tiwary[1], H. P. Sharma[1], S. Chakraborty[1], C. Majumder[1], K. Rojeeta Devi[2], Neelam[2], A. Sharma[3], V. V. Jyoti[4], Mayank[5], N. Ali[6], P. Banerjee[7], A. Kumar[6], S. Kumar[2], S. K. Chamoli[2], S. Ganguly[8], S. Muralithar[9], R. P. Singh[9] and I. Bala[9]

[1]Department of Physics, Institute of Science, Banaras Hindu University, Varanasi 221005, India
[2]Department of Physics and Astrophysics, University of Delhi, Delhi 110007, India
[3]Department of Physics, Himachal Pradesh University, Shimla 171005, India
[4]Department of Nuclear Physics, Andhra University, Visakhapatnam 530003, India
[5]Amity Institute of Nuclear Science and Technology, Amity University, Noida 201313, India
[6]Department of Physics, Panjab University, Chandigarh 160014, India
[7]Saha Institute of Nuclear physics, Block - AF, Sector - 1, Bidhan nagar, Kolkata 700064, India
[8]Department of Physics, Bethune College, 181 Bidhan Sarani, Kolkata 700006, India
[9]Inter University Accelerator Centre, Aruna Asaf Ali Mareg, New Delhi 110067, India

The nuclei which lie near A~140 amu mass region have been the subject of interest in aspects of both theoretical and experimental investigations due to their softness towards triaxial shape. The "Potential Energy Surface" (PES) calculations, in this mass region, predicted a small difference in energy for the prolate and oblate nuclear shapes [1]. The proton (neutron) Fermi surface lie near lower (higher) side of the $h_{11/2}$ sub-shell in these nuclei and, therefore, give rise to opposite, shape driving forces and drive the nuclei to gamma-soft triaxial shape. Hence, these nuclei provide an excellent opportunity to test various theoretical models. In addition, several magnetic rotational (MR) bands were reported, near N ~ 82 shell closure, with $\pi(h_{11/2})^{n}\nu(h_{11/2})^{-n}$ configuration. Systematically, MR bands has been observed in N = 78, ^{135}La, ^{136}Ce, ^{137}Pr, ^{138}Nd, ^{140}Sm, ^{141}Eu, and ^{142}Gd, isotonic nuclei.

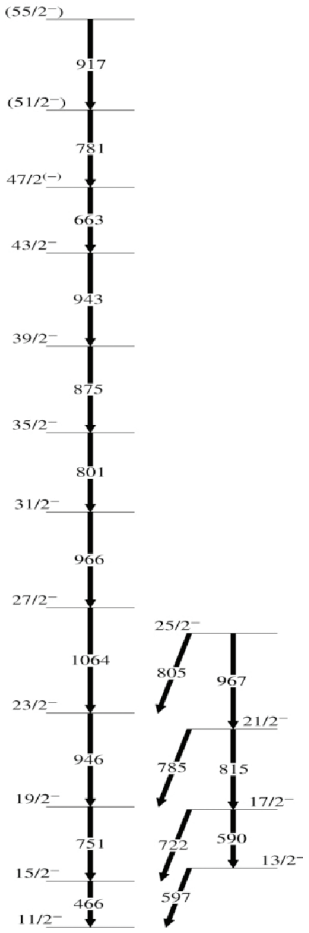

Fig. 5.1.2: Partial Level scheme of ^{139}Pm.

Previously, ^{139}Pm (Z = 61, N = 78) has been studied via same fusion evaporation reaction ^{116}Cd(^{13}Al,4n)^{139}Pm, with two different experimental facilities by Zhang *et al.* [3] and Dhal *et al.* [2] *et al,* respectively. However, placements of several γ-transitions are not in agreement with each other, in these two investigations. Further, two dipole bands, based on $\pi(h_{11/2})^{n}\nu(h_{11/2})^{-n}$ configuration, have been reported. On the basis of systematic TAC calculations [4] these bands were predicted to have Magnetic Rotational behaviour. Hence, in-beam spectroscopic measurements have been carried out, in order to confirm the placements of decaying γ-transitions and existence of MR bands in ^{139}Pm nucleus.

In-beam γ-ray spectroscopy of ^{139}Pm was carried out using the 15UD Pelletron accelerator [5, 6] at IUAC. The high spin states in ^{139}Pm are populated via ^{127}I(^{16}O, ^{4}n) ^{139}Pm fusion-evaporation reaction at E_{beam} = 82 MeV. Eighteen Compton suppressed clover Ge detectors of Indian National Gamma Array (INGA) [7] were used to detect the de-exciting γ-rays. The offline data analysis was done using INGA-SORT [8]. A number of matrices have been formed by sorting the gain-matched, list mode data in order to carry out the coincidence and angular correlation data analysis. In this work, a detailed re-investigation of the low lying levels of ^{139}Pm has been done via fusion evaporation reaction and also RDCO and polarization measurements of several γ-transitions were carried out.

In recent measurements, both online as well as offline calibration (using standard ^{152}Eu source) have been done, in order to extract correct energy and intensity information. The energy calibrated, full projection and the 466 keV energy gated spectrum are shown in Fig. 5.1.1. On the basis of γ-γ coincidence, R_{DCO} and polarization measurements a tentative level scheme of ^{139}Pm has been built, as shown in Fig. 5.1.2. Further analysis for lifetime measurements is under progress.

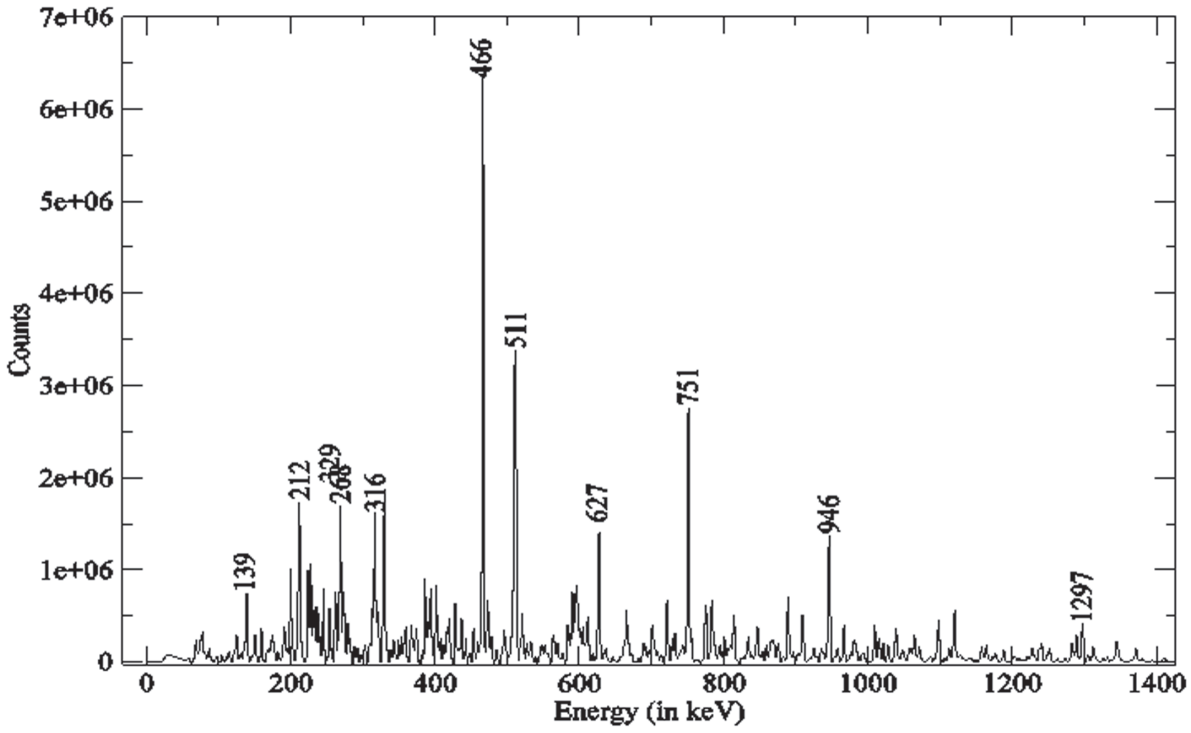

Fig. 5.1.1: Full projection of γ-γ coincidence spectrum ^{139}Pm.

The authors are thankful to all the staff of the target lab, Pelletron accelerator and INGA facilities at Inter University Accelerator Centre, New Delhi. The first author is also thankful to UGC for financial support vide contract no. 23/06/2013(I)EU-V.

REFERENCES

1. I. Ragnarsson et al., Nucl. Phys. A **233,** 329 (1974).
2. A. Dhal et al., Phys. Rev. C **80,** 014320 (2009).
3. N. T. Zhang et al., Phys. Rev. C **84,** 057302 (2011).
4. S. Kumar et al., J. Phys.: Conf. Ser. **413,** 012034 (2013).
5. G. K. Mehta et al., Nucl. Instrum. Meth. A **268,** 334 (1988).
6. D. Kanjilal et al., Nucl. Instrum. Meth. A **328,** 97 (1993).
7. S. Muralithar et al., Nucl. Instrum. Meth. A **622,** 281 (2010).
8. R. K. Bhowmik et al., Proc. DAE Symp. Nucl. Phys. **44B,** 422 (2001).

5.1.2 High spin structure of ^{129}La

K. Rojeeta Devi[1], Naveen Kumar[1], Neelam[1], Neeraj Kumar[1], A. Banerjee[1], C. V. Ahmad[1], Anand Pandey[1], Ravi Bhushan[1], Unnati Gupta[1], Suresh Kumar[1], S. K. Chamoli[1], S. Verma[1], Samit Kr. Mandal[1], R. Garg[2], Indu Bala[2], S. Bhattacharya[2], R. P. Singh[2] , S. Muralithar[2], Pragati[3], Ajay Y. Deo[3], Sutanu Bhattacharyaa[4], T. Trivedi[4], Anupriya Sharma[5], Chandrani Majumder[6], H. P. Sharma[6] and Vishnu Jyoti[7]

[1]Department of Physics and Astrophysics, University of Delhi, Delhi 110007, India
[2]Inter University Accelerator Centre, Aruna Asaf Ali Marg, New Delhi 110067, India
[3]Department of Physics, Indian Institute of Technology, Roorkee 247667, India
[4]Department of Pure and Applied Physics, Guru Ghasidas University, Bilaspur 495009, India
[5]Department of Physics, Banaras Hindu University, Vanarasi 221005 , India
[6]Department of Physics, Himachal Pradesh University, Shimla 171005 , India
[7]Department of Nuclear Physics, Andhra University, Visakhapatnam 530003. India

It is well known that the nuclei in mass A ~ 130 amu region are γ soft. It is already established that the rotational alignment of a pair of $h_{11/2}$ neutrons along the rotation axis gives rise to an oblate shape, whereas, the alignment of a pair of $h_{11/2}$ protons give rise to a prolate shape and introduces shape-coexistence phenomenon. The different shapes and structures observed are determined by the configuration of the valence nucleons and can be discussed in view of different angular momentum coupling. Therefore, in this mass region, different high spin structure phenomena were studied, such as magnetic and antimagnetic rotation, chiral rotation, super-deformation and identical bands. In recent years, multiple bands and degenerate bands were also reported in ^{133}Ce and ^{133}La nuclei. The odd-Z ^{129}La is expected to show these phenomena and makes it an interesting candidate for the present study. For the moderate deformation, the Fermi level of the protons have $g_{7/2,}$ $d_{5/2,}$ $h_{11/2,}$ $s_{1/2,}$ $d_{3/2,}$ single particle orbitals compared to the $d_{5/2,}$ $g_{7/2,}$ $s_{1/2,}$ $d_{3/2,}$ $h_{11/2}$ single particle orbitals for the neutrons. Previously, ^{129}La was studied by using the reaction ^{51}V(^{82}Se, 4*n*)^{129}La. In this study, two strongly coupled bands, namely, band (1,2) and band (8,9), and many dipole bands were established having most of tentative spin and parity assignments. However, many discrepancies between the experimentally observed values and the theoretically predicted values were reported. Therefore, the main aim of the present work is to study the high spin structure of the ^{129}La nucleus by measuring the spin and parity using DCO and polarization measurements.

For this study, an experiment was performed to populate the excited states of ^{129}La through the reaction ^{121}Sb(^{12}C, 4*n*)^{129}La, with a beam energy of 66 MeV which was provided by the 15UD Pelletron at IUAC. The target used was ^{121}Sb, of thickness 900 μg/cm^2 with a backing of 10.0 mg/cm^2 thick ^{197}Au. The γ-rays were detected by using the INGA spectrometer at IUAC which consisted of 18 Compton- suppressed clover detectors with four, four, six, two and two detectors placed at angles 148º, 123º, 90º, 57º and 32º with respect to the beam direction, respectively, at the time of the experiment. The distance between the target position and the detectors was 25 cm. The list mode data were taken in double and higher fold γ-ray coincidence using a computer automated measurement and control based multi-parameter data-acquisition system along with the Collection and Analysis of Nuclear Data using Linux nEtwork (CANDLE) software. A total of about 13×10^7 events were recorded. The symmetric and asymmetric matrices were generated by sorting the data with CANDLE and INGASORT programs.

Total projection spectrum and γ-γ coincidence spectrum gated by the 110 keV, $21/2^+ \rightarrow 19/2^+$ γ-ray transition, are shown in Fig 5.1.3. In the gated spectrum, it is clearly seen that all the transitions up to the highest reported spin are observed. Further, analysis of the data for the DCO and polarization measurements is in progress.

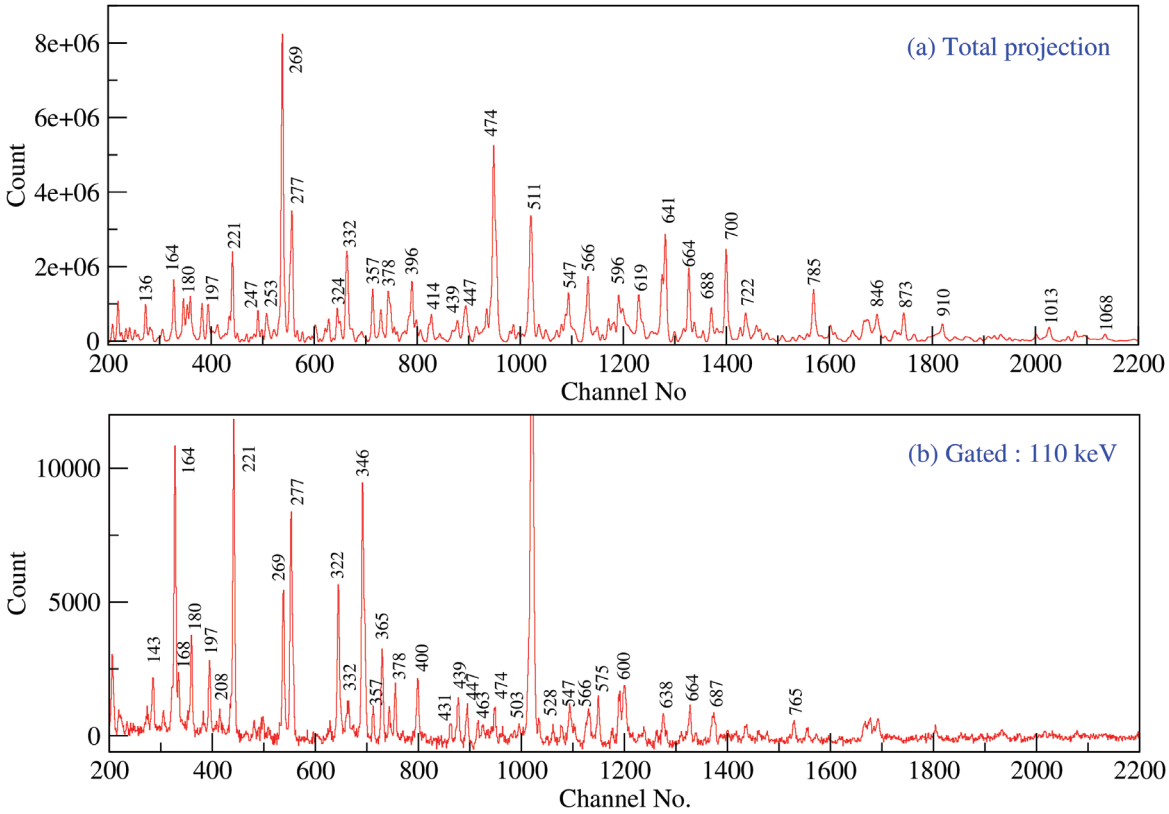

Fig. 5.1.3: (a) Total projection spectrum (b) γ-γ coincidence spectrum gated by the 110 keV, 21/2 → 19/2⁺ γ-ray transition.

References

1. Exotic Nuclear Excitations, S. C. Pancholi, Springer (2010).
2. J. Meng et al., Mod. Phys. Lett. A **23,** 2560 (2008).
3. P. A. Butler, J. Meyer-Ter-Vehn, D. Ward, H. Bertschat et al., Phys. Lett. B **56,** 453 (1975).
4. P. J. Smith, D. J. Unwin, A. Kirwan, D. J. G. Love et al., J. Phys. G: Nucl. Part. Phys, **11** 1271 (1985).
5. Y. He et al., J. Phys. G: Nucl. Part. Phys. **18,** 99 (1992).
6. I. Sankowska et al., Eup. Phys. J. A **37,** 169 (2008).
7. S. Frauendorf and J. Meng, Nucl. Phys. A **617,** 131 (1997).
8. T. Bhattacharja, Pramana – J. Phys. **75,** 25 (2010).
9. S. Muralithar et al., Nucl. Instrum. Meth. A **622,** 281 (2010).
10. S. Muralithar et al., J. Phys.; Conf. Ser. **312,** 052015 (2011).
11. B. P. Ajith Kumar, E. T. Subramanium, K. Rani, and K. Singh, Proc. DAE Symp. Nucl. Phys. **44B,** 390 (2001).
12. R. K. Bhowmik, S. Muralithar and R. P. Singh, Proc. DAE Symp. Nucl. Phys. **44B,** 422 (2001).

5.1.3 High spin states in ^{216}Fr

Pragati[1], A. Y. Deo[1], S. K. Tandel[2], S. S. Bhattacharjee[3], S. Chakraborty[4], S. Rai[5], S. G. Wahid[2], S. Kumar[6], S. Muralithar[3], R. P. Singh[3], Indu Bala[3], Ritika Garg[3], Swati Garg[1], B. Maheshwari[1] and A. K. Jain[1]

[1]Department of Physics, Indian Institute of Technology Roorkee, Roorkee 247667, India
[2]UM-DAE Centre of Excellence in Basic Sciences, Mumbai 400098, India
[3]Inter University Accelerator Centre, Aruna Asaf Ali Marg, New Delhi 110067, India
[4]Department of Physics, Institute of Science, Banaras Hindu University, Varanasi 221005, India
[5]Department of Physics, Visva-Bharati, Santiniketan 731235, India
[6]Department of Physics and Astrophysics, University of Delhi, Delhi 110007, India

Nuclei lying in the trans-lead region are of interest to study the interplay between single particle and collective states, as beyond the $Z = 82$ and $N = 126$ shell closure, nuclear shape changes from spherical to mainly quadrupole or octupole shape. Octupole collectivity is well established around Ra-Th region while nuclei in Fr region are transitional in nature [1, 2]. Debray *et al.,* observed that ^{216}Fr is the lightest nucleus in the transitional region from where the octupole deformation starts [3]. Therefore, it is expected that γ-spectroscopy of ^{216}Fr nucleus ($N = 129$) will provide information about the evolution of deformation in this region.

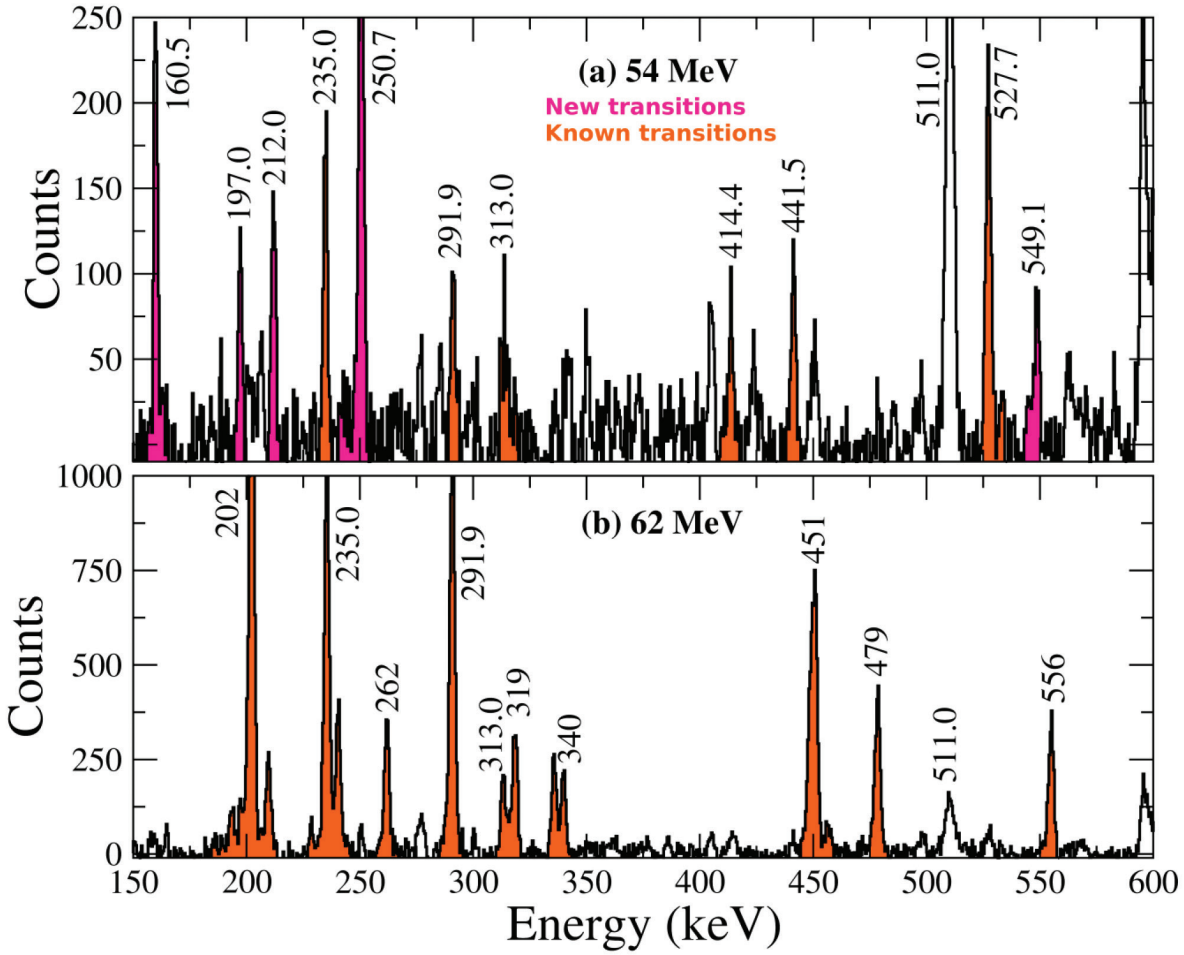

Fig. 5.1.4: Spectra showing transitions at beam energy (a) 54 MeV and (b) 62 MeV.

In the present work, high-spin states in ^{216}Fr nucleus were populated via ^{208}Pb (^{11}B, 3n) reaction. Self-supporting target of thickness ~ 6 mg/cm^2 was impinged with ^{11}B beam in 54−62 MeV energy range, provided by 15UD Pelletron accelerator at IUAC. Gamma rays from the fusion-evaporation reaction were detected using an array of 14 Compton suppressed Clover detectors. The γ-γ coincidence data were acquired using CANDLE [4]. Further, data were sorted into RADWARE [5] compatible γ-γ and γ-γ-γ histograms using a sorting code developed at IIT Roorkee.

Preliminary analysis shows evidence of several new transitions in ^{216}Fr. Fig. 5.1.4(a) displays the γ rays at an incident beam energy of 54 MeV. At this energy, the 3n−evaporation channel leading to ^{216}Fr is dominant and several transitions assigned to this nucleus are visible. With the beam energy at 62 MeV, the 4n−evaporation channel populating ^{215}Fr has the highest cross-section and transitions from this isotope are clearly seen in Fig. 5.1.4(b). Comparison of these spectra, along with the previously established transitions in ^{215}Fr and ^{216}Fr [3, 6], indicates that the 251 and 549 keV γ transitions are new and possibly may be assigned to ^{216}Fr . Moreover, several new γ transitions were observed in coincidence with the 251 keV γ transition as illustrated in Fig. 5.1.5. These transitions have not been reported in the previous work and may form the simplex partner of earlier observed band.

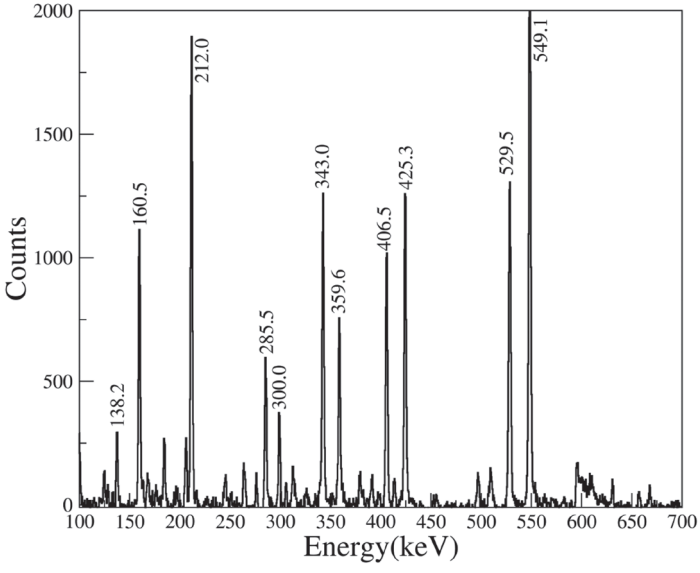

Fig. 5.1.5: Spectra showing transitions in coincidence with 251 keV transition.

Presently, further data analysis using DCO and PDCO matrices is in progress.

References

[1] L .P. Gaffney et al., Nature (London) **497,** 199 (2013).
[2] S. K. Tandel et al., Phys. Rev. C **87,** 034319 (2013).
[3] M. E. Debray et al., Phys. Rev. C **41,** R1895 (1990).
[4] Ajith Kumar B. P. et al., Proc. DAE Symp. Nucl. Phys. **44B,** 390 (2001).
[5] D. C. Radford, Nucl. Instrum. Meth. A **361,** 297 (1995).
[6] M. W. Drigert et al., Phys. Rev. C **32,** 136 (1985).

5.1.4 Barrier distribution for $^{16}O+^{169}Tm$ system through quasi-elastic back-scattering

Abhishek Yadav[1], A. Jhingan[1], M. Kumar[1], N. Saneesh[1], I. Bala[1], K. S. Golda[1], Md. Moin Shaikh[1], T. Banerjee[1], R. Dubey[1], G. Kaur[2], C. Yadav[1], R. N. Sahoo[3], A. Sood[3], H. Arora[4], K. Rani[4], N. K. Rai[5], P. P. Singh[3], M. K. Sharma[6], B. P. Singh[7], P. Sugathan[1] and R. Prasad[7]

[1]Inter University Accelerator Center, New Delhi 110067, India
[2]Department of Physics, Akal University, Talwandi Sabo, Punjab 151302, India
[3]Department of Physics, Indian Institute of Technology Ropar, Roopnagar, Punjab 140001, India
[4]Department of Physics, Panjab University, Chandigarh 202001, Punjab, India
[5]Department of Physics, Institute of Science, Banaras Hindu University, Varanasi 221005, India
[6]Department of Physics, S. V. College, Aligarh 202001, India
[7]Department of Physics, Aligarh Muslim University, Aligrh 202002, India

In recent years, there is a great interest in fusion barrier distribution studies due to the advances in experimental methods and theoretical interpretations [1-7]. The heavy-ion collisions at energies around the Coulomb barrier are strongly affected by the internal structure of colliding nuclei [1-6]. The coupling between relative motion and internal degrees of freedom of colliding ions (such as static deformations, collective excitations; rotation and/or vibration, nucleon transfer, projectile break-up etc.) results in a number of distributed barriers in place of a single potential barrier (B_{fus}). It is now well known that barrier distribution (BD) can be extracted experimentally from the fusion excitation function $\sigma_{fus}(E)$, using the relation $D_{fus}=d^2(E\sigma_{fus})/dE^2$ [3]. The extracted BD can be treated as a fingerprint of the reaction mechanism characterizing the importance of channel couplings because the nature and strengths of the couplings are present in the distribution of barriers. Further, it was suggested that the same information can also be obtained from the cross-section of quasi-elastic back-scattering (QE) (as the total flux is conserved) measured at large angles using the prescription $D_{qel}=-d(d\sigma_{qel}/d\sigma_R)/dE$, which gives an alternative representation of fusion BD [5]. In the present work, the QE-measurements have been performed for the system $^{16}O+^{169}Tm$, which will be translated to BD. It should be noticed that the spherical doubly shell-closed 16O projectile will behave as an inert partner and, therefore, any effect of the coupling of different degrees of freedom on BD should be attributed to the target nucleus only.

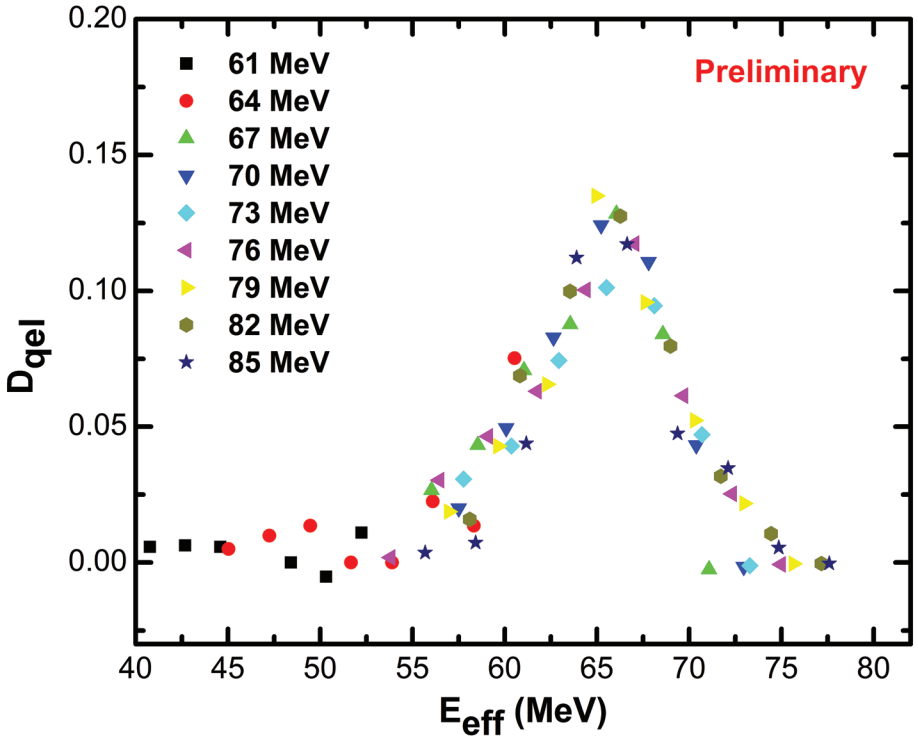

Fig. 5.1.6: Fusion barrier distribution for $^{16}O+^{169}Tm$ system using back-angle QE-scattering.

The experiment was performed at IUAC, New Delhi using HYTAR detector system in GPSC [7]. Beam energy was varied in steps of 3 MeV ranging from 17% below barrier to 16% above barrier. Four telescope detectors each at an angle of 173º were arranged in symmetrical cone geometry to measure the back-scattered quasi-elastic events. Nine telescopes, six at angles from +60º to +160º with angular separation of 20º and three more telescopes at angles -110º, -122º and -134º, were used. Two monitor detectors were placed at ±10º for normalization. The QE-excitation functions have been obtained and the experimental BD for the $^{16}O+^{169}Tm$ system were derived. The nuclear potential parameters will be extracted from angular distribution measurements for theoretical calculations. Further analysis of the experimental data (preliminary results are shown in Fig. 5.1.6) and the theoretical calculations are underway.

REFERENCES

[1] G. Kaur et al., Phys. Rev. C **94,** 034613 (2016).
[2] Md. Moin Shaikh et al., Phys. Rev. C **91,** 034615 (2015).
[3] N. Rowley, G. R. Satchler and P. H. Stelson, Phys. Lett. B **254,** 25 (1991).
[4] M. Dasgupta et al., Annu. Rev. Nucl. Part. Sci. **48,** 401 (1998).
[5] H. Timmers et al., Nucl. Phys. A **584,** 190 (1995).
[6] K. Hagino, N. Rowley, and A. T. Kruppa, Comp. Phys. Commun. **123,** 143 (1999).
[7] A. Jhingan et al., Proc. DAE Symp. Nucl. Phys. **59,** 830 (2014).

5.1.5 Observation of fission-like events in $^{18}O+^{159}Tb$ system at energy ≈ 5.5 AMeV

Abhishek Yadav[1], Pushpendra P. Singh[2], Indu Bala[1], Vijay R. Sharma[1], Mohd. Shuaib[3], D. P. Singh[4], U. Gupta[5], S. Gupta[6], M. K. Sharma[7], R. Kumar[1], S. Muralithar[1], R. P. Singh[1], B. P. Singh[3] and R. Prasad[3]

[1]Inter University Accelerator Centre, New Delhi 110067, India
[2]Department of Physics, Indian Institute of Technology Ropar, Roopnagar, Punjab 140001, India
[3]Department of Physics, Aligarh Muslim University, Aligarh 202002, India
[4]Department of Physics, University of Petroleum and Energy Studies, Dehradun 248007, India
[5]Department of Physics and Astrophysics, Delhi University, Delhi 110007, India
[6]Department of Physics, Agra College, Agra 282001, India
[7]Physics Department, S. V. College, Aligarh 202001, India

Comprehensive understanding of heavy-ion (HI) reaction dynamics at near barrier energies has been a topic of current interest during the last few years [1–6]. Reactions induced by HIs are important, as both the projectile and the target nuclei are heavy thereby involving large input angular momentum. At energies 4-7 MeV/nucleon, complete (CF) and incomplete fusion (ICF) are dominant modes of reactions. It may further be pointed out, that the excited composite system may also undergo fission depending on the available excitation energy, angular momentum, entrance channel mass asymmetry, etc. Nishio *et al.* [1] have also reported that fission of incompletely fused composite nucleus is one of the dominant processes other than fission of the composite system formed via CF at intermediate energies. The experimental data for fusion-fission reactions in HI-interaction is still limited and a comprehensive understanding of HI-induced fission at medium energies is still lacking. In view of the above, experiments have been performed for $^{18}O+^{159}Tb$ system at IUAC using the recoil-catcher activation technique, followed by off-line γ-ray spectroscopy. Our earlier studies of the $^{18}O+^{159}Tb$ system [5,6] indicated that CF and/or ICF are the dominant processes at energies ≈ 5-7 MeV/nucleon. Further analysis of the present system shows the presence of several residues which are not expected to be populated either by CF or ICF processes. Moreover, these residues were found to have charge and atomic mass values around half of the values for the residues produced by CF and/or ICF channels, indicating the possibility of their production through fission of the composite system formed via CF and/or ICF processes. More than 20 fission-like residues ($32 \leq Z \leq 40$) have been identified in $^{18}O+^{159}Tb$ interactions at ≈ 95.57 and 99.16 MeV incident energies. The total production cross-sections for the presently measured fission fragments are found to be ≈ 246 and ≈ 345 mb, at 95.57 and 99.16 MeV, respectively. It may, however, be pointed out that these measured values for the total fission cross-section give only a lower limit (shown by arrows in Fig. 5.1.7) as many fission fragments could not be observed in the present work because either they are stable or having short half-lives.

The authors thank the Director, IUAC for providing all the necessary facilities. One of the authors (A.Y.) sincerely acknowledges Dr. P. Sugathan and Dr. Akhil Jhingan for their support and encouragement. A.Y. also thanks DST for providing financial support through Young-scientist project (ref. number SB/FTP/PS-194/2013).

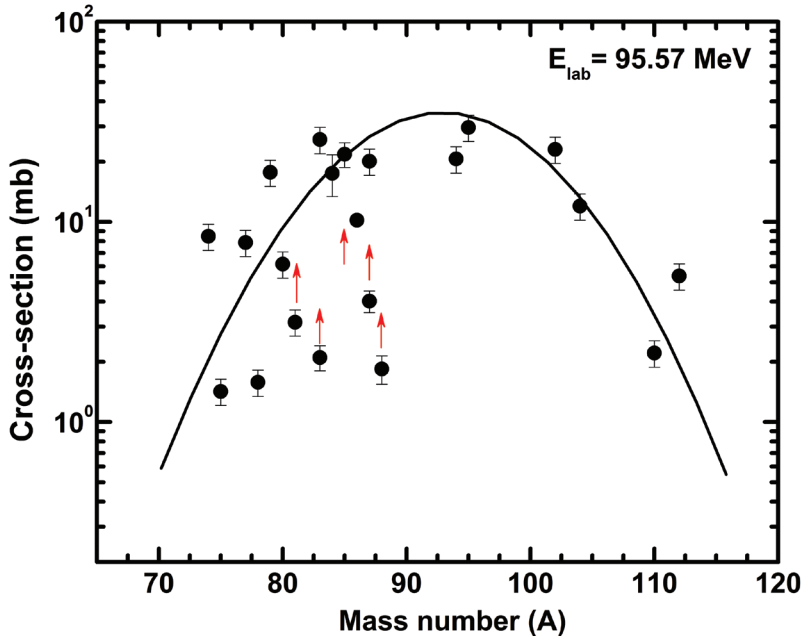

Fig. 5.1.7: Mass distribution of fission products in $^{18}O+^{159}Tb$ reaction at Elab ≈ 95.57 MeV (arrows indicate values expected to go up). The line is drawn through the data points as Gaussian fit.

REFERENCES

1. K. Nishio et al., Phys. Rev. Lett. **93,** 162701 (2004).
2. Pushpendra P. Singh et al., Int. Jour. Mod. Phys. E **17,** 549 (2008).
3. Vijay R. Sharma et al., Phys. Rev. C **84,** 014612 (2011).
4. Abhishek Yadav et al., Phys. Rev C **85,** 034614 (2012); ibid **85,** 064617 (2012).
5. Abhishek Yadav et al., EPJ Web. Conf. **86,** 00064 (2015).
6. Abhishek Yadav et al., EPJ Web. Conf. **117,** 08022 (2016).

5.1.6 Structure of ^{127}Xe at high angular momenta

S. Chakraborty[1], H. P. Sharma[1], S. S. Tiwary[1], C. Majumder[1], S. Rai[2], Pragati[3], Mayank[4], S. S. Bhattacharjee[5], R. P. Singh[5], S. Muralithar[5], P. Banerjee[6], S. Ganguly[7], S. Kumar[8], A. Kumar[9] and R. Palit[10]

[1]Department of Physics, Institute of Science, Banaras Hindu University, Varanasi 221005, India
[2]Department of Physics, Visva-Bharati, Santiniketan 731235, India
[3]Department of Physics, Indian Institute of Technology, Roorkee 247667, India
[4]Amity Institute of Nuclear Science and Technology, Amity University, Noida 201313, India
[5]Nuclear Physics Group, Inter University Accelerator Centre, New Delhi 110067, India
[6]Nuclear Physics Division, Saha Institute of Nuclear Physics, Kolkata 700064, India
[7]Department of Physics, Bethune College, 181 Bidhan Sarani, Kolkata 700006, India
[8]Department of Physics and Astrophysics, University of Delhi, Delhi 110007, India
[9]Department of Physics, Panjab University, Chandigarh 160014, India
[10]Department of Nuclear and Atomic Physics, Tata Institute of Fundamental Research, Mumbai 400005, India

Investigation of the high spin states in odd-A Xe nuclei have been a subject of interest because of the variety of structural features observed at high spin. The ratio of E_{4+} to E_{2+} of even-even Xe nuclei has been found to be close to 2.5, indicating existence of O(6) symmetry (γ-soft rotor) in these nuclei. The Triaxial Rotor plus Particle Model (TRPM) calculations predicted triaxial shape (γ ~ 25º) in odd-A Xe nuclei also [1]. As a consequence of the triaxial shape of odd-A Xe, large signature splitting has been observed in yrast $vh_{11/2}$ band. The signature splitting in yrast $vh_{11/2}$ band have been found to be small but inverted [2]. The explanation in favour of this signature inversion in yrast bands is not yet clear.

The high-spin structure of Xe isotopes have been studied in detail up to A=125 [3], but the structural information of ^{127}Xe is limited only up to low spin [4]. Therefore, in-beam γ-ray spectroscopy of ^{127}Xe has been carried out in order to infer the structure of this nucleus at high spin.

Excited states of ^{127}Xe were populated via ^{122}Sn(^{9}Be, 4nγ) fusion evaporation reaction at a beam energy of 48 MeV, delivered by the 15UD Pelletron accelerator of IUAC. A 8.4 mg/cm^2 thick, isotopically enriched (99.3%), ^{122}Sn foil was used as the target. INGA, an anti-Compton γ-detector array, was used to collect the

two- and higher-fold γ-γ-coincident events. Offline data analysis was carried out using INGASORT and RadWare computer codes. Details of the experimental set up and data analysis are available in Ref. [5].

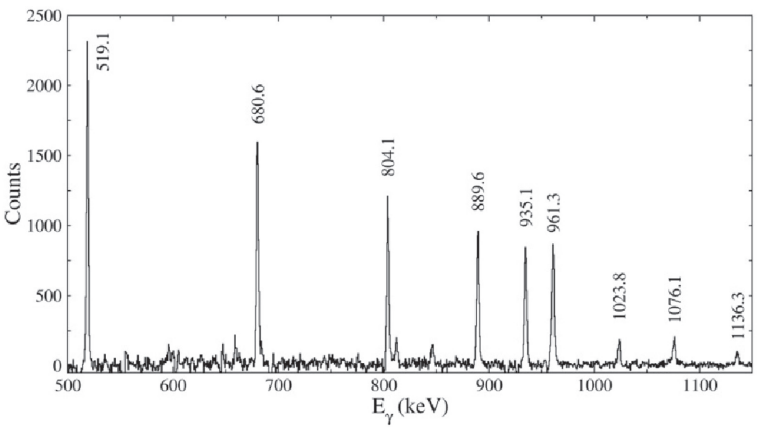

Fig. 5.1.9: Sum of energy gated spectra on 1024 & 1077 keV γ- transitions.

From the present experimental study, the high spin states of ^{127}Xe have been investigated. The strongly populated $\nu h_{11/2}$ band has been observed up to ~ 8.3 MeV as shown in Fig. 5.1.8. γ-transitions belonging to this band have been shown in the sum of the 1024 and 1077 keV energy gated spectra (Fig. 5.1.9). Spins and parities of several states of $\nu h_{11/2}$ band have been assigned from angular correlation and linear polarization results. Structure of this band before and after alignment, has been discussed in Ref. [5, 6]. Beside this yrast $\nu h_{11/2}$ band, three more negative parity bands have been identified. Previously reported one and three quasi-particle positive parity bands have also been extended up to high spin.

Authors are thankful to the staff of the target lab, Pelletron accelerator and INGA facilities at IUAC, New Delhi. The first author is also thankful to the Council of Scientific and Industrial Research (CSIR), India, for Senior Research Fellowship under file no. 9/13(662)/2017-EMR-I.

REFERENCES

1. A. Gelberg et al, Nucl. Phys. A **557,** 439c (1993).
2. C. -B. Moon et al, Phys. Rev. C **76,** 067301 (2007).
3. A. Al-Khatib et al, Phys. Rev. C **83,** 024306 (2011) and references therein.
4. W. Urban et al, Z. Phys. A **320,** 327 (1985).
5. S. Chakraborty et al, Braz. J. Phys. **47,** 406 (2017).
6. S. Chakraborty et al, Proc. DAE Symp. Nucl. Phys. **61,** 278 (2016).

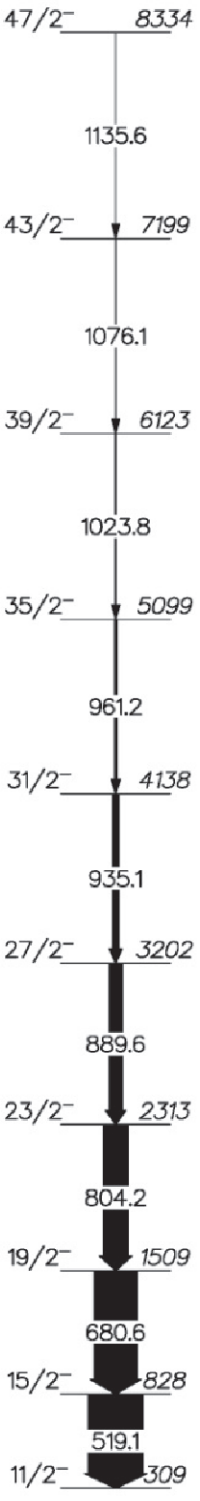

Fig. 5.1.8: Partial level scheme of ^{127}Xe.

5.1.7 High spin structure of Rn isotopes and role of high-j orbitals

Soumik Bhattacharya[1,2], S. Bhattacharyya[1,2*], R. Banik[1,2], R. Raut[3], A. Dhal[1], S. Nandi[1,2], S. Das Gupta[4], D. Mondal[1,2], R. P. Singh[5], Indu Bala[5], S. Muralithar[5], A. Sharma[5], S. S. Bhattacharjee[5] and V. Srivashtava[5]

[1]Variable Energy Cyclotron Centre, 1/AF, Bidhannagar, Kolkata 700064, India
[2]Homi Bhabha National Institute, Anushaktinagar, Mumbai 400094, India
[3]UGC-DAE-CSR Consortium, Kolkata 700107, India
[4]Heritage Institute of Technology, Anandapur, Kolkata 700107, India.
[5]Inter University Accelerator Centre, Aruna Asaf Ali Marg, New Delhi 110067, India

Four proton 'particles' and few neutron 'holes' outside doubly closed ^{208}Pb nucleus make the study of Radon isotopes very interesting in order to understand the interaction between the core and valance particles. Low lying states in these nuclei are dominated by single particle configurations with the four valence protons occupying the available $f_{7/2,}$ $h_{9/2,}$ $i_{13/2}$ orbitals and for neutron $p_{1/2,}$ $f_{5/2,}$ $p_{3/2}$ orbitals. At higher energy neutron core excitations play a significant role. Around Z = 82 shell closure region, various exotic phenomena have been observed ranging from well-established super-deformed states [1] in Hg, Tl, Pb, and Bi to shears bands, observed in several Pb [2,3] and Bi isotopes [4]. A dipole band structure is also reported in ^{205}Rn built on the isomer [5]. Same exotic phenomena are also expected beyond Z = 82 with the availability of unique parity $i_{13/2}$ orbital for both protons and neutrons which also provide a fertile ground to study the high spin isomers and the band structure built on that.

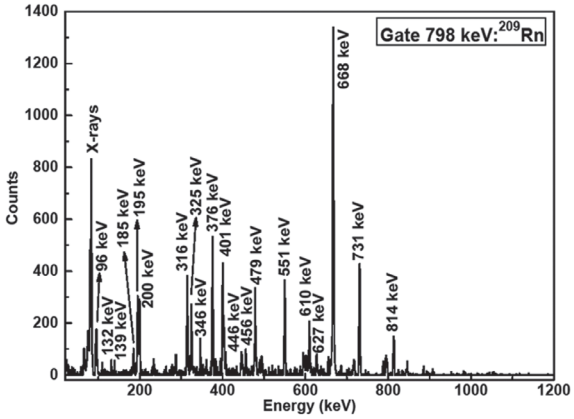

Fig. 5.1.10: Coincidence spectra corresponding to the ground state transition of ^{209}Rn observed from the current work.

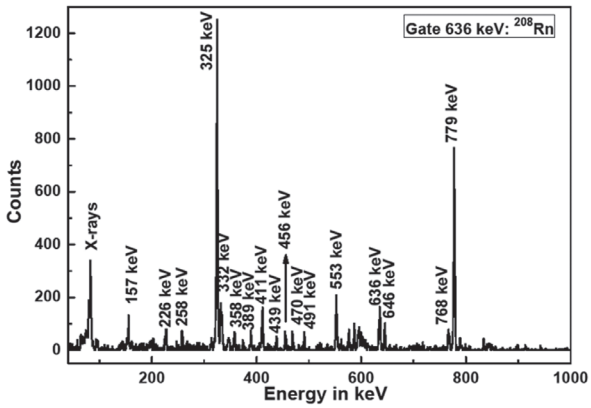

Fig. 5.1.11: Transitions in coincidence with 636-637 keV doublet transition corresponding to ^{208}Rn.

In view of the above interest, high spin states above the long lived isomers of ^{209}Rn and ^{208}Rn are produced with ^{16}O beam from the 15UD Pelletron facility at IUAC with following fusion evaporation reaction ^{16}O+^{198}Pt → ^{209,208}Rn+5n,6n at 102 MeV beam energy. We used a self-supported, 9.3 mg/cm^2 thick, enriched ^{198}Pt foil as target. The gamma rays, from the excited levels, were detected using INGA facility which consists of 18 Compton Suppressed Clover HPGe detectors and 2 LEPS detectors. The list mode data were collected with two-fold coincidence as well as in singles trigger condition and the corresponding time was also measured with TDC. Calibration and continuous monitoring of the FWHM of each crystal were carried out using standard ^{152}Eu and ^{133}Ba sources. Preliminary analysis indicates the production of ^{208}Rn and ^{209}Rn with comparable cross sections. The representative gated spectra corresponding to the transitions from ^{208}Rn and ^{209}Rn are shown Fig. 5.1.10 and 5.1.11, respectively. Almost all of the relevant transitions can be seen in the figures. Further analysis is in progress.

REFERENCE

[1] R. V. F. Janssens and T. L. Khoo, Annu. Rev. Nucl. Part. Sci. **41,** 321 (1991).
[2] S. Frauendorf, Nucl. Phys. A **557,** 259 (1993).
[3] R. Clark et al., Phys. Rev. Lett. **78,** 1868 (1997).
[4] P. J. Dagnal et al., J. Phys. G **20,** 1591 (1994).
[5] J.R. Novak et al., Phys. Rv. C **59,** R2989 (1999).

5.1.8 Observation of pairing of valence neutrons in ^{18}O using ^{27}Al(^{18}O,^{16}O n)^{28}Al

B. N. Joshi[1], N. Madhavan[2], J. Gehlot[2], S. Nath[2], A. Yadav[2], V. Srivastava[2], M. M. Hosamani[2], K. Mahata[1], K. S. Golda[2], Y. Gupta[1], V. Desai[1], Md. Moin Shaikh[2], M. Kuhshwaha[1], A. Parihari[1], G. Mohanto[1], M. Kumar[2], A. Banarjee[3], T. Varughese[2], A. Saxena[1] and Arun K. Jain[1]

[1]Nucelar Physics Division, Bhabha Atomic Research Centre, Mumbai 400085, India
[2]Inter University Accelerator Centre, Aruna Asaf Ali Marg, New Delhi 110067, India
[3]Dept of Physics and Astrophysics, Delhi University, Delhi 110007, India

Nucleon-nucleon interaction has two strong attractive residual interactions besides the mean field interaction responsible for the shell model leading to the magic numbers. One of the residual interactions is the long range attractive one leading to the clustering of the surface nucleons. The other one is a short range attractive part leading to pairing of the nucleons in the dense nuclear interior. In order to gain an additional binding this pairing interaction should lead to increased relative momentum between the two valence neutrons in ^{18}O. For studying this effect, we have measured the neutron angular distribution in the ^{27}Al(^{18}O,^{16}O n)^{28}Al reaction at 75, 90 and 100 MeV incident energies. When the two valence neutrons' centre of mass is farther away from the ^{16}O centre

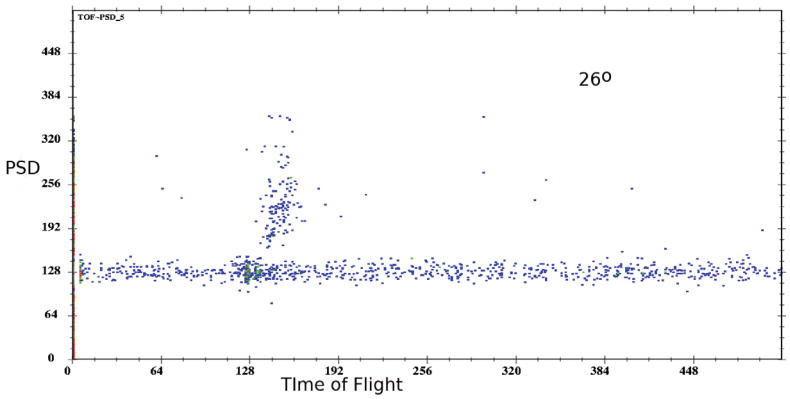

Fig. 5.1.12: Time of flight vs PSD spectrum from a neutron detector.

then the relative momentum between the two neutrons is expected to be large if they are paired. On the other hand if they are clustered then this relative momentum is expected to be small. When the centre of the two neutrons comes closer to the ^{16}O centre, the relative momentum between the two neutrons is expected to be comparatively smaller as compared to when their centre of mass is farther away from the ^{16}O centre when the two neutrons are paired. The opposite is expected when the two neutrons are clustered. Therefore, when the ^{16}O is having larger momentum in the ^{18}O any neutron pick up reaction will show the neutron angular distribution shifted to smaller angles compared to when the ^{16}O is having smaller momentum in the ^{18}O. More than 40 years ago, the neutron pick up reaction in ^{6}Li(d, tp)^{4}He showed [1] the angular distribution to be shifted toward larger angles indicating the deuteron cluster to be shrunk in ^{6}Li, indicating the neutron and proton in the deuteron cluster in ^{6}Li to be clustered. Experiment using the reaction ^{27}Al(^{18}O, n^{16}O)^{28}Al was performed using HYRA [2] at IUAC. The HYRA was operated in vacuum mode and configured to select the appropriate energy of ^{16}O. Beam-like particle were rejected by placing a slit in between MD1 and MD2. Pulsed ^{18}O beam of 1 μs interval was used at three incident energies: 100 MeV, 90 MeV and 75 MeV. A self-supporting natural aluminum target of thickness 500 μg/cm^2 was pasted at the centre of the entrance of the bellow pipe, before the small scattering chamber. A silicon PAD detector of 300 μm × 2 cm × 2 cm was placed in HYRA focal plane to measure energy of the ^{16}O. Beam spot was tuned on the target position by inserting a quartz crystal at the target chamber. Six numbers of 5 inch × 5 inch, liquid scintillator based neutron detectors were placed at a distance of 107 cm from the target to get the neutron angular distribution from ~ 25º to ~ 55º in lab. Neutrons and gammas were separated clearly by the pulse shape discrimination (PSD) method as seen in Fig. 5.1.12. Prompt gamma rays were used as a reference to measure the time-of-flight of the neutrons. Neutron angular distributions were obtained at three energies. Peaks of the three angular distributions were normalized to the 90 MeV peak as seen in Fig. 5.1.13. A clear shift in the angular distributions is seen for the 100 MeV and 75 MeV angular distributions compared to the 90 MeV data. The inward shift in angular distribution is the signature of paring of two neutrons in ^{18}O.

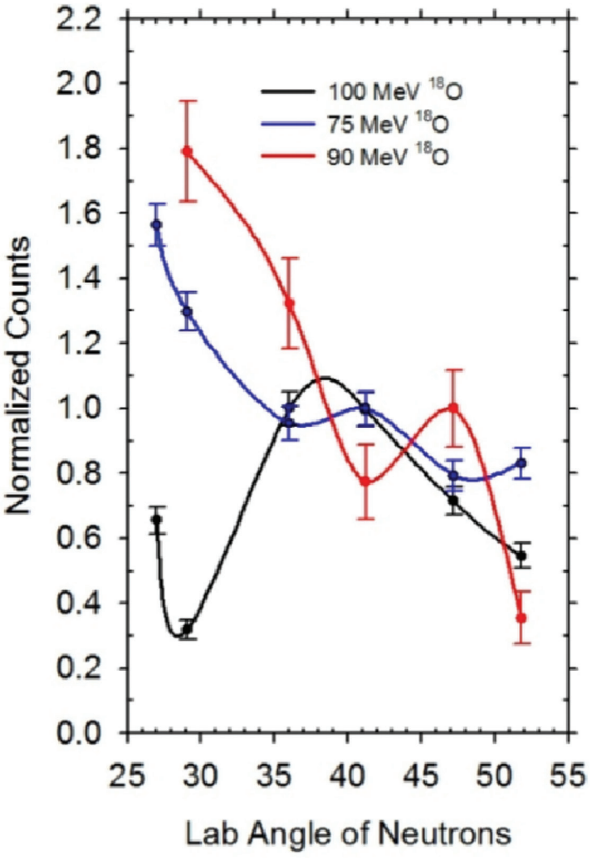

Fig. 5.1.13: Peak normalized neutron angular distributions for the reaction ^{27}Al(^{18}O, n^{16}O)^{28}Al at three energies.

REFERENCE

[1] A K Jain et al., Phys. Rev. Lett. **32,** 173 (1974).
[2] N. Madhavan et al., Pramana – J. Phys. **75,** 317 (2010).

5.1.9 Multi-quasiparticle isomers below doubly-magic ^{208}Pb

S. G. Wahid[1], S. K. Tandel[1], Poulomi Roy[1], S. Suman[1], M. Hemalatha[1], Anurag Patel[1], A. Y. Deo[2], Siddharth Rai[3], Anupriya Sharma[4], Soumendu Bhattacharjee[4], Pragati[2], S. Muralithar[4] and R. P. Singh[4]

[1]UM-DAE Centre for Excellence in Basic Sciences, Mumbai 400098, India
[2]Department of Physics, Indian Institute of Technology, Roorkee 247667, India
[3]Department of Physics, Viswa-Bharati, Santiniketan 731235, India
[4]Inter University Accelerator Centre, Aruna Asaf Ali Marg, New Delhi 110067, India

The structure of nuclei in the vicinity of magic numbers provides valuable insight into the ordering and relative spacing of single-particle energy levels. Nuclei lying just below the doubly-magic ^{208}Pb are near spherical and are characterized by high-j valence orbitals, neutron $i_{13/2}$ and proton $h_{11/2,}$ near the Fermi surface. These are suitable conditions for the realization of high-spin isomers with dominant contributions to their wave functions from the high-j orbitals. Information on high-spin isomers in the vicinity of the heaviest doubly-magic nucleus ^{208}Pb, which are built on configurations involving several valence protons and neutrons, provide key insights into single-particle and pairing energies. Therefore, they offer an opportunity to provide discriminating tests of modern-day, large-scale shell model calculations and the various interactions used.

Excited states in ^{202}Tl were populated in ^{198}Pt(^{7}Li,3n) reaction. Indian National Gamma Array (INGA) at IUAC was used to record two- and higher-fold γ-ray coincidence events.

Several new transitions have been identified and placed in the level scheme of ^{202}Tl. States above E_x = 2045 keV are newly identified. Most of the transitions are placed using the prompt data. Many transitions are evident in the delayed data as well due to feeding from an apparently long-lived, high-spin isomer.

Single-gated spectra on known, low-spin 390 and 493 keV transitions show all the new transitions above spin 8 and 9 levels up to which the level scheme was previously established. Two strong parallel branches are found above the 2045 keV state. The 694 and 861 keV transitions are intense and constitute parallel branches. All new gamma rays above these parallel branches are in coincidence with the 694 keV as well as the 861 keV transitions and all gamma rays below. The 134 keV transition is newly established and is in coincidence with the 694 keV as well as 861 keV gamma rays. Fig. 5.1.14 displays spectra obtained by gating on some of the new transitions: (a) 134 keV; (b) 694 keV; (c) 861 keV.

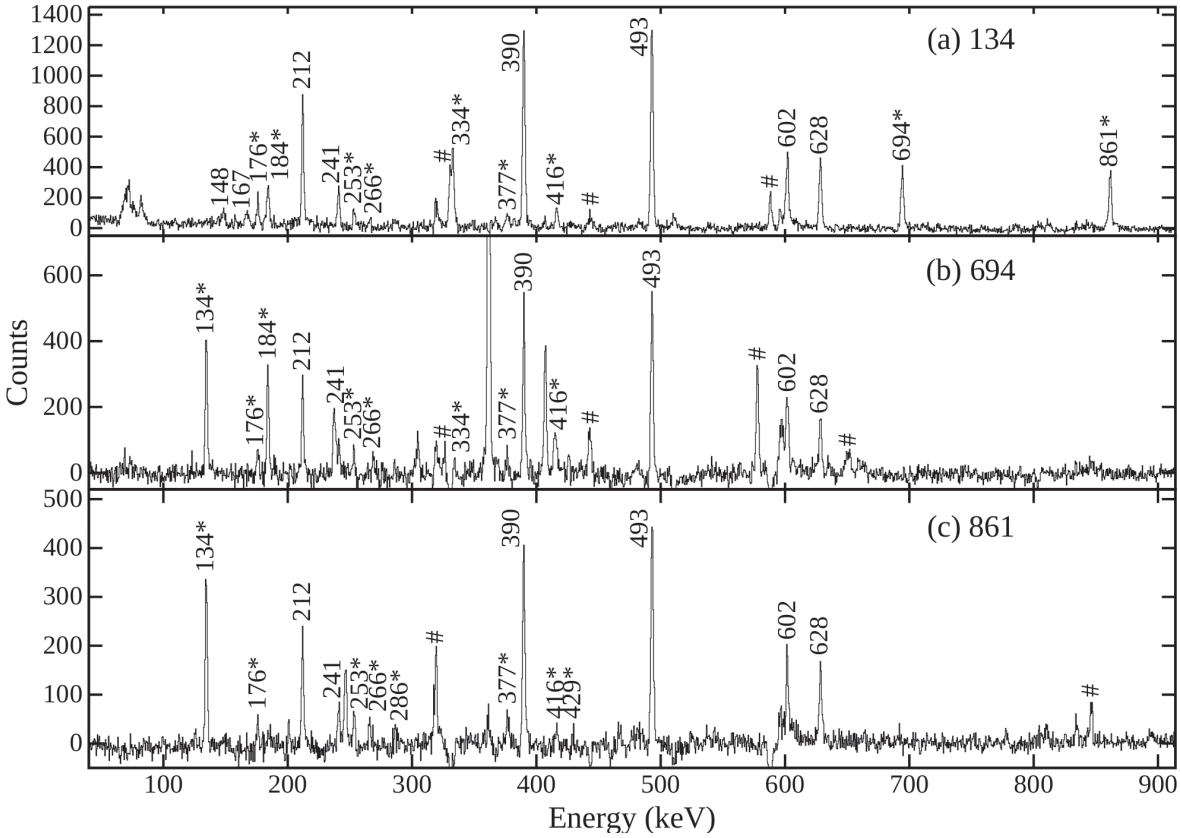

Fig. 5.1.14: Spectra obtained by gating on the strong new transitions; (a) 134 keV, (b) 694 keV and (c) 861 keV. New transitions are marked with an asterisk and contaminant ones are labelled with hash marks.

Several other new transitions can be seen in these spectra. DCO ratios and polarization information for many new transitions are being obtained to firmly assign spin and parity for the newly identified levels.

REFERENCES

1. E. Wilson et. al., Phys. Lett. B **747,** 88 (2015).
2. J. Wrzesinski et. al., Phys. Rev. C **92,** 044327 (2015).
3. Zs. Podolyak et. al., J. Phys. Conf. Ser. **580,** 012010 (2015).
4. M. Pfutzner et. al., Phys. Lett. B **444,** 32 (1998).

5.1.10 No evidence of reduced collectivity in Coulomb excited Sn isotopes

R. Kumar[1], M. Saxena[2], P. Doornenbal[3], A. Jhingan[1], A. Banerjee[4], R. K. Bhowmik[1], S. Dutt[5], R. Garg[1], C. Joshi[6], V. Mishra[7], P. J. Napiorkowski[2], S. Prajapati[8], P. A. Soederstroem[3] and H. J. Wollersheim[9]

[1]Inter University Accelerator Centre, Aruna Asaf Ali Marg, New Delhi 110067, India
[2]Heavy Ion Laboratory, University of Warsaw, 02-093 Warsaw, Poland
[3]Riken Nishina Centre for Accelerator-Based Science, Saitama 351-0198, Japan
[4]Department of Physics and Astrophysics, University of Delhi, Delhi 110007, India

[5]Department of Physics, Aligarh Muslim University, Aligarh 202002, India
[6]Department of Physics, M.S. University of Baroda, Vadodara 390002, India
[7]Department of Physics, Institute of Science, Banaras Hindu University, Varanasi 221005, India
[8]Department of Physics, Bareilly College, Bareilly 243005, India
[9]GSI Helmholtzzentrum fur Schwerionenforschung GmbH, D-64291 Darmstadt, Germany

Recently, we performed two Coulomb excitation experiments at GSI [1] and at IUAC [2] to obtain high precision data for ^{112,114}Sn isotopes. The measured B(E2↑) values were normalized to the one of ^{116}Sn, which seemed to be well established [3]. Surprisingly, the experimental data showed a rather asymmetric behavior which could not be explained by shell model [4] or mean field [5] calculations.

In a recent Doppler Shift Attenuation measurement (DSAM) [6], a reduced collectivity was found for the mid-shell Sn nuclei with up to 20% lower B(E2) values as compared to previously found data [3].

We performed a series of Coulomb excitation experiments at IUAC in order to excite all stable Sn isotopes (^{112,116,118,120,122,124}Sn) with a ^{58}Ni beam. Both projectile and target nuclei were excited and from the 2^+ intensities the B(E2) value ratios can be determined in a straight forward manner.

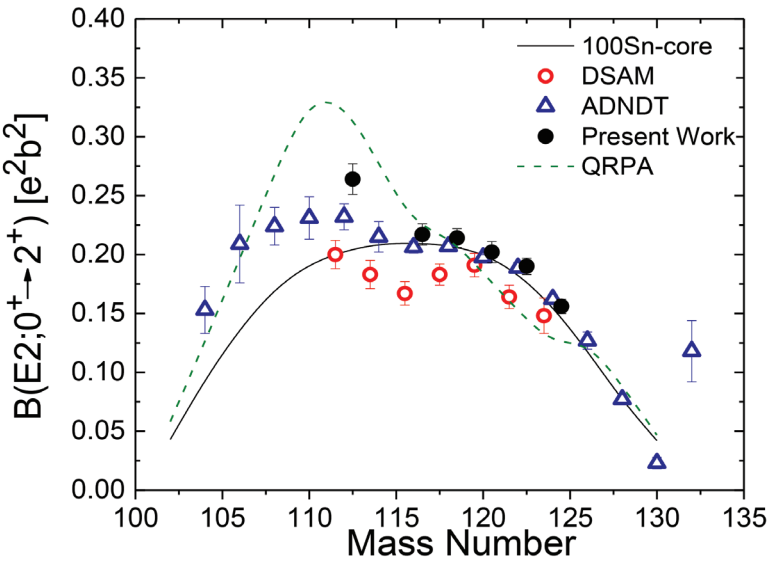

Fig. 5.1.15: Dependence of B(E2↑) values of Sn-isotopes on the mass number. Surprisingly, one observes for the stable Sn isotopes a disagreement up to ~20% between the recently measured values by Jungclaus et al. [6], using the DSA method, and the tabulated ADNDT data [7]. For comparison with the experimental data, results of Large Scale Shell Model calculation are shown which use a ^{100}Sn core (for details see Ref. [8]).

From the intensity of the Doppler corrected γ-ray lines corresponding to the $2^+ \rightarrow 0^+$ transitions, the target as well as projectile excitation could be extracted for distant collisions. These γ-ray yields are a direct measure of the B(E2; $0^+ \rightarrow 2^+$) values and show almost no feeding from higher excited states. In order to obtain high precision results, the B(E2) values of ^{112,116,118,120,122,124}Sn were determined relative to the B(E2;$0^+ \rightarrow 2^+$) = 0.0705(18) e^2b^2 value of ^{58}Ni. The experimental γ-ray ratios were corrected for the different Ge detectors' efficiencies (< 1.2%) and target enrichment (< 4.2%).

The Coulomb excitation calculations were performed using the Winther-de Boer COULEX code [9]. In these calculations, not only the first excited 2^+ state and the related B(E2; $0^+ \rightarrow 2^+$) value was included, but also the higher excited 2^+ and 4^+ states. The slowing down of the projectiles in the targets (0.8 %), the uncertainty of the PPAC boundaries (0.5 %) and the adopted ^{58}Ni B(E2 ↑) value (2.5 %) were also considered. The subsequent γ-ray decay was calculated for the particle-γ angular correlation, taking into account the internal conversion and the finite geometry of the γ-detector. The de-orientation of the particle-γ correlation, caused by the interaction of the nucleus with the magnetic moment of the atomic shell, was determined experimentally. For the short lived 2^+ states ($T_{1/2}$ < 1ps) of tin isotopes the de-orientation is expected to be very small. Since the tin ionization was not investigated in the present experiment and hence the atomic spin is unknown, the nuclear g-factor of the 2^+ state was not extracted from de-orientation coefficients as done in [10].

In the second step of the analysis, the close collision data were analyzed, similarly, to the Ni projectiles detected in the PPAC for the small $\theta_{c.m.}$ scattering angles. The B(E2; $0^+ \rightarrow 2^+$) value was kept constant and the re-orientation matrix element $< 2^+||M(E2)||2^+ >$ was adjusted to the γ-ray intensity ratio measured in the angular range of $90^\circ < \theta_{c.m.} < 150^\circ$. In an iterative process, the newly determined quadrupole moments were used for the distant collision analysis but it did not change the B(E2; $0^+ \rightarrow 2^+$) values significantly. The present experimental results are summarized in Table 1 and are compared with the published data [6, 10].

B(E2↑) values obtained using our data agree well with the recent Coulomb excitation results, thus confirming the disagreement to the DSA lifetime data. We confirmed earlier Coulomb excitation data from [11], [12] and

the adopted values from [7]. We note that with the present re-measurement for the B(E2) of ^{116}Sn, our previously published values of 0.242(8) e^2b^2 and 0.232(8) e^2b^2 for ^{112,114}Sn which are based on a relative measurement, are increased by ~4% to 0.251(8) e^2b^2 and 0.241(8) e^2b^2, respectively. The B(E2) value for ^{112}Sn inserted in Table 1, is slightly larger as compared to our earlier publication [2].

Table I: Comparison of the measured B(E2 ↑) values of the Sn isotopes extracted from the present experiment with the Coulomb excitation experiment [10] and the DSA life time measurements [6].

Isotope	B(E2; $0^+ \rightarrow 2^+$) Present	$<2^+\|\|M(E2)\|\|2^+>$ Present	B(E2; $0^+ \rightarrow 2^+$) Ref. [10]	$<2^+\|\|M(E2)\|\|2^+>$ Ref. [10]	B(E2; $0^+ \rightarrow 2^+$) Ref. [6]
^{112}Sn	0.264(13)	0.01(15)	0.250(10)	0.05(12)	0.200(12)
^{114}Sn	0.241(8)[A]	-	0.229(9)	0.12(11)	0.183(12)
^{116}Sn	0.217(9)	0.26(14)	0.205(8)	0.22(11)	0.167(10)
^{118}Sn	0.214(8)	0.21(13)	0.203(9)	0.09(12)	0.183(9)
^{120}Sn	0.202(9)	0.19(14)	0.210(9)	-	0.191(10)
^{122}Sn	0.190(7)	0.17(13)	0.198(9)	-0.11(12)	0.164(10)
^{124}Sn	0.156(6)	0.23(14)	0.165(7)	-0.11(12)	0.148(15)

[A] The B(E2↑) value of ^{114}Sn [2] was normalized with respect to the average value determined from the present measurement and [10].

As the experimental B(E2 ↑) values of the stable Sn isotopes show no evidence of reduced collectivity, the discussion reported in Kumar *et al.* [2] is still valid in which the experimental data are compared with theoretical calculations using RQRPA [5] and LSSM [8]. The dependence on the neutron number is asymmetric with respect to the mid-shell nucleus ^{116}Sn.

The measured re-orientation matrix elements of the stable Sn isotopes have positive signs and hence describe an oblate nuclear shape. They have large uncertainties and are in reasonable agreement with the recently performed Coulomb ex-citation measurements [10]. In the case of ^{122,124}Sn, a different sign is reported, though the large error bars are compatible with either oblate or prolate shapes.

In summary, Coulomb excitation measurements have been performed for ^{112,116,118,120,122,124}Sn using ^{58}Ni as projectile. The determined B(E2 ↑) values were measured with high precision and agree well with earlier measurements as well as recent Coulomb excitation experiment.

REFERENCES

1. P. Doornenbal et al., Phys. Rev. C **78,** 031303 (2008).
2. R. Kumar et al., Phys. Rev. C **81,** 024306 (2010).
3. S. Raman, C. W. N. Jr., and P. Tikkanen, Atom. Data and Nucl. Data Tab. **78,** 1 (2001).
4. A. Banu et al., Phys. Rev. C **72,** 061305 (2005).
5. A. Ansari, Phys. Lett. B **623,** 37 (2005).
6. A. Jungclaus et al., Phys. Lett. B **110,** 695 (2011).
7. B. Pritychenko et al., At. Data Nucl. Data Tables **107,** 1 (2016).
8. A. Banu et al., Phys. Rev. C **72,** 061305(R) (2005).
9. A. Winther and J. de Boer, in Coulomb Excitation, edited by K. Alder and A. Wiinther, (Academic Press, New York/London, 1966).
10. J. M. Allmond et al., Phys.Rev. C **92,** 041303(R) (2015).
11. R. Graetzer, S. M. Cohick, and J.X. Saladin et al., Phys. Rev. C **12**, 1462 (1975).
12. P. H. Stelson, F. K. McGowan and R. L. Robinson et al., Phys. Rev. C **2,** 2015 (1970).

5.1.11 Projectile structure effect on the onset and strength of incomplete fusion

Vijay R. Sharma and R. Kumar

Inter University Accelerator Centre, Aruna Asaf Ali Marg, New Delhi 110067, India

An offline experiment was performed to explore the dynamics of incomplete fusion process and to understand the role of non-alpha cluster projectile on incomplete fusion processes. Beam of ^{14}N were impinged on the ^{169}Tm target at energies starting from the Coulomb barrier to well above it. Analysis has been done using Candle software developed at IUAC, New Delhi. Further, the evaporation residues have been identified by their characteristics gamma-lines, and confirmed by decay-curve analysis for each. Experimental excitation function

of ^{179}Os (4n), ^{179}Re (p3n) and ^{178}Re (p4n), ^{177}W (α2n), ^{176}W(α3n), ^{175}W (α4n), and ^{174}W (α5n) evaporation residues have been analysed in the framework of equilibrated CN-decay using statistical model code PACE4. In order to check the accuracy of our measurements and to test the adopted data reduction procedure, an attempt has been made to deduce the value of fusion barrier (V_B) in the lab system, from the analysis of experimentally measured complete fusion cross section. According to Gutbrod et al. [1], the normalized CF probability may be given as

$$\sigma_{CF} = \pi R^2 (1 - V_B / E_{c.m.}) \quad (1)$$

The normalized values of σ_{CF} is plotted as a function of $1/E_{c.m.}$ in Fig. 5.1.16. As shown in this figure, the data points follow a straight-line trajectory which intersects the x-axis at $E_{c.m.}$ (projectile energy in the c.m. frame) corresponding to $V_B \approx 63$ MeV. This corresponds to the value of fusion barrier of the ^{14}N+^{169}Tm system and strengthens the present measurements and the data reduction procedure.

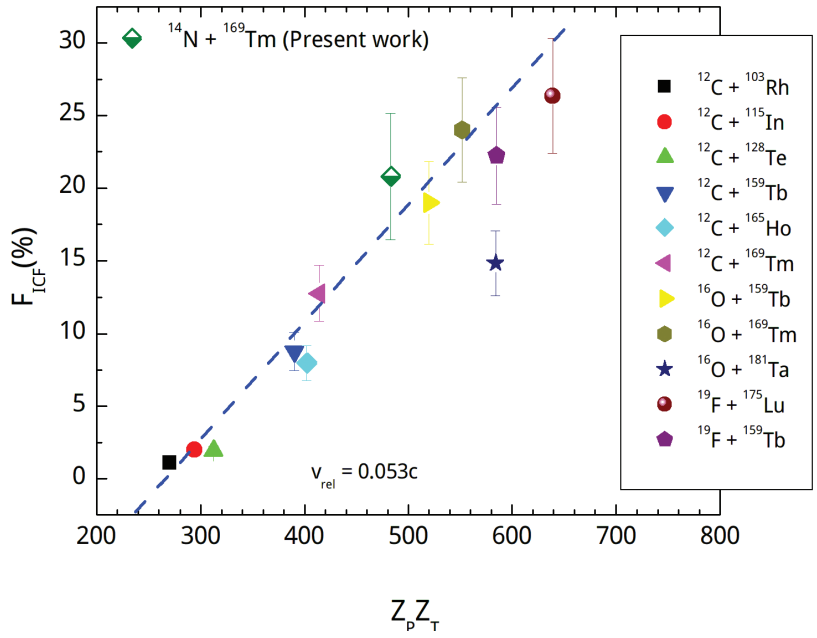

Fig. 5.1.16: Incomplete fusion strength function (F_{ICF}) of various systems (see text) as a function of Z_pZ_T. The dashed line is drawn to guide the eyes.

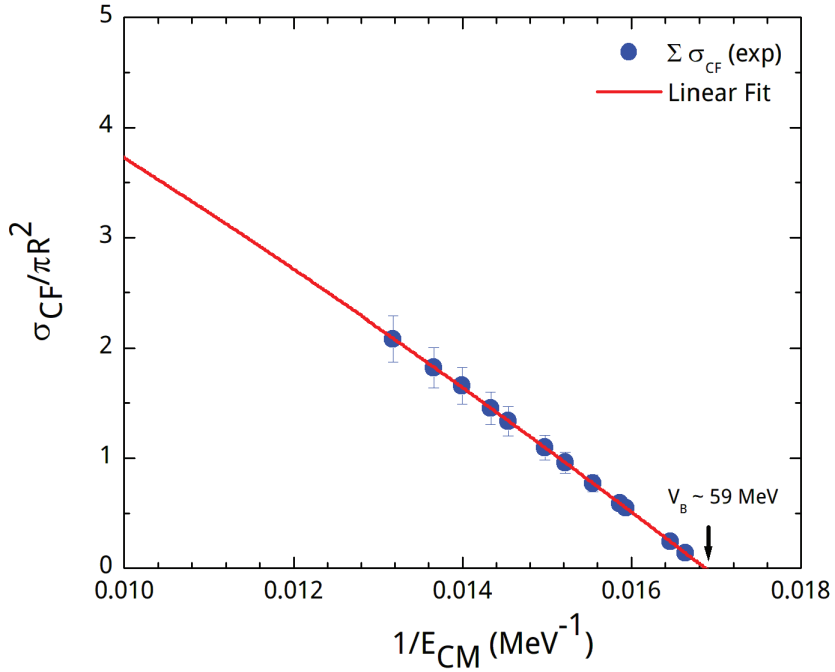

Fig. 5.1.17: CF cross sections as a function of $1/_{Ec.m.}$ found to reproduce the Coulomb barrier for ^{14}N+^{169}Tm system. The continuous line through the data points is achieved by best fitting procedure of data.

To summarize, it has been observed that the onset and strength of ICF strongly depend on projectile type and projectile energy. Therefore, we extended this study in terms of charge dependence on ICF fraction. In order to display the charge dependence, the ICF strength function for the presently studied system at constant relative velocity ($v_{rel} \approx 0.053c$) is plotted as a function of Z_pZ_T (i.e. product of projectile and target atomic numbers) and is presented in Fig. 5.1.17 along with F_{ICF} of systems available in the literature to have Z_pZ_T systematics [2], if any. As can be seen from this figure, the percentage of incomplete fusion fraction $F_{ICF,}$ follows almost a linear growth as the charge product Z_pZ_T increases. Further, the value of F_{ICF} is found to be more for larger Z_pZ_T values, which indicates the role of Coulomb repulsion on ICF fraction i.e. as the projectile comes near the field of the target nucleus (for higher Z_pZ_T) it may break-up easily as compared to low Z_pZ_T projectile target combination. An increase in the value of Z_pZ_T enhances the strength of the Coulomb interaction resulting in the larger break-up probability. Hence, in the development of the ICF modeling at low energies, Z_pZ_T should also be taken into account.

One of the authors (VRS) thanks Dr. N. Madhavan for fruitful discussion on ICF studies

REFERENCES

1. H. H. Gutbrod, W. G. Winn, and M. Blann, Phys. Rev. Lett. **30,** 25 (1973).
2. R. Kumar , Vijay R. Sharma et al., submitted to Phys. Rev. C (2017).

5.1.12 Fission fragment mass distributions of nuclei populated by multi-nucleon transfer channels in ^{6,7}Li+^{238}U reaction

A. Pal[1,2], S. Santra[1,2], D. Chattopadhyay[1,2], A. Kundu[1,2], A. Jhingan[3], P. Sugathan[3], N. Saneesh[3], Mohit Kumar[3], N. L. Singh[4], A. Yadav[3], C. Yadav[3], R. Dubey[3], K. Kapoor [5], Kavita Rani[5], Honey Arora[5], Visakh A.C.[6], Devinder Kaur[5], B. K. Nayak[1,2], A. Saxena[1,2] and S. Kailas[1]

[1]Nuclear Physics Division, Bhabha Atomic Research Centre, Mumbai 400085, India
[2]Homi Bhabha National Institute, Anushaktinagar, Mumbai 400094, India
[3]Inter University Accelerator Centre, Aruna Asaf Ali Marg, New Delhi 110067, India
[4]Department of Physics, The M. S. University of Baroda, Vadodara 390002, India
[5]Department of Physics, Punjab University, Chandigarh 160014, India
[6]Department of Physics, Central University of Kerala, Kasaragod, Kerala 671123, India

Measurements of fission fragment angular distributions (FFAD) and mass distributions (FFMD) have been scarcely carried out for fission following transfer reactions. Recently, effect of transfer induced fission on inclusive FFAD for ^{6}Li +^{232}Th systems have been studied by A. Pal et al.[1]. The study of the effect of transfer or projectile breakup on FF mass and folding angle distribution is equally interesting. In the present work, FF folding angle distribution (FFFAD) and FFMD for transfer/ breakup induced fission for ^{6,7}Li+^{238}U system have been measured exclusively and the unusual behavior observed in FFFAD and FFMD have been explained. The mass-distributions of several exotic neutron-rich fissioning nuclei, namely, ^{242,243,244}Pu and ^{240,241}Np, populated in multi-nucleon transfer/ ICF reactions have been obtained. Interestingly, the mass-distributions of the composite nuclei ^{244}Pu and ^{241}Np cannot be measured using the fusion reaction of any stable target/projectile combination.

An experiment on ^{6,7}Li+^{238}U reaction was carried out at 15UD Pelletron facility at IUAC. Details of the experimental set up have been reported in Ref [2]. Mass distributions obtained for inclusive fissions and in coincidence with alpha (dominant transfer channel), deuteron/triton and proton have been shown respectively in Fig. 5.1.18 (a),(b),(c) and (d) for ^{6}Li + ^{238}U reaction and in Fig. 5.1.19 (a),(b),(c) and (d) for ^{7}Li + ^{238}U reaction. In ^{6}Li + ^{238}U reaction, the α, d and p-gated fission events correspond to the composite fissioning nuclei ^{240}Np, ^{242}Pu and ^{243}Pu (formed by the capture of deuteron, α and ^{5}He respectively), Whereas, in ^{7}Li+^{238}U reaction, the α, t and p-gated fission events correspond to the composite fissioning nuclei ^{241}Np, ^{243}Pu and ^{244}Pu (formed by the capture of triton, α and ^{6}He, respectively).

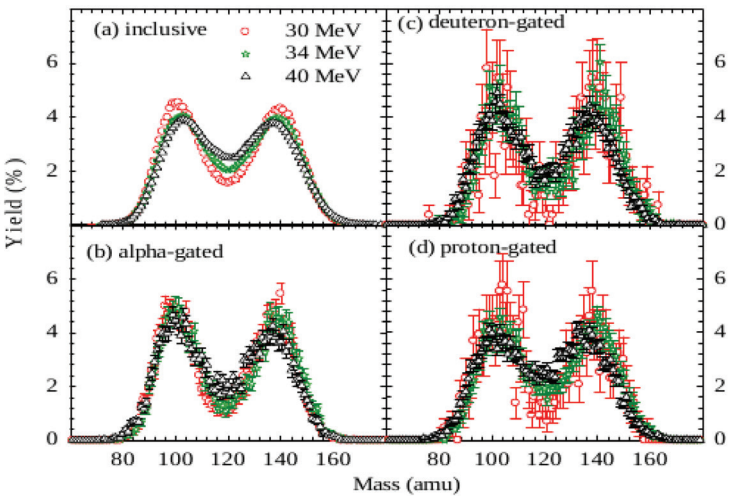

Fig. 5.1.18: Mass distributions in ^{6}Li+^{238}U reactions.

The P/V ratios for transfer induced fission channels are more compared to CF-fission at respective projectile energies and, hence, responsible for the enhancement in the P/V ratio of inclusive fission compared to CF-fission. Observation of peak of FFFAD for ICF-fission at below barrier energy at smaller angle compared to the one in CF fission also confirms the presence of breakup induced fission. Thus in the present exclusive measurements, the mass distributions of a few exotic neutron-rich nuclei populated by multi-nucleon transfer reaction have been obtained and these transfer induced fission channels have been found to be responsible for enhancing P/V ratio of inclusive mass distribution compared to the ones in CF-fission and also for enhancing the width of folding angle distributions at sub-barrier energies.

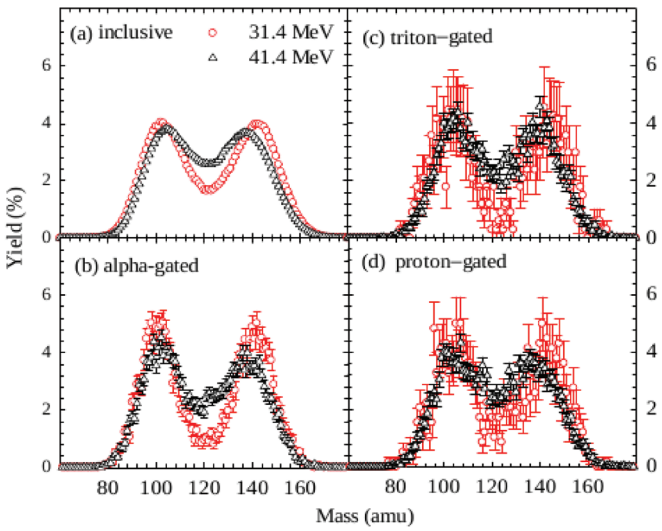

Fig. 5.1.19: Mass distributions in $^{7}Li+^{238}U$ reactions.

REFERENCES

1. A. Pal et al., Phys. Rev. C **96,** 024603 (2017).
2. A. Pal et al., Proc. DAE-BRNS Symp. Nucl. Phys. **61,** 376 (2016) and references therein.

5.1.13 Investigating the effect of CELD in fission of pre-actinides

Tathagata Banerjee[1], S. Nath[1], A. Jhingan[1], N. Saneesh[1], Mohit Kumar[1], Abhishek Yadav[1], Gurpreet Kaur[2], R. Dubey[1], M. Shareef[3], P. V. Laveen[3], A. Shamlath[3], Md. Moin Shaikh[1], S. Biswas[4], J. Gehlot[1], K. S. Golda[1], P. Sugathan[1] and Santanu Pal[1]

[1]Nuclear Physics Group, Inter University Accelerator Centre, Aruna Asaf Ali Marg, Post Box 10502, New Delhi 110067, India
[2]Department of Physics, Panjab University, Chandigarh 160014, India
[3]Department of Physics, School of Mathematical and Physical Sciences, Central University of Kerala, Kasaragod 671314, India
[4]Department of Physics, Murshidabad College of Engineering and Technology, Cossimbazar Raj, Berhampore, Murshidabad 742102, India

Non-compound nuclear fission (NCNF) processes start competing with CN formation [1,2] from CN mass A~200 amu. Any discrepancy between measured fission excitation function and predictions of statistical model (SM) is usually attributed to the presence of NCNF in a reaction. However, choice of SM parameters and inclusion or exclusion of certain physical effects may vary the results of SM. Inclusion of the collective enhancement in level density (CELD) in the calculation of survival probability, gives better agreement with the experimental excitation functions [3]. We wanted to investigate the effects of CELD in the de-excitation of heavy compound nucleus in detail.

We measured fission fragment (FF) angular distributions for the reactions $^{19}F+^{182}W$, $^{19}F+^{187}Re$ and $^{19}F+^{193}Ir$ in the laboratory energy (E_{lab}) range of 82 – 120 MeV. The experiment was performed in the General Purpose Scattering Chamber (GPSC) at IUAC. Fragments were detected using nine hybrid telescope detectors [4], which were mounted on the

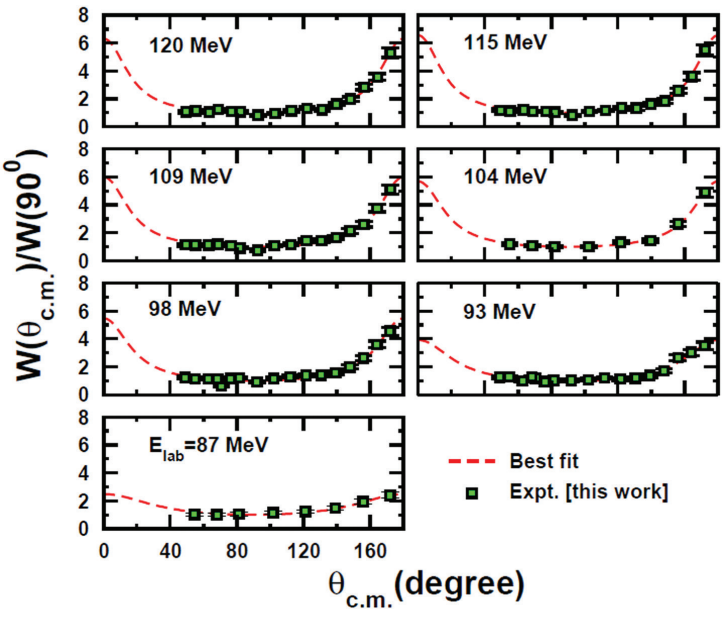

Fig. 5.1.20: Measured fission fragment angular distributions along with the best fit to data for the reaction $^{19}F+^{182}W$.

two movable arms inside the scattering chamber. Each telescope consisted of a ΔE (gas) detector and E (silicon) detector. Measurements were carried out with a large angular coverage (θ_{lab} = 41°-170°). FFs were distinguished from other reaction products based on energy loss and residual energy. Two monitor detectors (Si PIPS) were kept at 70 cm from the target and at θ_{lab} = 10° in the horizontal plane for positioning the beam on the target and for the absolute normalization of fission cross-sections.

The measured FF angular distributions, $d\sigma/d\Omega(\theta_{lab})$ were transformed to the center of mass (c.m.) frame of reference using Viola systematics for symmetric fission [5]. The FF angular distributions in the c.m. frame of reference, $d\sigma/d\Omega(\theta_{c.m.})$, thus obtained, were fitted with the exact theoretical expression [6] for the angular distribution function. The measured angular distributions, normalized to W(90°), for the reaction $^{19}F+^{182}W$ at different Elab are shown in Fig. 5.1.20.

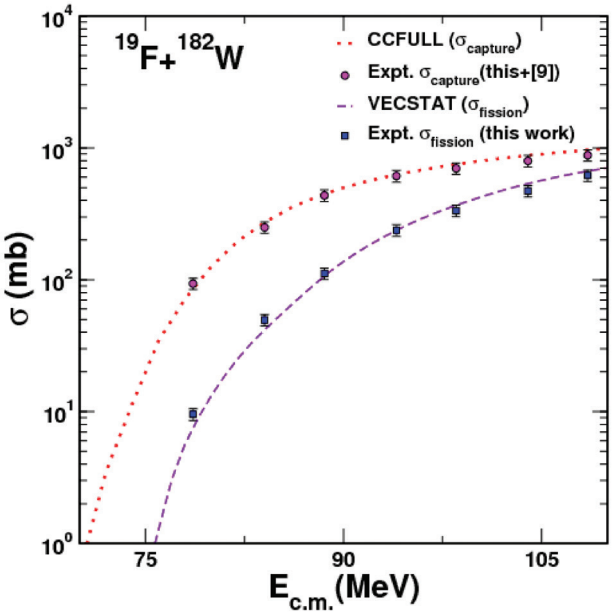

Fig. 5.1.21: Measured and calculated capture and fission cross sections for the reaction $^{19}F+^{182}W$. The dotted (violet) line represents VECSTAT predictions including the effects of shell, K orientation, CELD and a suitable strength of dissipation.

The experimental σ_{fis} for the reaction were obtained by integrating the measured $d\sigma/d\Omega(\theta_{c.m.})$ [7] and compared with the predictions of a statistical model code VECSTAT [8] (see Fig. 5.1.21). In this model, the fission barrier was calculated from the finite-range liquid drop model (FRLDM) potential [10]. Besides the effects of shell in the ground state level density and height of the fission barrier, effects of orientation (K-state) degree of freedom [11], CELD [12] and a suitable dissipation in the de-excitation of heavy nuclei, were also incorporated. Experimental capture cross sections showed agreement with CCFULL predictions [13]. A dissipation strength of 2×10^{21} s^{-1} was found to be sufficient to reproduce the data, as is shown in Fig. 2 for $^{19}F+^{182}W$. Further details can be found in Ref. [14].

REFERENCES

[1] Tathagata Banerjee, S. Nath and Santanu Pal, Phys. Rev. C **91,** 034619 (2015).
[2] Tathagata Banerjee et al., Phys. Rev. C **94,** 044607 (2016).
[3] D. A. Mayorov et al., Phys. Rev. C **90,** 024602 (2014).
[4] A. Jhingan et al., Proc. DAE-BRNS Symp. Nucl. Phys. **59,** 830 (2014).
[5] V. E. Viola et al., Phys Rev. C **31,** 1550 (1985).
[6] R. Vandenbosch and J. R. Huizenga, Nuclear Fission (Acadamic Press, New york, 1973).
[7] Tathagata Banerjee et al., Phys. Rev. C **96,** 014618 (2017).
[8] J. Sadhukhan, Ph.D. Thesis, Homi Bhabha National Institute, 2012 (unpublished).
[9] J. Gehlot et al., Proc. DAE-BRNS Symp. Nucl. Phys. **61,** 404 (2016).
[10] A. J. Sierk, Phys. Rev. C **33,** 2039 (1986).
[11] J. P. Lestone and S. G. McCalla, Phys. Rev. C **79,** 044611 (2009).
[12] V. I. Zagrebaev et al., Phys. Rev. C **65,** 014607 (2001).
[13] K. Hagino, N. Rowly and A. T. Kruppa, Comput. Phys. Commun. **123,** 143 (1999).
[14] Tathagata Banerjee et al., submitted to Phys. Rev. C (2017).

5.1.14 Measurement of sub-barrier fusion cross sections for $^{19}F+^{181}Ta$

Md. Moin Shaikh[1], S. Nath[1], J. Gehlot[1], Tathagata Banerjee[1], Ish Mukul[2], R. Dubey[1], A. Shamlath[3], P. V. Laveen[3], M. Shareef[3], A. Jhingan[1], N. Madhavan[1], T. Rajbongshi[4], P. Jisha[5], G. Naga Jyothi[6], A. Tejaswi[6], R. N. Sahoo[7] and Anjali Rani[8]

[1]Nuclear Physics Group, Inter University Accelerator Centre, Aruna Asaf Ali Marg, New Delhi 110067, India
[2]Department of Particle Physics and Astrophysics, Weizmann Institute of Science, Rehovot 76100, Israel
[3]Department of Physics, School of Mathematical and Physical Sciences, Central University of Kerala, Kasaragod 671314, India
[4]Department of Physics, Gauhati University, Guwahati 781014, India
[5]Department of Physics, University of Calicut, Calicut 673635, India
[6]Department of Nuclear Physics, Andhra University, Visakhapatnam 530003, India
[7]Department of Physics, Indian Institute of Technology Ropar, Rupnagar 140001, Punjab, India
[8]Department of Physics and Astrophysics, University of Delhi, Delhi 110007, India

Study of fusion excitation functions at deep sub-barrier energies has been an important area of research of late. Measurements have been performed up to very low cross sections in this energy regime. An onset of fusion hindrance at deep sub-barrier energies has been observed compared to the theoretical predictions, obtained from the coupled-channels (CC) calculations, in symmetric systems [1–3] with some exceptions [4, 5]. The observations for highly asymmetric systems are not very clear, while ^{6,7}Li+^{198}Pt systems [6, 7] showed no signs of fusion hindrance, signature of fusion hindrance was observed in the system ^{16}O+^{208}Pb [8]. Hence, precision measurements of fusion excitation functions at deep sub barrier energies are of utmost importance.

Recoil separators have extensively been used to measure heavy ion-induced fusion cross sections. However, unambiguous identification of the fusion products, viz. evaporation residues (ERs), amongst overwhelmingly dominant background events becomes extremely challenging in the deep sub-barrier energy regime. We have measured fusion cross sections for the asymmetric system ^{19}F+^{181}Ta at sub-barrier energies, till the energy at which ERs could be identified unambiguously.

The experiment was carried out at the 15UD Pelletron accelerator facility of IUAC. A pulsed 19F beam, with pulse separation of 4 μs, was bombarded on ^{181}Ta (170 μg/cm^2) target with a ^{nat}C (20 μg/cm^2) backing. ERs were separated from the background events using the recoil mass spectrometer, Heavy Ion Reaction Analyzer (HIRA). Two monitor detectors were placed at laboratory angle (θ_{lab}) 15.5º with respect to beam direction, for absolute normalization of ER cross section (σ_{ER}). ERs were detected by a multi-wire proportional counter (MWPC) at the focal plane of HIRA. Yields of ERs were extracted from the coincidence spectrum between energy loss ΔE (from the cathode of MWPC) and time-of-flight (TOF). Transmission efficiency of HIRA (ε_{HIRA}), crucially required for estimation of $\sigma_{ER,}$ was calculated using the semi-microscopic Monte Carlo code TERS [10].

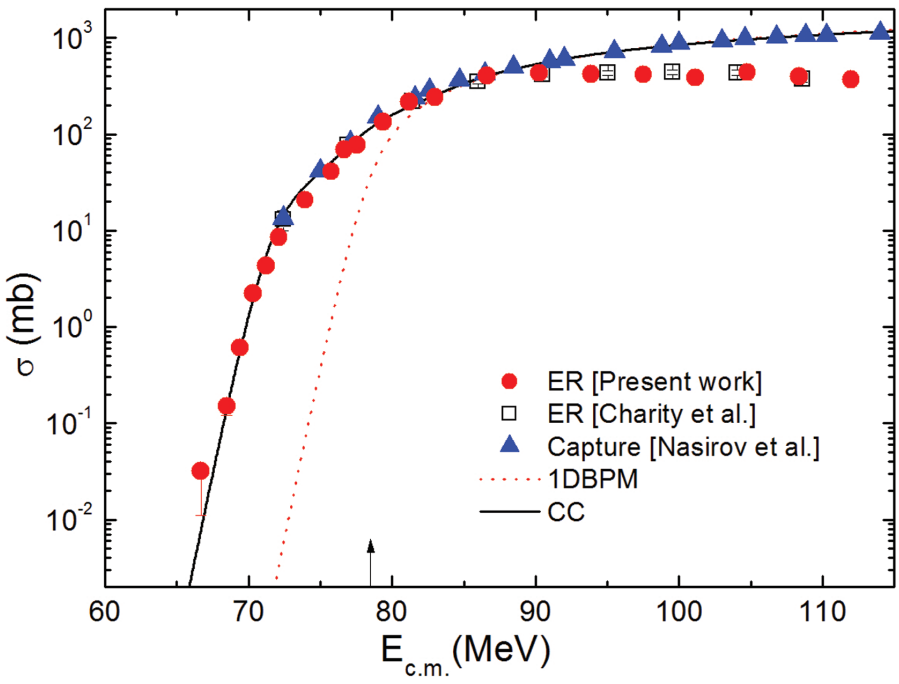

Fig. 5.1.22: The experimental fusion excitation functions for the system ^{19}F+^{181}Ta along with the theoretical predictions.

Hinde *et al.* [11] had reported experimental ER and fission excitation functions for ^{19}F+^{181}Ta, measured at E_{lab} = 80–126 MeV. We extended the measurements down to E_{lab} = 74 MeV. It is evident from Ref. [11] that the fission cross section (σ_{fis}) is insignificant compared to σ_{ER} at the range of E_{lab} (74–80 MeV) considered in the present work. Therefore, σ_{ER} is considered to be σ_{fus} in the present work. On the other hand, at E_{lab} above the barrier, one has to consider $\sigma_{fus} = \sigma_{ER} + \sigma_{fis.}$ Measured σ_{ER} along with $\sigma_{fus,}$ which was obtained from the work of Nasirov *et al.* [12] are shown in Fig. 5.1.22. Measured σ_{fus} appears to be well reproduced by conventional CC calculations, calculated employing the code CCFULL [13].

The authors thank the Pelletron staff of IUAC for providing beams of excellent quality throughout the experiment, Mr. Abhilash S. R. for assistance in fabricating the target and Mr. T. Varughese for support during the experiment.

REFERENCES
[1] C. L. Jiang et al., Phys. Rev. Lett. **89,** 052701 (2002).
[2] C. L. Jiang et al., Phys. Rev. Lett. **93,** 012701 (2004).
[3] A. M. Stefanini et al., Phys. Rev. C **82,** 014614 (2010).
[4] A. M. Stefanini et al., Phys. Rev. C **92,** 064607 (2015).
[5] C. L. Jiang et al., Phys. Rev. C **82,** 041601(R) (2010).
[6] A. Shrivastava et al., Phys. Rev. Lett. **103** 232702 (2009).
[7] A. Shrivastava et al., Phys. Lett. B **755,** 3326 (2016).
[8] M. Dasgupta et al., Phys. Rev. Lett. **99,** 192701 (2007).
[9] A. K. Sinha et al., Nucl. Instrum. Meth A **339,** 543 (1994).
[10] S. Nath, Comput. Phys. Commun. **180,** 2392 (2009).
[11] D. J. Hinde et al., Nucl. Phys A **385,** 109 (1982).
[12] A. K. Nasirov et al., Phys. Lett. B **686,** 72 (2010).
[13] K. Hagino, N. Rowleyi and A. T. Kruppa, Comput. Phys. Commun. **123,** 143 (1999).

5.1.15 Low-level nuclear structure study of ^{132}Ba using Coulomb excitation

S. Dutt[1], M. Saxena[2], R. Kumar[3], A. Jhingan[3], A. Agarwal[4], A. Banerjee[5], R. K. Bhowmik[3], C. Joshi[6], J. Kaur[7], A. Kumar[8], M. Matejska-Minda[2], V. Mishra[8], I. A. Rizvi[1], A. Stolarz[2], H. J. Wollersheim[9] and P. J. Napiorkowski[2]

[1]Department of Physics, Aligarh Muslim University, Aligarh 202002, India
[2]Heavy Ion Laboratory, University of Warsaw, Pasteura 5a, 02-093 Warsaw, Poland
[3]Inter University Accelerator Centre, Aruna Asaf Ali Marg, New Delhi 110067, India
[4]Department of Physics, Bareilly College, Bareilly 243005, India
[5]Department of Physics and Astrophysics, University of Delhi, Delhi 110007, India
[6]Department of Physics, M. S. University of Baroda, Vadodara 390002, India
[7]National Institute for Physics and Nuclear Engineering (IFIN-HH), 30 Reactourului, 077125 Bucharest-Magurele, Romania
[8]Department of Physics, Banaras Hindu University, Varanasi 221005, India
[9]GSI Helmholtzzentrum fur Schwerionenforschung GmbH, D-64291, Darmstadt, Germany

Nuclei in the transitional region $Z \geq 50$ and $N \leq 82$ are of vast interest as they show a large variety of co-existing structures. Doubly-magic 132Sn nucleus and nuclei close to this core nucleus are of key importance for the shell-model structure studies [1, 2]. In Te (Z = 52) isotopes, vibrational-like bands and two-quasiparticle excitations have been found to coexist [3, 4]. However, more proton rich nuclei, like Xe (Z = 54) and Ba (Z = 56), seem to develop a transitional path from spherical shapes to strong deformations. Thus, in the transitional $^{132\text{-}134}$Ba isotopes one could expect a possibility of interesting interplay between them.

Previous measurements on ^{132}Ba nucleus were performed long back in 1985 by Burnett et.al. [5] with a ^{12}C beam of 40 MeV energy. This energy of ^{12}C ions was well above the Cline's safe energy criteria [6], and hence the influence of nuclear interactions can't be neglected while determining the reduced transition probabilities. A Coulomb excitation experiment with ^{132}Ba (Z = 56, N = 76) target was performed at IUAC, New Delhi [3]. ^{58}Ni beam of 175 MeV was bombarded on ~40% isotopically enriched ^{132}Ba target of ≈ 500 μg/cm^2 thickness (on ≈ 20 μ g/cm^2 carbon backing) to Coulomb excite the target nuclei. The scattered beam particles and the recoils were detected in an annular parallel plate proportional counter (APPPC) [7], position sensitive for both the azimuthal ($\phi\mu$) and the polar (θ) angles. The APPPC was placed in the forward direction from the target position, covering an angular range of $15^\circ \leq \theta_{lab} \leq 45^\circ$ in the laboratory frame. The azimuthal (ϕ) angle was obtained from the cathode foil which was divided into 16 radial sections of 22.5° each. The de-exciting γ-rays were detected in the four clover detectors, having an energy resolution of about 2.5 keV, each mounted at angle ≈ 145° relative to the beam direction. The ϕ_γ angles for the clover detectors were ±45° and ±145° relative to the vertical direction.

Individual energies and timing from the 16 crystals were recorded in coincidence with the APPPC cathode (16 signals) event-by-event. The data were analyzed by using the GSI On-line Off-line Object Oriented (GO4) software package. Individual timing gates were applied for each crystal of Clover detectors and ϕ segments of APPPC to reduce the background radiation. A typical energy calibrated raw gamma-ray spectrum for a single crystal of Clover detector is shown in Fig. 5.1.23. The scattered particles and the recoils were detected in the annular parallel plate proportional counter (APPPC). The information of azimuthal angle (ϕ) was obtained by detecting the hit pattern in the azimuthal sector of the APPPC. However, the scattering angle θ was obtained from the time difference between the inner and outer contact of the delay lines.

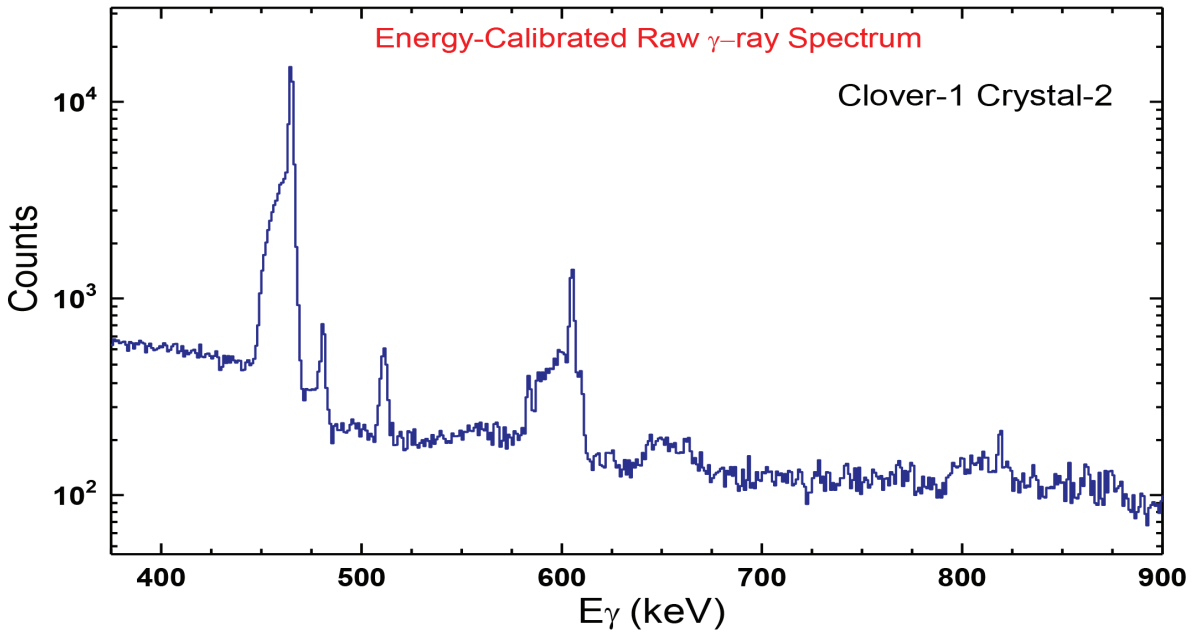

Fig. 5.1.23: Energy calibrated raw γ-ray spectrum obtained from a single crystal of a Clover detector.

Doppler shift correction of the measured γ-ray energies was performed event-by-event by using the information of scattering angles and Clover detectors' position. A γ-ray energy resolution of about 3.5 keV was obtained after Doppler shift correction for the target excitation. For distant collisions, first 2^+ state in ^{132}Ba was populated along with other stable Ba-isotopes, which were present as isotopic contamination in the target. Higher excited states 4_1^+ and 2_2^+ could also be populated in the close collisions between projectile and target nuclei. The Doppler-shift corrected γ-ray spectrum for a single crystal of Clover detector is shown in Figs. 5.1.24 and 5.1.25, for the two cases of distant and close collisions, respectively.

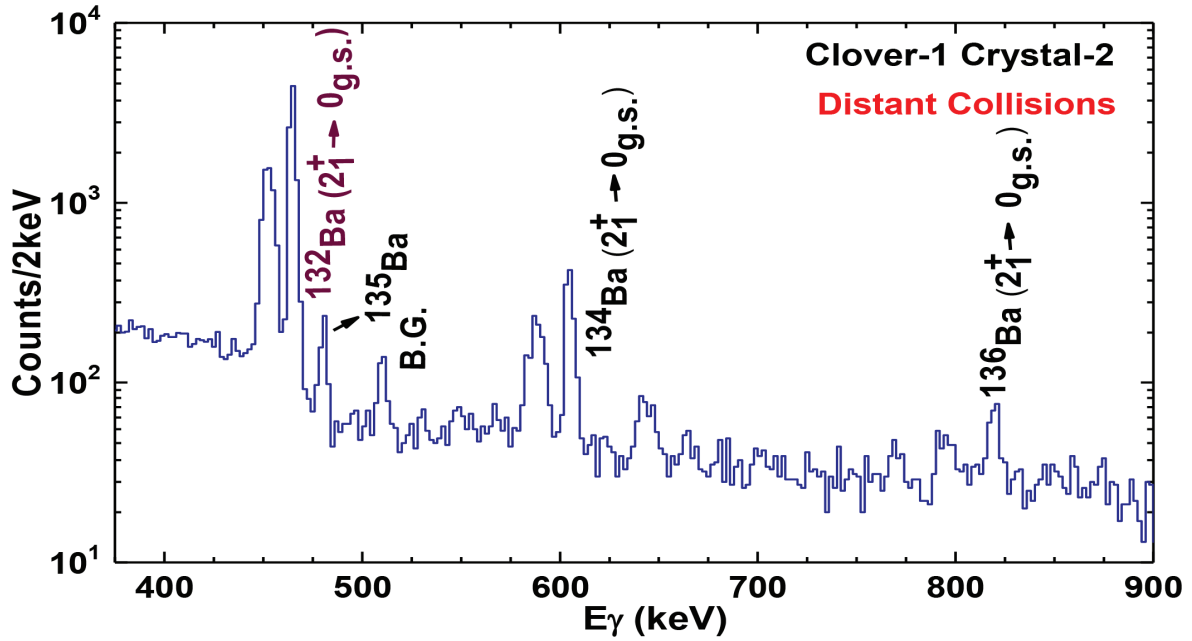

Fig. 5.1.24: Doppler-shift corrected γ-ray spectrum obtained from a single crystal of a Clover detector in coincidence with scattered projectiles detected in PPAC ($21.5^o \leq \theta_{c.m.} \leq 63.1^o$).

The excitation strength of the 2_1^+ state in ^{132}Ba was determined for distant collisions with respect to the first excited 2^+ state in ^{134}Ba, used for normalization. This normalization was further corrected for the different Clover-crystal efficiency and target enrichments. The theoretical cross-sections were calculated for a set of E2 matrix elements with the Winther-de Boer Coulomb excitation code [8]. The data were also examined for the re-orientation effects, but these effects were found to be negligible for the present nuclei. The matrix elements and B(E2↑) values of the $0_{g.s.} \rightarrow 2_1^+$ and $2_1^+ \rightarrow 4_1^+$ transitions have been determined and will be presented elsewhere. However, we couldn't observe $2_2^+ \rightarrow 0$g.s. gamma-ray with the IUAC set-up.

REFERENCES

[1] R. F. Casten, Nuclear Structure from a Simple Perspective (Oxford University Press, 2001).
[2] H. Grawe and M. Lewitowicz, Nucl. Phys A **693,** 116 (2001).
[3] T. Lonnroth et al., Physics Scripta **34,** 682 (1986).
[4] H. Sabri et al., Nucl. Phys. A **946,** 11 (2016).
[5] S. M. Burnett et al., Nucl. Phys. A **432,** 514 (1985).
[6] www.pas.rochester.edu/~Publications/annurev.ns.36.120186
[7] A. Jhingan et. al., Proc. DAE-BRNS Symp. Nucl. Phys. **61,** 966 (2016).
[8] A. Winther and J. de Boer, A computer program for multiple Coulomb excitation, in K. Alder and A. Winther, Coulomb Excitation (Academic Press, New York-London).

5.2 MATERIALS SCIENCE

A. Tripathi

The materials science research programmes in areas of ion beam induced materials modification and characterization are being carried out in a wide range of energies varying from tens of keV to hundreds of MeV. Studies on various type of materials: metallic, semiconducting and insulating and in different forms: nanostructures, thin film and bulk, are undertaken. This year there have been 45 user experiments over 135 shifts and these included 17 runs spread over 53 shifts which were BTA experiments associated with students' Ph.D. programmes. The experiments are mostly performed in the irradiation chamber in the materials science beamlines in beamhall-I, though experiments utilizing in-situ XRD facility were performed in materials science beamline in beamhall-II and experiments requiring low fluence irradiation were performed in GPSC. The users also utilized various synthesis techniques and offline characterization facilities such as XRD, AFM, SEM, Raman, UV-Vis, I-V, Hall measurement.

The formation of charge neutrality level in highly conducting Cadmium oxide (CdO) thin films in a series of experiments was demonstrated and the model was further verified by intentionally creating the defects by SHI irradiation. The low ion fluence SEE test facility at GPSC beam line was used to evaluate the radiation hardness of the digital and mixed signal CMOS ASICs designed and fabricated at SCL. For SEE testing of these ASICs, various ion beams of Si, Ni, Ti, and Ag with energies 100-140 MeV were used to vary linear energy transfer (LET). YCMO/SNTO p-n junctions irradiated using 100MeV O^{+7} ions show the asymmetric behavior along with two resistive states under the positive and negative bias modes suggesting the bipolar resistive switching (BRS) effect. As the TL sensitivity of crystalline Al_2O_3 is enhanced by doping with carbon, the anodized alumina has been exposed to 50 keV C^+ ions and shown to improve its TL response with a systematic rise in intensity with increasing fluence. The luminescence studies have been done for swift heavy ion and gamma irradiated rare earth doped $SrGd_2O_4$ and $BaGd_2O_4$ phosphors. Semi-insulating GaAs wafers implanted with 100 keV Si-1 ions showed the increase in absorption with ion fluence. The modification of surface morphology of Al doped ZnO (ZnO:Al) thin films using 120 MeV Ag^{+9} ions was studied for improving sensor sensitivity as the morphological modification of the sensor material increases its efficiency. The ferromagnetic τ-phase in MnAl alloy thin films was stabilized in 250 keV H+ ion beam irradiated thin films on Si and GaAs substrates. Polycrystalline yttria stabilized zirconia (YSZ) pellets were irradiated with 80 MeV Ag^{6+} ions to investigate its radiation tolerance against fission fragments at typical nuclear reactor temperature (850ºC). The results present strong evidence for the applicability of YSZ as an inert matrix fuel in nuclear reactors, with competitive effects of radiation damage (S_e) and dynamic thermal healing mechanisms. The energy loss and energy loss straggling of He, Li, C and O ions in Ni in the energy range ~ 0.25 – 7.00 MeV/n are measured and compared with the energy loss values predicted from most commonly used theoretical/semi-empirical formulations and energy loss straggling computed using Bohr, Lindhard-Scharff (LS), Bethe-Livingston (BL), Yang et al. and Titeica formulations. The irradiation of Graphene Oxide (GO) film with 120 MeV Au ions showed the annealing of GO film at lower fluences. Strain induced by 120 MeV Si^{9+} ion irradiation was found to affect the coercivity of $ZnFe_2O_4$. The kinetics of electronic excitations induced monoclinic-to-tetragonal phase transition in zirconium oxide films was studied by varying the density of EEs and the fluences of irradiation. 80 MeV Au, 0.25 MeV He, and 250 keV He were utilized in the study the radiation damage and H/D trapping in tungsten foils. Enhancement in mixing of Ni/Bi multilayers was observed with both 200 keV Ar ions and 100 MeV Au ions as a function of ion fluence. Controllability by low energy ion beam processing over shape, size and composition of nanostructures on Au-Si bi-layer was demonstrated.

Ion Beams in Materials Engineering and Characterization (IBMEC 2016) conference was hosted by Inter University Accelerator Centre along with Ion Beam Society of India in IUAC from 28th September to 1st October 2016. The conference was the continuation of SHIMEC (Swift Heavy Ions in Materials Engineering and Characterization) conference series being organized at IUAC but its scope has been widened to include the regime of low energy ions also. The conference had 17 invited, 19 oral and 74 poster contributions. The inaugural talk was given by Prof. T. Venkatesan from NUS, Singapore. The conference was preceded by an International school on ion Beams in Materials Science from September 22-27, 2017 with nearly 50 participants.

The proceedings of the 18th International Conference on Radiation Effects in Insulators (REI 18), which was co-hosted by IUAC were published in an special issue of NIM B journal (Vol 379, 2016) with 51 accepted papers.

5.2.1 Energy loss and straggling of swift heavy ions in varying thicknesses of Ni metal

Sunil Kumar[1], P.K. Diwan[1], S.A. Khan[2], D.K. Avasthi[3]

[1]Department of Applied Science, UIET, Kurukshetra University, Kurukshetra- 136119, India
[2]Inter-UniversityAccelerator Centre, Aruna Asaf Ali Marg, New Delhi - 110 067, India
[3]Amity Institute of Nanotechnology, Amity University, Noida-201 313, India

Ion beams are a powerful and versatile tool to modify and characterize the materials through Ion Beam based Analytical (IBA) techniques viz. RBS, NRA, ERDA etc. The energy loss profile of swift heavy ions obtained through these techniques is simulated mainly via SIMNRA, RUMP and NDF computer codes [1]. These codes are developed with the approximation that energy loss profiles are always Gaussian in shape and described in terms of average energy loss and energy loss straggling. Therefore, in order to use these codes, the accurate knowledge of both energy loss and straggling of heavy ions in different target materials is highly essential. Number of research group are involved to study these parameters both experimentally as well as theoretically. However, it is almost impossible to measure these parameters for all ion-target combinations, at various energies, because number of such combination is infinite. So, the only alternate is to use theoretical/semi-empirical formulations to predict these parameters. Further, before using these parameters as input in computer codes, the predicted values need to be authenticated through comparison with the measured values so that the most suitable theoretical formulation for such predictions can be identified. In the present study, energy loss and energy loss straggling of He, Li, C and O ions in Ni in the energy range ~ 0.25 – 7.00 MeV/n were measured utilizing 15 UD Pelletron-Accelerator facility at Inter-University Accelerator Centre (IUAC), New Delhi.

For comparison of measured energy loss values (dE/dx), the predicted values of most commonly used theoretical/ semi-empirical formulations [2,3] (Benton & Henke, Northcliffe – Schilling, Hubert et al., Diwan et al., ICRU report 73, MSTAR, CasP and SRIM code) were generated and presented in Fig.1(a), as a function of energy for He, Li, C and O ions in Ni metal. In case of energy loss straggling, measured values are compared (Fig.1(b)) with the computed values [4] based on Bohr, Lindhard-Scharff (LS), Bethe-Livingston (BL), Yang et al. and Titeica formulations.

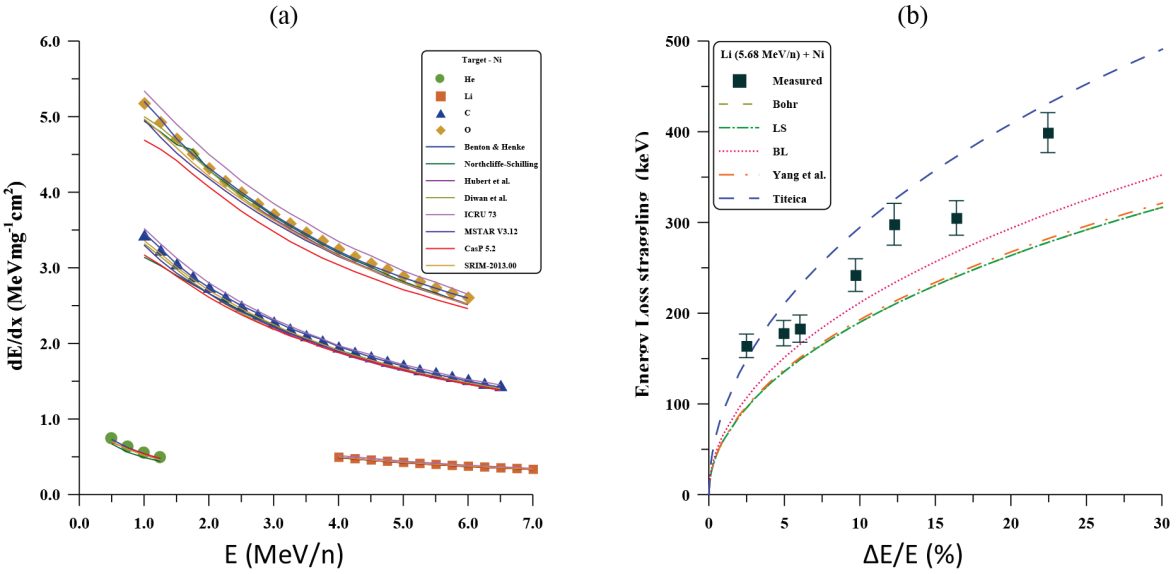

Figure 1(a) Energy loss and (b) energy loss straggling in Ni

Through such comparison, it is observed that the prediction of SRIM code for energy loss and Titeica theory for energy loss straggling are in good agreement with the presently measured values as compared to other theoretical/semi-empirical formulations.

REFERENCES

[1] M. Mayer, K. Arstila, U. Toussaint, Nucl. Instr. and Meth. Phys. Res. B 268 (2010) 1744 - 1748
[2] P.K. Diwan et al., Nucl. Instr. and Meth. Phy. Res. B 266 (2008) 4738 – 4741 and references therein.
[3] P.K. Diwan, Sunil Kumar, Nucl. Instr. and Meth. Phy. Res. B 359 (2015) 78 – 84 and references therein.
[4] Sunil Kumar, P.K. Diwan, J. of Radiation Res. and Appl. Sci. 8 (2015) 538-543 and references therein.

5.2.2 Single Event Effects Testing of Microelectronic devices using Swift Heavy Ions

Shammi Verma, Gaurav Srivastava, Sumit Soin, Parveen Rana, Y. Ram Kishore, Thakur Gurmeet Singh

Semi-Conductor Laboratory (SCL), Department of Space, Mohali, India

The intense heavy ions environment encountered in space applications can cause a variety of transient and destructive effects known as single event effects (SEE) which include single event latch-up (SEL), single event transient (SET), single event upset (SEU) and single event burnout (SEB). There are many device conditions and failure modes for a specific device due to SEE depending on the incident energetic particle. Different device effects, hard or soft errors, may or may not be acceptable foragiven device design & functionality. The low ion fluence (~$10^6 cm^{-2}$) SEE test facility at GPSC beam line, IUAC, Delhi was used to evaluate the radiation hardness of the digital and mixed signal CMOS ASICs designed and fabricated at SCL. APC based automatic test setup was developed for SEE testing of CCD Signal Processor, OBC 2.2, LVD STx, LVDS Rx, 16-bit Buffer and 16-bit Transceiver. The test setup comprised of DUT Board, 3-Channel Power Supply, Digital Storage Oscilloscope and computer loaded with Test Program. The data was acquired on PC using serial/parallel inter face. For SEE testing of these ASICs, various ion beams of Si, Ni, Ti, and Ag with energies 100-140 MeV were used to vary linear energy transfer (LET) from10-50 MeV-cm^2/mg. Table-1 summarizes the result highlights of the SEE testing performed on various ASICs. Figure 1 shows the cross-section for CSP and figure-2 shows the effect in CSP output due to upsets in registers.

Table 1 : Summary of SEE Tests performed onvarious ASICs and their results

Sr. No.	Device/ASIC Tested	Ion Beam Used	LET (MeV cm^2/mg)	Observations	Results
1	CCD Signal Processor (CSP)	Si	10.15	SEUs observed at LET of 20.56 MeV-cm^2/mg, how ever no SEL was observed upto LET~50.04 MeV-cm^2/mg.	ASIC is "pass" up to LET ~10.15 MeV-cm^2/mg in SEU and up to 50.04 MeV cm^2 /mg in SEL
		Ti	20.56		
		Ni	30.51		
		Ag	50.04		
2	OBC2.2	Si	10.15	No SEUs are observed in LET of 10.15 MeV-cm^2/mg. For LET of 20.56 MeV-cm^2/mg to 50.04 MeV-cm^2/mg, No SEUs are observed in Logic portion but SRAM showed the upsets.	ASICs passed up to LET ~10.15 MeV-cm^2/mg for SEU and up to 50.04 MeV-cm^2 /mg in SEL
		Ti	20.56		
		Ni	30.51		
		Ag	50.04		
3	LVDSTx&Rx	Ni	30.51	No SET/SEU/SEL were observed till LET ~50.04 MeV-cm^2/mg	Devices are passed up to LET of 50.04MeV-cm^2/mg
		Ag	50.04		
4	16-bit Buffer and 16-bit Transceiver	Ni	30.51	No increase in supply current and no SEU/SET/SEL were observed upto LET 50 MeV-cm^2/mg	Devices are passed up to LET of 50.04 MeV-cm^2/mg
		Ag	50.04		

OBC- On-Board Controller; LVDS Tx & Rx- Low Voltage Differential Signaling Transmitter and Receiver; CSP- CCD Signal Processor

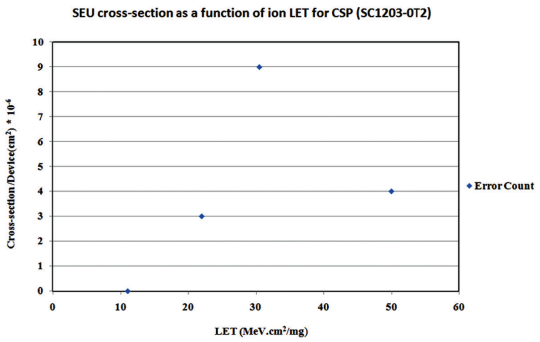

Fig.1 Cross-section and Bit-error versus LET graphs for CSP

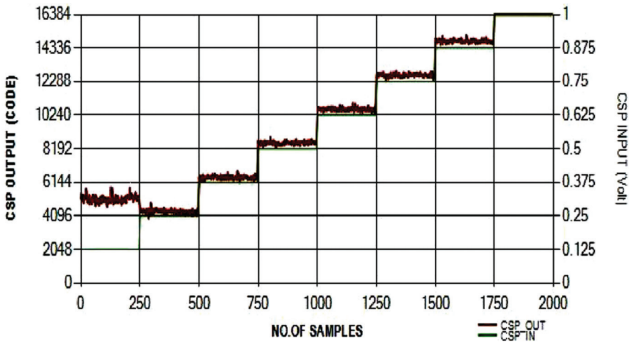

Fig. 2 Observed upsets in CSP registers under irradiation with 140 MeV Ag ion beam

5.2.3 Study of MnAl thin films

Himani Khanduri[1], S. A. Khan[1], S. K. Srivastava[2] and D. K. Avasthi[1]

[1]Inter-University Accelerator Centre, Aruna Asaf Ali Marg, New Delhi - 110 067, India
[2]Department of Physics,Indian Institute of Technology Kharagpur, Kharagpur- 721302, India

The tetragonal $L1_0$MnAl alloy with ferromagnetic τ-phase has a wide range of permanent magnet applications, from electric motors and generators to magnetic storage devices due to its large magnetic anisotropy, large saturation magnetization and high Curie transition temperature. In the bulk form, τ-phase is unstable and decomposes in β-Mn and γ-MnAl at room temperature. However, in thin film form τ-phase can be stabilized. There are many reports on the growth and magnetic properties of MnAl thin films [1-3].

Ion beam irradiation has been used in various studies to modify the structural as well as magnetic properties of thin films in recent years [4-5]. Ion irradiation at elevated temperature provides a rapid temperature rise and energy transfer, which can be extraordinarily useful for magnetic patterning [5]. In present study, we irradiated the as-deposited MnAl thin films by 250 keV protons in order to modify the structural and magnetic properties.

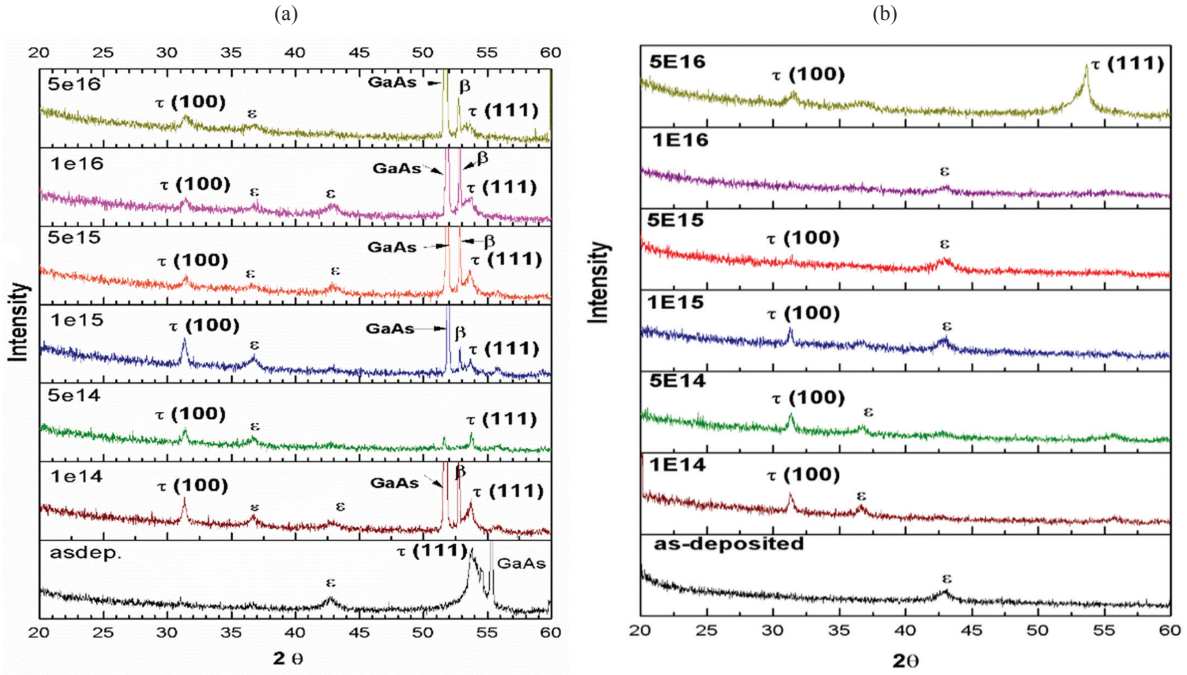

Fig 1. XRD patterns of as-deposited and irradiated (with fluences 1×10^{14}, 5×10^{14}, 1×10^{15}, 5×10^{15}, 1×10^{16} and 5×10^{16} ions/cm^2) MnAl thin films on (a) Si substrate and (b) GaAs substrate.

The MnAl thin films were deposited on Si and GaAs substrates by electron beam evaporation method at a pressure of order 10-7 mbar. MnAl alloy prepared by arc melt technique was used as source. MnAl alloy was prepared by taking Mn concentration 50% and Al concentration 50% during alloy preparation. These as-deposited MnAl thin films were irradiated by 250 keV protons beam with beam current of 1.5 μA to fluences of 1×10^{14}, 5×1014,

1×1015, 5×10^{15}, 1×10^{16} and 5×10^{16} ions/cm^2. X-ray diffraction (XRD) of as deposited and irradiated thin films have been carried out by using Bruker D8 Advance XRD.

The sample thickness and composition of as deposited thin film were measured by Rutherford backward spectroscopy using 2 MeV He ions. XRD pattern of 250 keV H^+ irradiated MnAl thin films reveal the presence of ε-phase in as-deposited MnAl thin film on Si and GaAs substrate as shown in Fig. 1. The τ (100) peak observed at 31.7° after irradiating the as-deposited films by 250 keV H^+ with fluences from 1×10^{14} to 5×10^{16} ions/cm^2. The XRD patterns of all the irradiated films show the presence of mixed τ and ε-phase. The MnAl thin film on Si substrate irradiated at fluence 5×10^{16} ions/cm^2 exhibit τ (100) and τ (111) diffraction peaks at 31.7º and 53.68º in the XRD pattern. This suggest that there is an enhancement of τ-phase in this film. The lattice parameter were calculated a=2.819 Å and c=3.294 Å from the 2θ valued of the (100) peak and (111) peak. Further analysis of the data is underway.

REFERENCES

[1] M. Hosoda et al., J. Appl. Phys. 111 (2012) 07A324
[2] T. L. Cheeks et al., J., Appl. Phys. Lett 60 (1992) 1393
[3] T. M. Rosier, Y. W. He and N. A. El-Masry Mater. Lett. 26 (1996) 227
[4] M. Abesaet al., Mater. Sci. Eng. C 23 (2003) 229–233
[5] C.-H. Lai, C. H. Yang and C.C. Chiang, Appl. Phys. Lett. 83 (2003) 4550

5.2.4 Ion-Beam Induced Annealing in Graphene Oxide Film

Chetna Tyagi[1], S.A. Khan[1], Indra Sulania[1], R. Meena[1], D.K. Avasthi[2] and Ambuj Tripathi[1]

[1]Inter-University Accelerator Centre, Aruna Asaf Ali Marg, New Delhi - 110 067, India
[2]Amity Institute of Nanotechnology, Amity University, Noida, Sec-125, Uttar Pradesh, India-201313.

The properties of Graphene oxide (GO) can be tuned by modifying the ratio of sp^2 and sp^3 hybridization [1] using ion beam irradiation. However, the inherent defects present in GO during its production deteriorate its properties. Our group has earlier demonstrated annealing of defects in carbon nanostructures (fullerene, CNT and graphene) [2-4] at lower fluence of swift heavy ion (SHI) irradiation. In the present work, we have studied irradiation of GO film with 120 MeV Au ions to fluences ranging from 10^{10} to 10^{13} ions/cm^2. In-situ XRD measurements and Raman Spectroscopy (Figure 1) showed the annealing of GO film at lower fluences. The irradiated samples showed an increase in the intensity of aromatic carbon bonds evident from Fourier Transform Infrared (FTIR) and UV-Vis spectroscopy indicating the increase in graphitic regions and sp^2 hybridization.

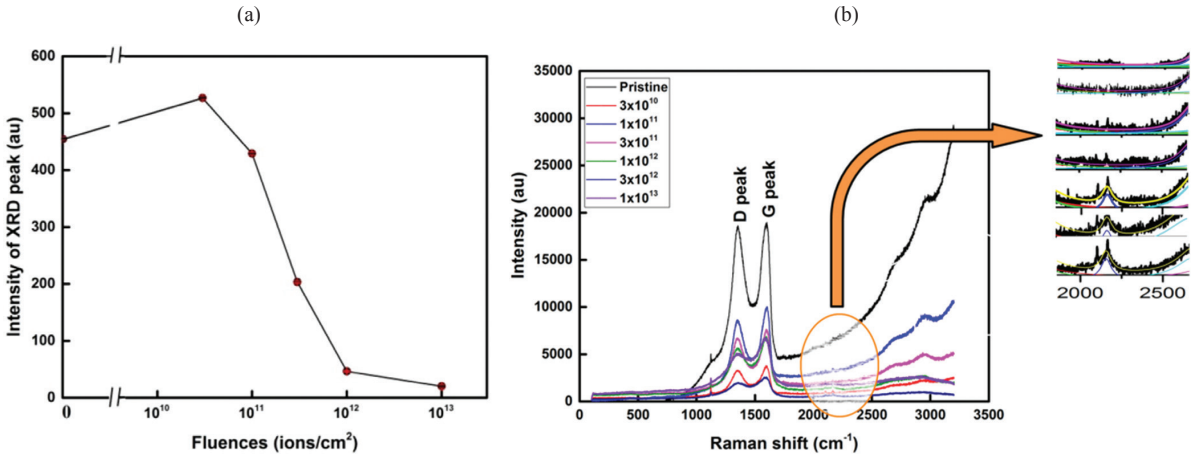

Figure 1(a) Plot of intensity of XRD peak varying with fluences and (b) Raman spectra of GO samples irradiated with 120 MeV Gold ion beam to different fluences

REFERENCES

[1] W. Choi et al., Critical Reviews in Solid State and Materials Sciences 35.1 (2010) 52-71
[2] R. Singhal et al., Journal of Applied Physics 107.10 (2010) 103504
[3] A. Kumar et al.,Thin Solid Films 517.15 (2009) 4322-4324
[4] S. Kumar et al., Nanoscale Res. Lett. 9 (2014) 126

5.2.5 Electrochemical performance of reduced graphene oxide – polypyrrole nanotubes nanocomposites and 85 MeV C^{6+} ion irradiation

Madhabi Devi and A. Kumar

Material Research Laboratory, Dept.t of Physics, Tezpur University, Napaam, Tezpur-784028, Assam, India

Nanocomposites of reduced graphene oxide (RGO) nanosheets and polypyrrole nanotubes (PPyNTs) have been synthesized by in-situ reduction of graphene oxide in presence of PPyNTs as spacers. In-situ chemical reduction of GO in appropriate conducting polymer (CP) solutions can prevent their restacking and restore the conductivity of RGO because of the presence of CP in their solutions during the reduction [1]. The nanocomposites exhibit high specific capacitance and good electrochemical stability as electrode material for supercapacitors. The specific capacitance gradually increases to 299 F g^{-1} with the increase in feeding of RGO and the capacitive retention is about 77.28 % of the initial capacitance after 1000 cycles. A maximum energy density of 24 W h kg^{-1} and power density of 192 W kg^{-1} are achieved by utilizing the surface area of RGO nanosheets with the help of PPyNTs as spacers [2]. The synergistic effect between CP nanostructures and RGO increases the specific capacitance of the nanocomposites by simultaneously combining two kinds of charge storage mechanisms; (i) Pure electrostatic attraction between ions and the charged electrode surface (i.e. EDL capacitance) and, (ii) Faradic pseudocapacitance arising from PPy redox reactions [3]. The specific capacitance of PPyNTs and RGO-PPyNTs nanocomposites is calculated from the galvanostatic charge-discharge curves which are shown in Figure 1(i) and the cyclic stability after 1000 cycles of the nanocomposite showing the highest capacitance is shown in Figure 1(ii). The formula used for calculating their specific capacitances is given by

$$C_{sp} = \frac{I \times \Delta t_d}{m \times \Delta V}$$

where, I is the constant discharge current, m is the mass of the electrode material, ΔV is the potential drop during discharge, and Δt_d and Δt_c are the discharging and charging duration, respectively. The specific capacitances of pure PPyNTs and RGO-PPyNTs nanocomposites with 5, 10, 20 and 40 wt. % of RGO are estimated to be 128.02, 164.39, 197.09, 238.73 and 299.81 F g^{-1}, respectively.

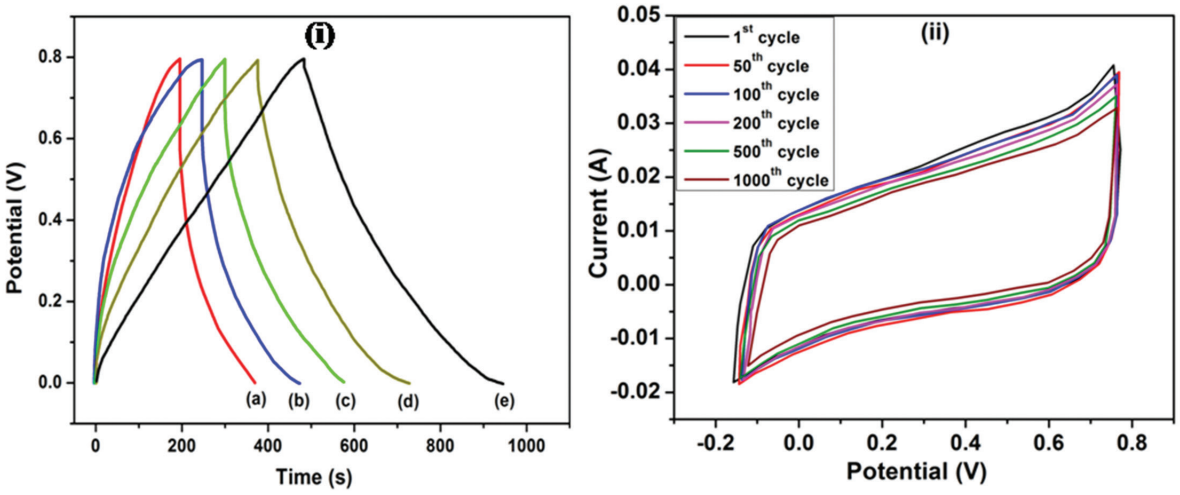

Figure 1: (i) Galvanostatic charge-discharge curves of (a) PPyNTs and RGO-PPyNTs nanocomposites with (b) 5 wt. %, (c) 10 wt. %, (d) 20 wt. % and (e) 40 wt. % of RGO at a current density of 0.5 A g^{-1};
(ii) CV curves with increasing cycle number of 40 wt. % RGO-PPyNTs nanocomposite.

Based on the highest electrochemical performance, the nanocomposite with 40 wt. % of RGO was chosen to irradiate with 85 MeV C^{6+} ions with a view to study the fluence dependent electrochemical properties of the nanocomposite. The nanocomposite films of 1 × 1 cm^2 size were subjected to SHI irradiation using the 15 UD tandem Pelletron accelerator at IUAC, New Delhi. The nanocomposite films were irradiatied with 85 MeV C^{6+} ion beam to four different fluences of 6×10^{10}, 3.6×10^{11}, 2.2×10^{12} and 1.3×10^{13} ions/cm^2 keeping the beam current constant at 1 pnA (particle-nanoAmpere). The energy used for irradiation was evaluated from Stopping and Range of ions in Matter (SRIM) software in such a way that the projected range of C^{6+} ions was much greater than the estimated thickness of the nanocomposite films so that the ions passed through the films and were not implanted. The study of the fluence dependent electrochemical properties of 40 wt. % RGO-PPyNTs nanocomposite will be presented in the next annual report.

REFERENCES

[1] J. Du *et al.,* Macromol. Chem. Phys. 213 (2012) 1060
[2] M. Devi *et al.,* Synth. Met. 222 (2016) 318
[3] N.A. Kumar *et al.,* Chem. Commun. 50 (2014) 6298

5.2.6 Tailoring magnetic properties of $ZnFe_2O_4$: Effect of 120 MeV Si^{9+} ion

R. Sharma[1], S. Raghuvanshi[1], S. A. Khan[2], P. N. Prakash[2], D. K. Avasthi[3] and S. N. Kane[1]

[1]Magnetic Materials Laboratory, School of Physics, D. A. University, Khandwa road Campus, Indore-452001, India
[2]Inter-University Accelerator Centre, Aruna Asaf Ali Marg, New Delhi - 110 067, India
[3]Amity University, Noida 201313, Uttar Pradesh, India

Effect of ion irradiation (120 MeV $28Si^{9+}$,fluence ranging between 1×10^{12} – 1×10^{14} ions/cm^2) on the structural, magnetic properties of $ZnFe_2O_4$ (annealed at 450 ºC/3hr) prepared by sol-gel auto-combustion method is reported. X-ray diffraction (XRD), vibrating sample magnetometer (VSM), SEM-EDS were used to monitor irradiation induced changes in the studied samples. XRD (shown in fig1 a) analysis shows single phase cubic spinel, and no other phases are produced due to irradiation. Obtained marginal change in experimental lattice parameter a_{exp}. depicts that samples retain structural integrity even after highest dose, revels their radiation resistance ability, as also reported in Reference [1]. Close matching of theoretical lattice parameter $(a_{th.})$, $a_{exp.}$ (table I) shows that the obtained cation distribution is close to real one [2]. Ion irradiation induced increase of x-ray density (ρ_{xrd}) is attributed to reduction of free volume. SEM images (fig.1 b, c) show in-homogeneous particle size distribution in pristine, irradiated samples. Obtained migration of Zn^{2+}, Fe^{3+} ions on A, B-site is consistent with theoretical magnetization $(M_{(t)})$, experimental magnetization $(M_{S(exp)})$. Linear increase of M(t), MS (exp) (fig 1d) with oxygen positional parameter(u) depicts disorder induced magnetization in the samples. This result shows the usefulness of ion irradiation in tailoring magnetic properties. Grain diameter $D_{W\text{-}H}$ (obtained by Williamson Hall plot) remains practically un-changed after irradiation, although irradiation results in changes in strain (range between 6.93×10^{-4} – 9.15×10^{-4}). Ion irradiation induced changes in strain affects coercivity (H^c), as shown in fig. 1 e, attributed to the changes in domain wall movements in the studied samples.

Table I: Irradiation dependence of structural parameters.

Fluence (ions/cm^2)	$a_{exp.}$(in nm)	$a_{th.}$(in nm)	$D_{W\text{-}H}$(in nm)	ρ_{xrd}(in kg/m^3)
0	0.8430	0.8434	16.9	5345.6
1×10^{12}	0.8421	0.8421	16.9	5361.3
1×10^{13}	0.8422	0.8430	15.9	5360.3
1×10^{14}	0.8411	0.8423	16.2	5382.1

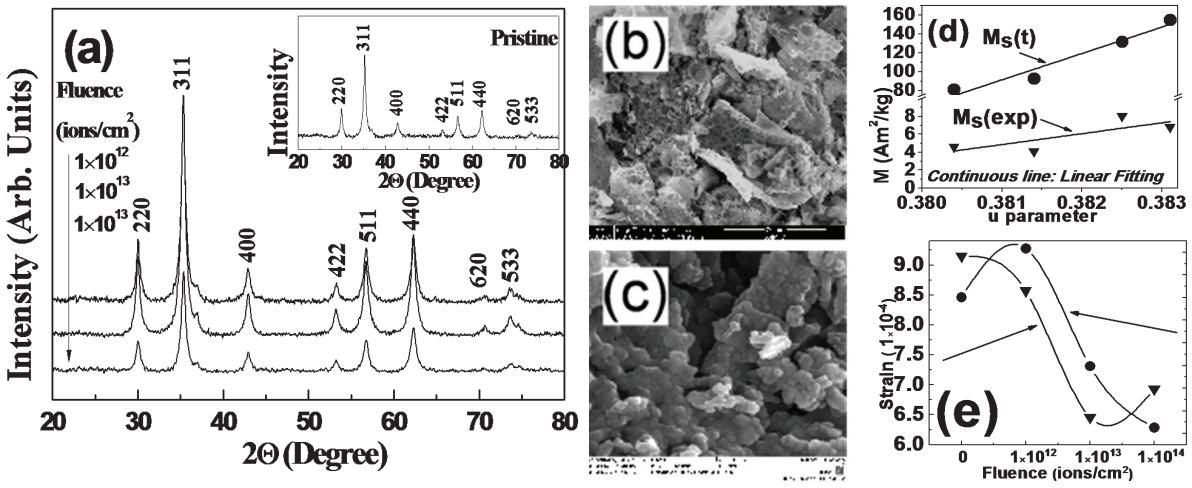

Fig. 1: (a) XRD pattern of irradiated samples, Inset: XRD pattern of pristine sample, (b) and (c) SEM image of pristine, irradiated sample (1×10^{14} ions/cm^2), (d) variation of M with u (e) Strain, HC variation with fluence.

REFERENCES
[1] M. Satalkar, S. N. Kane, P. K. Kulriya, D. K. Avasthi, Nucl. Inst. Meth. B 379 (2016) 235
[2] M. Satalkar, S. N. Kane, M. Kumaresavanji, J. P.Araujo, Mater. Res. Bull. 91 (2017) 14

5.2.7 Effect of temperature in the radiation stability of yttria stabilized zirconia under swift heavy ions irradiation

Parswajit Kalita[1*], Santanu Ghosh[1], Gael Sattonnay[2], Udai B. Singh[1], Vinita Grover[3], Rakesh Shukla[3], S.Amirthapandian[4], Pawan Kulriya[5], Ramcharan Meena[5], A.K. Tyagi[3] and D.K. Avasthi[5,6]

[1]Department of Physics, Indian Institute of Technology Delhi, New Delhi – 110016, India
[2]CSNSM, University of Paris Sud, Bat 108 F-91405, Orsay Cedex, France
[3]Chemistry Division, Bhabha Atomic Research Centre, Mumbai – 400085, India
[4]Materials Physics Division, Indira Gandhi Centre for Atomic Research, Kalpakkam -603102, India
[5]Inter-University Accelerator Centre, Aruna Asaf Ali Marg, New Delhi - 110 067, India
[6]Amity University, Noida – 201313, India

Polycrystalline yttria stabilized zirconia (YSZ) pellets were irradiated with 80 MeV Ag^{6+} ions to investigate its radiation tolerance against fission fragments. To better simulate a nuclear reactor environment, the irradiations were carried out at typical nuclear reactor temperature (850ºC). For comparison, irradiations were also performed at room temperature. All irradiations were carried out at the Materials Science beam-line using the 15UD Pelletron accelerator at IUAC, New Delhi. Grazing incidence X-ray diffraction (GIXRD) (Figure 1 (a)) and Raman spectroscopy measurements reveal degradation in crystallinity for the room temperature irradiated samples. No bulk structural amorphization was however observed, whereas defect clusters were formed as indicated by transmission electron microscopy (TEM). A significant reduction of the irradiation induced defects/ damage, i.e. improvement in the radiation tolerance, was seen under irradiation at 850 ºC (Figure 1(b)). This is attributed to the fact that the rapid thermal quenching of the localized hot molten zones (arising from spike in the lattice temperature upon irradiation) is confined to 850 ºC thereby resulting in the reduction of the defects/ damage produced. Our results present strong evidence for the applicability of YSZ as an inert matrix fuel in nuclear reactors, where competitive effects of radiation damage (Se) and dynamic thermal healing mechanisms may lead to a strong reduction in the damage production and thus sustain its physical integrity.

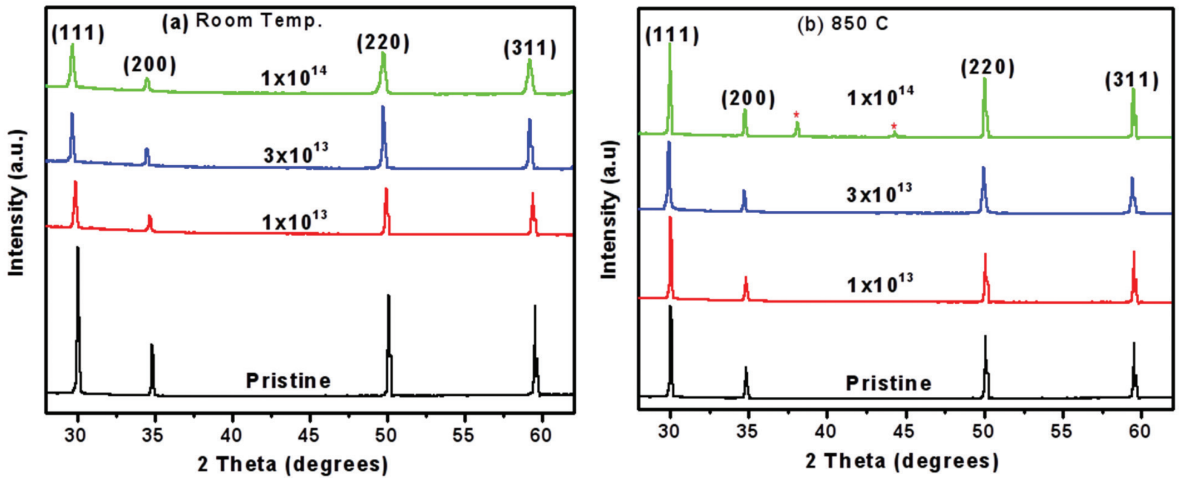

Figure 1. GIXRD patterns of the pellets irradiated with different fluences at (a) room temperature and (b) 850ºC. All fluences are given in ions/cm^2.

In addition, YSZ poly-crystals with varying microstructure were irradiated with 80 MeV Ag6+ ions at room temperature and 1000 K at the Materials Science beam-line using the 15UD Pelletron accelerator at IUAC, New Delhi. The analysis of the effects of irradiation are in progress.

REFERENCES
[1] Parswajit Kalita et al., J. of Appl. Phys. 122 (2017) 025902

5.2.8 Morphological modification of ZnO:Al thin film using swift heavy ion irradiation

Susanta Kumar Sahoo[1], Sutanu Mangal[1], Fouran Singh[2], Udai P. Singh[3]

[1]School of Applied Sciences, KIIT University, Bhubaneswar 751024, Odisha, India

[2]Inter-University Accelerator Centre, Aruna Asaf Ali Marg, New Delhi - 110 067, India
[3]School of Electronics Engineering, KIIT University, Bhubaneswar, Odisha, India, 751024

The gas sensitivity depends on the reducing and adsorbing ability of the detected gas on the surface of the material [1]. The grain size and porosity related changes of the surface material have a role to increase the gas response [2]. So, morphological modification of the sensor material increases the efficiency of the sensor material. The oxides are good sensor materials towards the reducing gases. In the present work, the modification of surface morphology of Al doped ZnO (ZnO:Al) thin films using swift heavy ion (120 MeV Ag^{+9}) irradiation to different fluences ranging from 3×10^{11} ions/cm^2 to 3×10^{13} ions/cm^2 is reported.

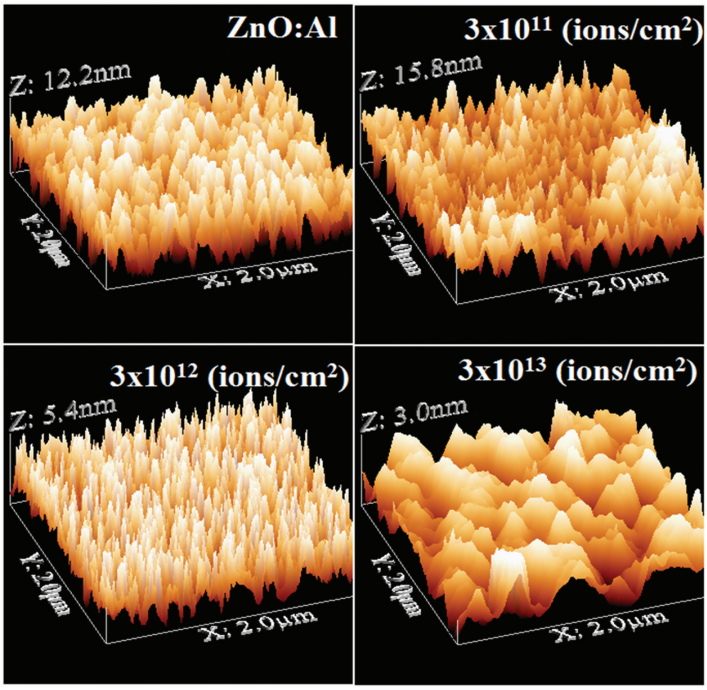

Fig. 1 Atomic force micrographs of pristine and irradiated ZnO:Al thin films

Al doped ZnO films were deposited on the glass substrates using RF magnetron sputtering. The thicknesses of the films were 500±10 nm, as measured by Filmetric thin film analyser. The surface morphology of the materials was investigated by atomic force microscopy (AFM) as shown in Fig. 1. The RMS roughness decreases with fluences upto 3×10^{13} ions/cm^2 (Table 1). The discontinuous tracks and defects reduce the sample roughness [3]. The fragmentations of particles are clearly observed in the irradiated films. The different structures developed due to irradiation. This can be used to optimize the fluences for material modification as per need in sensor devices.

Table 1 RMS roughness of the pristine and irradiated samples

Fluence (ions/cm2)	Pristine	3×10^{11}	3×10^{12}	3×10^{13}
RMS Roughness (nm)	2.87	3.44	1.26	0.66

REFERENCES

[1] Bai Shouli et al., Sensors and Actuators B 174 (2012) 51–58
[2] K. Galatsis et al., Sensors and Actuators B 83 (2002) 276–280
[3] R. Kumaravel et al., Radiation Physics and Chemistry 80 (2011) 435–439

5.2.9 Electronic structure modification and Fermi level shifting in Niobium doped anatase Titanium dioxide thin films

Subodh K. Gautam[1], Arkaprava Das[1], S. Ojha[1], D. K. Shukla[2], D.M. Phase[2] and Fouran Singh[2]

[1]Inter University Accelerator Centre, Aruna Asaf Ali Marg, New Delhi-110067, India
[2]UGC-DAE Consortium for Scientific Research, University Campus, Khandwa Road, Indore 452017, India

Electronic structure modification and Fermi level shifting in Niobium doped anatase Titanium dioxide thin films as a comparative study of NEXAFS, work function and stiffening of phonons were reported. This study reports the effect of swift heavy ions (SHIs) irradiation induced modification of structural, optical and electronic structure properties along with the stiffening in low frequency E1g Raman mode and Fermi level shifting by SHI induced different density of electronic excitations. The shifting of Fermi level and modification of electronic structure are understood in term of work function modification and reduction of hybridized O 2p and T 3d unoccupied states in conduction band. The reduction of hybridized state and stiffening behavior of E1g Raman mode along with decrease in work function are explained in terms of nano-crystallization followed by amorphization in NTO lattice induced by continuous and discontinuous amorphous ion tracks containing intestinally created defects and non-stoichiometry in the lattice. Moreover, the investigations on highly stable and crystalline anatase TiO_2 films and Nb_2O_5 -anatase TiO_2 NCs films are a topic of interest for studying the phase stability and/or phase transformation (PT) under different density of electronic excitations (EEs). It is also reported that SHI irradiation induces crystalline to crystalline phase transformation and amorphization in same system at different density of EEs. Results are explained in terms of continuous and discontinuous track formation and its effect on PT are investigated by calculations in the framework of in-elastic thermal spike model. These studies are very appropriate for better insights of electronic structure modification during phase transformation and controlled Fermi level shifting, which plays a crucial role in controlling the charge carrier injection efficiency in opto-electronic applications [for details, see *Phys. Chem. Chem. Phys. 18 (2016) 3618*].

5.2.10 Carrier Transport Mechanism an ultra-sensitive Niobium Doped Titanium Dioxide/p-Si Heterojunction Photodiode under illumination by solar simulated light

Subodh K. Gautam[1], Arkaprava Das[1], R.G. Singh[2], V.V. Shiva Kumar[1] and Fouran Singh[1]

[1]Inter University Accelerator Centre, Aruna Asaf Ali Marg, New Delhi -110067, India
[2]Department of Physics, Bhagini Nivedita College, Delhi University, Delhi– 110043, India

Based on the study reported in *Phys. Chem. Chem. Phys. 18 (2016) 3618,* an ultra-sensitive Niobium Doped Titanium Dioxide/p-Si Heterojunction Photodiode wasdeveloped and the Carrier Transport Mechanism was investigated. Nano-crystalline Nb doped anatase TiO_2 (NTO) thin film was deposited on p-type Si substrate for fabrication of n-NTO/p-Si heterojunction photodiode using RF magnetron sputtering technique. The current density–voltage (J–V) characteristics of n-NTO/p-Si heterojunction diode in ±5V bias range was measured under dark and simulated solar light illumination conditions and important diode parameters of n-NTO/p-Si heterojunction diode such as ideality factor, barrier height and series resistancewere determined. Diode exhibited excellent behavior under dark condition as rectification ratio is found to be ~7 $\times 10^2$ with high forward current ~1.54 A/cm^2 at 5V. The n-NTO/p-Si heterojunction works as an efficient photodiode in reverse bias under simulated solar light illumination shows open circuit voltage (V_{oc}) of about 200 mV with high contrast ratio ~225 at -2V and very high photo responsivity ~2.7 A/W at -5V. The very high responsivity of photodiode is mainly due to the generation of high density electron-hole plasma in NTO depletion region by the absorption of incident UV range photons. Charge transport mechanism of n-NTO/p-Si heterojunction diode is explained with the help of energy band diagram under equilibrium at zero bias and under solar illumination in reverse bias conditions [for details, *seeJ. Appl. Phys. 120, (2016) 214502*]. This photo-diode is then tested for their reliability and Radiation Stability under SHI irradiation for their possible applications in radiation environments such as space, nuclear reactors, particle accelerators, and military equipments. Results depict that dark reverse current on indirect irradiated photodiode enhanced ~18 times under solar light illumination and the contrast ratio (the ratio of photocurrent (I_{Ph}) to dark current (I_{dark}) at particular bias voltage) of diode is high ~50 at -0.5 V and decreases with increasing applied voltage. The detailed investigation is under progress for their in-depth understanding.

5.2.11 Formation of charge neutrality level in highly conducting Cadmium oxide (CdO) thin films: role of doping and irradiation

Arkaprava Das[1], Subodh K. Gautam[1], Dinesh K. Shukla[2], and Fouran Singh[2]

[1]Inter-University Accelerator Centre, Aruna Asaf Ali Marg, New Delhi - 110 067, India
[2]UGC-DAE Consortium for Scientific Research, University Campus, Khandwa Road, Indore 452017, India

A series of investigations on the formation of charge neutrality level (CNL) in highly conducting Cadmium oxide (CdO) thin films is demonstarted by the observed variation in the band gap upon annealing and doping.

It may be explained by the observation that tin (Sn) doping breaks the perfect periodicity of CdO cubic crystal structure and creates virtual gap states (ViGS). The level of local CNL resides at the branch point of ViGS, making the energy at which native defect's character changes from predominantly donor-like below CNL to predominantly acceptor-like above the CNL and a schematic band diagram is developed to substantiate the same. Further investigations using soft x-ray absorption spectroscopy (SXAS) at Oxygen and Cadmium edge show the reduction of Sn^{4+} to Sn^{2+}. The analysis of the spectral features has revealed an evidence of *p-d* interaction between O 2*p* and Cd 4*d* orbitals [*Nature Scientific Reports 7 (2017) 40843*]. The validity of our proposed model is further verified by intentionally creating the defects by SHI irradiation [*Materials Research Express 4 (2017) 045901*].

5.2.12 Micro-Raman and electronic structure study on kinetics of electronic excitations induced monoclinic-to-tetragonal phase transition in zirconium oxide films

Mukesh Rawat[1], Arkaprava Das[2], D.K. Shukla[3], Parasmani Rajput[4], A. Chettah[5], D.M. Phase[3], R.C. Ramola[1] and Fouran Singh[2]

[1]Department of Physics, BadshahiThaul Campus, H.N.B.Garhwal University, Tehri Garhwal 249199, India
[2]Inter-University Accelerator Centre, Aruna Asaf Ali Marg, New Delhi - 110 067, India
[3]UGC-DAE Consortium for Scientific Research, University Campus, Khandwa Road, Indore 452017, India
[4]Atomic & Molecular Physics Division, Bhabha Atomic Research Center, Trombay, Mumbai 400085, India
[5]LGMM Laboratory, Université 20 Août 1955-Skikda, BP 26, 21000 Skikda, Algeria

Study of phase transformations (PT) by electronic excitations (EEs) induced by swift heavy ion (SHI) irradiations is an important topic of research. Zirconium oxide (ZrO_2) is known to exhibit Monoclinic –to-tetragonal PT induced by swift heavy ion (SHI) irradiation. In the present work, such PT along with its kinetics in sputter grown ZrO_2 films on silicon substrates by EEs is reported. The density of EEs and the fluences of irradiation were varied for the better insight of phase transformation kinetics. The phase transition is well evident from the investigations using grazing incidence x-ray diffraction (GIXRD) and micro-Raman spectroscopy (mRS). Studies reveal a PT from the monoclinic to tetragonal phase. It is noted that at high fluence of Ag ion irradiation, partly PT to cubic phase is also observed. However, it is clear from this study that this PT is not only due to transient temperature induced by SHI, but also attributed to the strain in the lattice created under the influence of the induced density of defects in the lattice. Interestingly, it may be noted that strain is well evident by the stiffening of the characteristic Raman modes of monoclinic phase. The modifications in electronic and local structure releaved using soft x-ray absorption spectroscopy (XAS) and x-ray absorption fine structure (XAFS) and found after fitting of Zr K-edge XAFS thatphase transformation from m-ZrO_2 to t-ZrO_2 and/or c-ZrO_2 occurs upon Ni and Ag irrdaitation. Studies would elucidate a deeper understanding about the kinetics of PT under such non-equilibrium conditions. [*for details, see RSC Advances 6 (2016) 104425*].

5.2.13 Band gap engineering and low temperature transport phenomenon in highly conducting antimony doped tin oxide thin films

M.P.S.Rana[1], Fouran Singh[2], S. Negi[1], Subodh K. Gautam[1], R.G. Singh[3] and R.C. Ramola[1]

[1]Department of Physics, H.N.B.Garhwal University, BadshahiThaul Campus Tehri Garwal-249199, India
[2]Inter-University Accelerator Centre, Aruna Asaf Ali Marg, New Delhi - 110 067, India
[3]Department of Physics, Bhagini Nivedita College, University of Delhi -110023, India

A huge band gap tuning and low temperature transport phenomenon in highly transparent antimony doped tin oxide thin film (Sb:SnO_2) under the influence of swift heavy ions irradiation (SHII) is reported. Structural analysis shows an enhancement in crystallinity at initial fluence of irradiation followed by amorphization at higher fluences. Films were also well studied for their surface morphology by atomic force microscopy and scanning electron microscopy. Band gap analysis reveals a drastic band gap narrowing around 1.1 eV upon SHI irradiation. Transport measurements show that the high conductivity and the carrier concentration decrease upon increase in the fluence of irradiation. The mechanism of charge carrier transport were investigated at low temperature is attributed to nearest neighbour hopping (NNH) and variable range hopping (VRH) in different temperature regimes. Origin of the band gap tuning is understood in framework of Burstein-Moss (BM) shift, Quantum Confinement (QC) effect and band-tailing states in amorphous semiconductors. [for details, see *Ceramics International 42 (2016) 5932*].

5.2.14 Studies on Structure & Properties of Functional Oxides

Hetal Kundalia[1], Brinda Vyas[1], Malay Udeshi[1], Indra Sulania[2], K. Asokan[2], Fouran Singh[2], Saif A. Khan[2] and D.G. Kuberkar[3]

[1]Department of Physics, Saurashtra University, Rajkot-360005, India
[2]Inter-University Accelerator Centre, Aruna Asaf Ali Marg, New Delhi - 110 067, India
[3]Department of Nanoscience and Advanced materials, Saurashtra University, Rajkot-360005, India

A series of Cu & Zn doped $NdMnO_3$ (NMO) samples [$NdMn_{1-x}MxO3$ (M = Cu & Zn) (x = 0, 0.05, 0.10, 0.20)] were synthesized using conventional Solid State Reaction (SSR) route and structural characterization was carried out using PANalytical X-ray Diffractometer at Saurashtra University, Rajkot. All the samples possess orthorhombic structure with space group *Pnma* (no. 62). Energy Dispersive X-ray Spectroscopy (EDX) measurements were carried out using IUAC, New Delhi facility confirming the stoichiometry for all the samples. Temperature dependent dielectric measurements recorded using IUAC, New Delhi facility on all the samples show relaxation behaviour in loss spectra (Figure 1(a)). To understand the evolution of grain and grain boundary, Scanning Electron Microscopy (SEM) measurements were taken at IUAC, New Delhi, which show well developed grain morphology in all the samples. Room temperature Raman spectroscopy measurements were performed on $NdMn_{1-x}MxO_3$ (M = Cu & Zn) (x = 0, 0.05, 0.10, 0.20).

Ceramic composites of (1-*x*)ZnO-*x*$BaTiO_3$ (x=0.2,0.3,0.4,0.5) were synthesisized using conventional solid state reaction (SSR) route.The starting materials were in the form of ZnO and $BaTiO_3$ powders. Room temperature Raman spectroscopy measurement taken on ZnO, $BaTiO_3$ (BTO), (1-*x*)ZnO–xBTO (*x*= 0.2, 0.3, 0.4, 0.5) systems at IUAC, New Delhi show shift in Raman modes with composition. Thickness measurements of NMO/Si, ZnO/Si and BTO/Si films were taken using Stylus profilometer facility at IUAC, New Delhi.

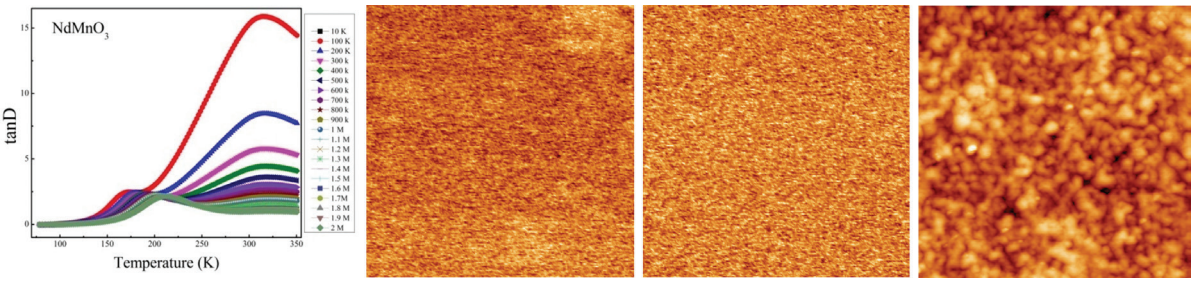

Figure 1. (a) tanδ vs temperature plot of bulk NMO and AFM images of (b) pristine NMO/LSAT films and filmsirradiated to fluences (c)5×10^{10}ions/cm^2 and (d)5×10^{12}ions/cm^2.

Thin films of $NdMnO_3$ were deposited on single crystalline LSAT substrate using PLD facility. All the NMO/LSAT films (200 nm) were irradiated with 200 MeV Ag^{+15} ions to ~ 5×10^{10}, 5×11^{11} and 5×12^{12} ion/cm^2 fluences, using the 15 UD Tandem Accelerator facility at Inter University Accelerator Centre (IUAC), New Delhi. Structural properties of the pristine and irradiated films were studied using PANalytical X-ray Diffractometer. AFM micro-structural study carried out reveal average RMS roughness decreases for the minimal fluence of irradiation 5×10^{10} and increases till the fluence of 5×10^{12}ions/cm^2. This is due to smoothening of films at lower fluence due to irradiation, whereas at higher fluence surface roughness increased due to the defects (Figure 1(b)-(d)).

5.2.15 Influence of electronic excitations on structural, optical and electrical properties of undoped and antimony doped tin oxide thin films

M. P. S. Rana[1], Fouran Singh[2], Kanchan Joshi[1], Sandhya Negi[1] and R. C. Ramola[1]

[1]Dept. of Physics, H.N.B.Garhwal University, BadshahiThaul Campus Tehri Garwal-249199, India
[2]Inter-University Accelerator Centre, Aruna Asaf Ali Marg, New Delhi - 110 067, India

Study reports on the influence of swift heavy ion irradiation (SHII) induced electronic excitations (EEs) on structural, optical and electrical properties of undoped SnO_2 (TO) and antimony doped SnO_2 (ATO) thin films. EEs in the thin films were induced by 70 MeV Si ion irradiation. It is noticed from the structural analysis that the crystallinity of TO and ATO almost remains unchanged upon Si ion beam irradiation. However, morphological studies by atomic force microscopy and scanning electron microscopy show surface modification upon

irradiation. Interestingly, transport measurements show that the pristine ATO film possesses high conductivity which further increases upon irradiation for a fluence of 1×10^{12} ions/cm^2, followed with drastic decrease in conductivity and carrier concentration at higher fluences of irradiation. Band gap modification in TO and ATO films are also reported with irradiation fluence and found be in agreement with quantum confinement (QC) model for TO; while with Burstein-Moss shift (BMS) model for ATO films. However, the modifications at higher fluence can be ascribed to the band tail states due to very high disorder in the lattice as revealed by very high value of Urbach energy in corroboration with transmittance investigations, which also exhibits a significant decrease in transmittance in both films at irradiation fluence $\geq1\times10^{13}$ ions/cm^2. [for details, see *Thin Solid Films 616 (2016) 34*].

5.2.16 Swift Heavy Ion Irradiation Studies on $YMnO_3$ Based Thin Film Devices

Keval Gadani, P.S. Solanki and N.A. Shah

Department of Physics, Saurashtra University, Rajkot – 360 005, Gujarat, India

Divalent (Sr^{2+} and Ca^{2+}) doped $YMnO_3$ manganite based thin film devices (~100 nm thickness) were deposited onto single crystalline, n-type semiconducting *(100)* $SrNb_{0.002}Ti_{0.998}O_3$ (SNTO) substrates using PLD technique at UGC–DAE CSR, Indore. These films were irradiated by swift heavy ion (SHI) irradiation using 200 MeV Ag^{+15} and 100 MeV O^{+7} ions using facility at IUAC, New Delhi. Structural behaviour was studied using XRD measurements at room temperature. To study the surface morphology of the pristine and irradiated films, Atomic force microscopy (AFM) measurement was performed at IUAC, New Delhi. Current–Voltage hysteresis was performed to understand resistive switching behaviour of presently studied devices.

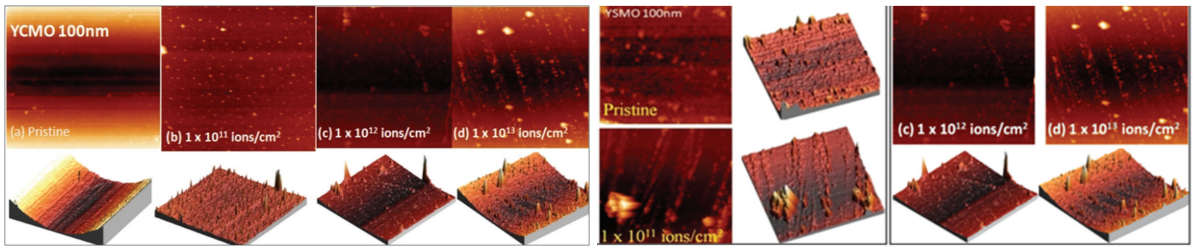

Figure 1. The AFM (two-dimensional and three-dimensional) micrographs of pristine and irradiated (100 MeV O^{+7} ion) $Y_{0.95}Ca_{0.05}MnO_3$ (YCMO) and (200 MeV Ag^{+15} ion) $Y_{0.95}Sr_{0.05}MnO_3$ (YSMO) films

It can be seen from Figure 1 that the pristine films possess nanostructured, homogeneous rectangular shaped granular islands which gets modified into hillock like defects onto the surface of thin films after irradiation with 1×10^{11}, 1×10^{12} and 1×10^{13} ions/cm^2 fluences. Values of rms surface roughness (RSR) increases with ion fluence which can be attributed to the energy deposition due to irradiation. Due to irradiation, surface morphology gets modified because of electronic energy transfer and the deposition of large kinetic energy by irradiated ions instantaneously on the films' surface.

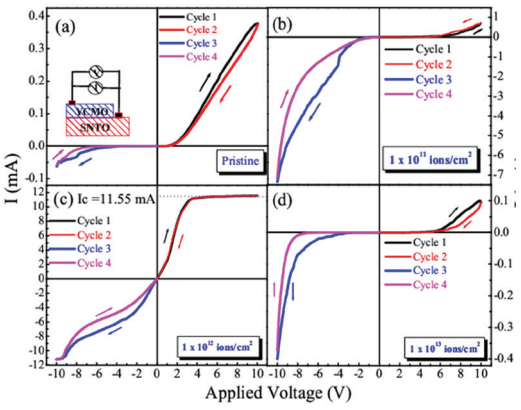

Figure 2: I –V curves of YCMO / SNTO films of pristine (a) and irradiated films (b) 1×10^{11} (1E11), (c) 1×10^{12} (1E12) and (d) 1×10^{13} (1E13) ions/cm2 at room temperature

YCMO films were irradiated using 100 MeV O^{+7} swift heavy ions (SHI) to different fluences using 15UD Tandem Accelerator, IUAC, New Delhi facility. I–V curves show the p-n junction/diode type asymmetric behaviour along with two resistive states under the positive and negative bias modes (Figure 2). This type of behaviour suggests the bipolar resistive switching (BRS) effect. The main aim is to understand the effect of SHI irradiation induced modification of interface across YCMO/SNTO p-n junction. In the present case, RS effect can be understood by (1) Role of oxygen vacancies (2) Field induced modification of depletion region (3) Charge carrier injection–trapped/detrapped process across YCMO/SNTO interface. Various theoretical models are reported for explanation of RS phenomenon in manganite based thin films. To understand the charge transport mechanism, various theoretical models were fitted with data of pristine and all the irradiated films. These kinds of high resistive conducting films will be useful in memory store and spintronic based device in future.SHI distinctly affects the I–V behaviour with an active role of defects, strain modifications and local annealing or recrystallization effect across YCMO/SNTO interfaces.

Structural investigations using θ–2θ X–ray diffraction (XRD) reveal that all the films crystallize in single phasic nature. Structural strain is found to increase due to irradiation with fluence of 1×10^{11} ions/cm^2. This can be ascribed to the irradiation induced creation of defects at the interface. Further increase in ion fluence of ~ 1×10^{12} ions/cm^2 can create more defects resulting in the degradation of lattice structure and hence strain gets enhanced in the film. For the higher ion fluence of ~ 1×10^{13} ions/cm^2, local heating takes place at the interface region as well as in the film lattice. This in turn results in the improved structure strain due to local annealing and recrystallization process. To study the surface morphology of the pristine and irradiated films, atomic force microscopy (AFM) measurement was performed. To understand the electrical properties of presently studied YSMO/ SNTO pristine and irradiated films, frequency dependent dielectric behaviour was studied. From Figure 3, it is seen that dielectric constant increases upon irradiation using the fluence of 1×10^{11} ions/cm^2 and 1×10^{12} ions/cm^2 while gets suppressed for 1×10^{13} ions/cm^2 fluence. Variation in dielectric behaviour with different ion fluence has been discussed on the basic of lattice strain and universal dielectric response (UDR) model.

5.2.17 Luminescence studies of rare-earth doped AGd_2O_4 (A=Sr and Ba) phosphors irradiated with γ-rays, O^{6+} and Au^{8+} ions

Jyoti Singh[1], J. Manam[1] and Fouran Singh[2]

[1]Department of Applied Physics, Indian Institute of Technology (Indian School of Mines), Dhanbad-826004, India
[2]Inter-University Accelerator Centre, Aruna Asaf Ali Marg, New Delhi - 110 067, India

The luminescence studies have been done for rare earth doped $SrGd_2O_4$ and $BaGd_2O_4$ phosphors. The swift heavy ion irradiation (O^{6+} and Au^{8+} ions) and gamma irradiation facility have been done at IUAC, New Delhi. After that, the thermoluminescence studies have been performed as a function of concentration, heating rates and doses, respectively. Raman and FESEM studies are also performed for swift heavy ion irradiated samples at IUAC, New Delhi. The thermoluminescence (TL) glow curves and dose responses of γ-irradiated samples are given in Figure. 1. The TL glow curves were further deconvoluted by CGCD method using Spreadsheet package software and the kinetic parameters such as order of kinetics (b), activation energy (E) and frequency factor (S) were also calculated. The order of kinetics for $SrGd_2O_4$: Eu^{3+} and $SrGd_2O_4$: Dy^{3+} is found to be first order and general orders, respectively. The linear behavior of dose response for as-formed $SrGd_2O_4$: Dy^{3+} and Eu^{3+} samples are observed within a wide range of dose. The TL glow curves of as-prepared $SrGd_2O_4$: Dy^{3+} phosphors was well-resolved into five peaks 114ºC, 161ºC, 198ºC, 248ºC, and 293ºC and the TL glow curve of γ-irradiated $SrGd_2O_4$: Eu^{3+} shows two well-resolved peaks at 120ºC and 325ºC with a shoulder at 264ºC by using computerized glow curve deconvolution program.

(a) (b)

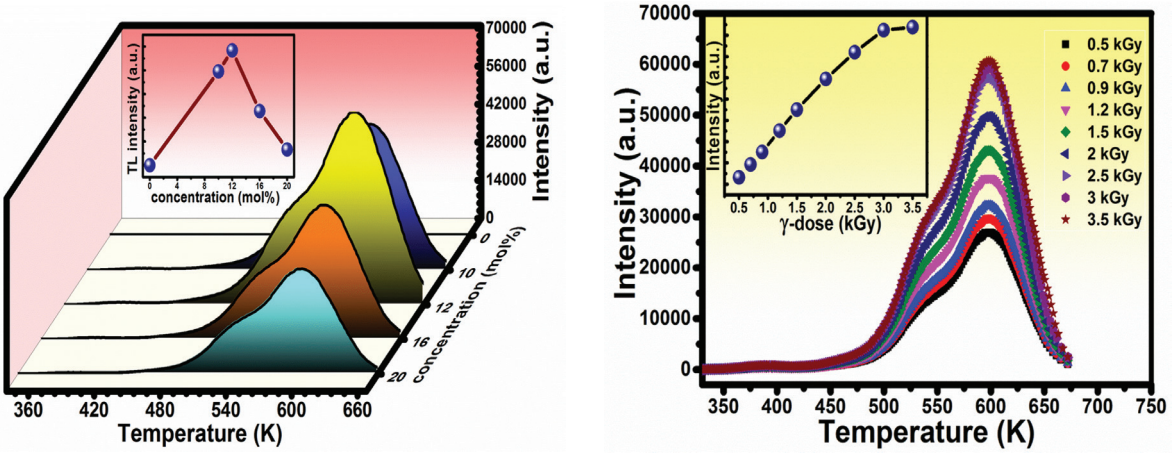

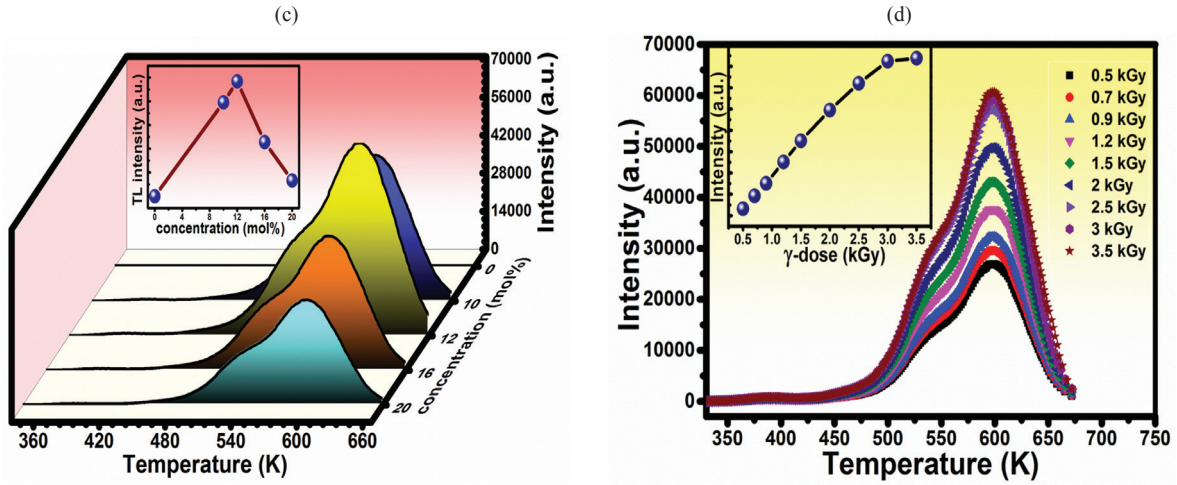

Figure. 1: the thermoluminescence glow curve and γ-ray dose response for $SrGd_2O_4$: Eu^{3+} (a) and (b) and for $SrGd_2O_4$: Dy^{3+} (c) and (d), respectively.

REFERENCES

[1] Jyoti Singh, J. Manam, Fouran Singh, Materials Research Bulletin 93 (2017) 318–324
[2] Jyoti Singh, J. Manam, Fouran Singh, Materials Research Bulletin 94 (2017) 113–121

5.2.18 Radiation damage and H/D trapping in ion irradiated Tungsten

Raole P M [1 *], Deshpande SP [1], Maya PN [1], Sharma Prashant [1], Attri Asha [1], Tyagi Anil [1], Khirwadkar S [1], Vala Sudhir [1], Abhangi M [1], Rayjada P [1], Satyaprasad A [1], Chandwani N[1], Kikani P[1], Kulriya P [2], K Devrani Devi[2], Safvan CP [2], Mal Kedar[2], Mukherjee Saurabh [3], Pujari PK [3], Karki V [4], Singh Manish [4], Kannan S [4], Mishra S [5], Khan KB [5], Lakhani A [6]

[1] Institute for Plasma Research, Gandhinagar, INDIA
[2] Inter-University Accelerator Centre, Aruna Asaf Ali Marg, New Delhi - 110 067, India
[3] Radio Chemistry Division, BARC, Mumbai
[4] Fuel Chemistry Division, BARC, Mumbai
[5] Radio Metallurgy Division, BARC, Mumbai
[6] UGC DAE Consortium, Indore

With the aim to study the radiation damage and H/D trapping in tungsten, 100 μm-thick tungsten foils (99.96 % pure, procured from Princeton Scientific Corp. USA) were recrystallized at 1838 K under 10^{-3} mbar pressure in Ar+H_2 environment and used for ion irradiation experiments carried out in Pelletron at IUAC Delhi. Au (Gold) ion beam of 80 MeV energy was used to create damage of 0.2 dpa in pure tungsten foils and alloys. The ion beam current was varied between 7 nA to 21 nA which correspondsto 1 to 3 pnA, for a fluence of1.3×10^{14}cm^{-2}. Some of Au irradiated samples were further exposed to 0.25 MeV helium ion beam with 1 μA current in LEIBF. The ion energy was so chosen that the range of helium ions matches with 0.1 MeV deuterium ions to be implanted at IPR and the fluence was so chosen that the damage created due to helium atom is sufficiently small (~0.03 dpa) compared to the pre-damage created by the gold ions (0.2 dpa).

Ion-irradiation experiments were followed by characterization of recrystallized (unirradiated) and pre-irradiated samples using different techniques. XRD analysis of recrystallized foils showed that after recrystallization the average crystallite size was more than 700 nm and SEM analysis showed that the average grain size is about 35 μm. The residual-resistivity-ratio (RRR – the ratio of resistivity at 300 K to 30 K) of the samples increased from 11 to 163 after recrystallization, indicating the annealing of the defects. Positron life-time measurements show a bulk life-time of 107 ps with 70 % intensity indicating a nearly defect free-samples with a few vacancy-clusters (corresponding life-time of 237 ps). TEM has also shown that the average grain-size has increased with nearly defect-free grains. The average dislocation line density was found to be 3.6×10^{8} cm^{-2} in the surface region.

The recrystallized foils were bombarded with 80 MeV Au^{7+} ions for a fluence of 1.3×10^{14} cm^{-2}. The implantation profile of the gold was measured using SIMS (Fig.1) and found to have a mean range of 4.06 ± 0.5 μm which is in agreement with the projected range from SRIM simulations (4.49 ± 0.73 μm). The positron Doppler broadening (DB) measurements showed a saturation of S-parameter (showing annihilation from valance electrons from the lattice) within the positron-beam penetration range of 500 nm (Fig.2). The positron life-time measurements indicated three lifetimes, one corresponds to the tungsten bulk life-time (t1 = 107 ps) with an intensity of 18

% (reduced from 70 % of un-irradiated sample), second measurement of 154 ps and the third of 260 ps with 41% and 37% intensity respectively, which might correspond to dislocations as well as vacancy clusters. TEM micrographs show long dislocations with length varied between 0.4 μm to 3 μm (Fig. 3). The dislocation line density was found to be 2.9×10^{8} cm^{-2} in the near-surface region. TEM micrographs taken at 2 μm depth from the top-surface (near the peak of damage zone) has also shown long dislocation lines with similar lengths as found near the surface region (Fig. 4). No dislocation-loops were observed either in the surface region or in the bulk. The dislocation density at the bulk was about 6.1×10^{8} cm^{-2}.

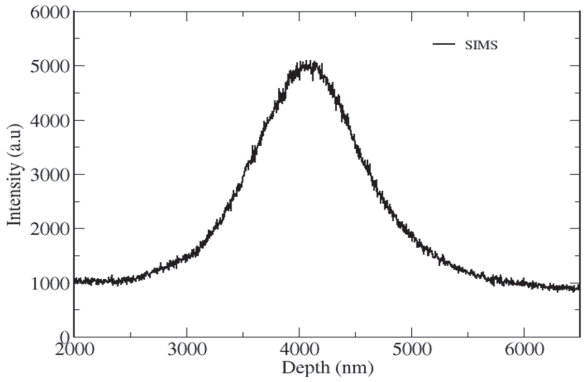

Fig. 1 Au depth profile from SIMS

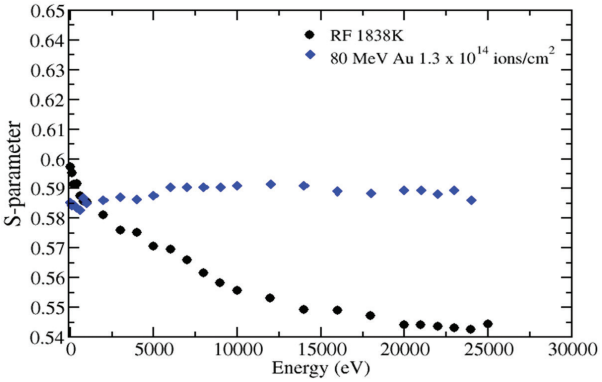

Fig. 2 Positron beam data showing defect saturation

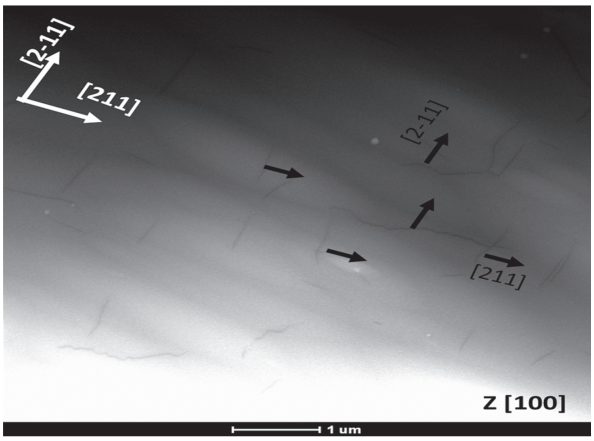

Fig 3. TEM micrographs showing dislocations for Au irradiated tungsten in near-surface region

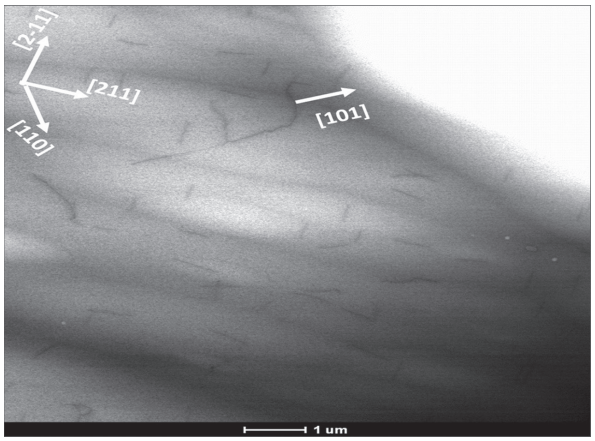

Fig 4. TEM micrographs showing dislocations for Au irradiated tungsten 2 μm deep into the sample

Low-energy, low-mass implantation experiments were carried out using 100 keV deuterium (at IPR) as well as 250 keV helium ions (at IUAC). The defect depth profile of D measured using positron DB studies indicated a broad peak between 100 nm – 300 nm deep into the foil. The deuterium depth profile analysed using SIMS also showed that the D concentration was closer to the surface than predicted by SRIM (427 ± 139 nm), a deuterium-peak was observed around 230 nm. TEM images of Tungsten implanted with 100 keV deuterium showed dislocation lines, network of dislocations and loops with dislocation line length ranging from 120 nm to 1900 nm and loop diameter within a range of 50 to 100 nm (Fig.5). The dislocation line density was 9.7×10^{8} cm^{-2}, higher than what is observed in boron and gold irradiated samples.

Deuterium bombardment was carried out on Au irradiated sample and the deuterium depth profile was measured using SIMS. It has been observed that the deuterium penetration was found to be deeper into the sample in the case of “Au+D”. On samples that were bombarded with 250 keV He ions, small dislocations are found with line-length varying between 40 nm – 1000 nm. No dislocation-loops were observed and the average dislocation was about $1\times10^{9}cm^{-2}$ which is the highest observed among any of the irradiated samples. Helium ions were also bombarded on samples that are pre-irradiated with gold. Further deuterium bombardment was carried out on those samples and the preliminary SIMS analysis shows that the helium bombardment reduces the deuterium content in “Au+He+D” samples (Fig.6) in narrow zone of about 75 to 225 nm from the surface.

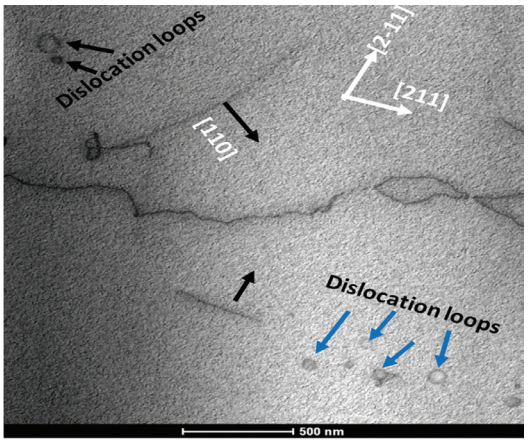

Fig. 5 TEM image of tungsten implanted 100 keV deuterium

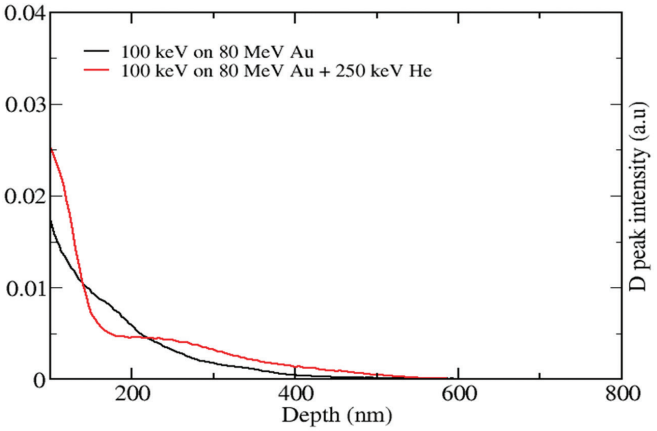

Fig. 6 Deuterium depth profile using SIMS in Au & Au+He implanted samples

5.2.19 Mixing study of Ni-Bi thin films using low energy ion beams

V. Siva[1], A. Chettah[2], S. Ojha[3], A. Tripathi[3], D. Kanjilal[3] and Pratap K. Sahoo[1]

[1]School of Physical Sciences, National Institute of Science Education and Research, HBNI, Jatni 752050, India
[2]Laboratoire LGMM, Groupe des materiauxfonctionnels, Université 20 Août 1955, Skikda, Algeria
[3]Inter-University Accelerator Centre, Aruna Asaf Ali Marg, New Delhi - 110 067, India

We have investigated the effect of ion beam mixing of Ni/Bi multilayers using 200 keV Ar ions and 100 MeV Au ions as a function of ion fluences. In the case of 200 keVAr ion irradiation, the Ni and Bi atoms diffuses across the interfaces upon increasing ion fluence (Fig. 1(a)). An enhancement in the mixing of Ni and Bi layers is observed with increasing ion fluence (Fig. 1(b)). The mixing can be attributed to the ion induced ballistic effects and the formation of latent tracks along the ion paths. In the case of 100 MeV Au ions, there is an enhancement in the mixing of Ni and Bi layers with increasing ion fluences as shown Fig. 1(c). These features were also reflected in the Rutherford Backscattering spectrometry spectra (using RBS facility of IUAC), in terms of the enhanced mixing with increasing ion fluences. The enhancement of the mixing in this case was attributed to the interface mediated phenomenon through the stable phases existing at the interfaces and ion induced temperature evolution. These results were published in references (1) and (2).

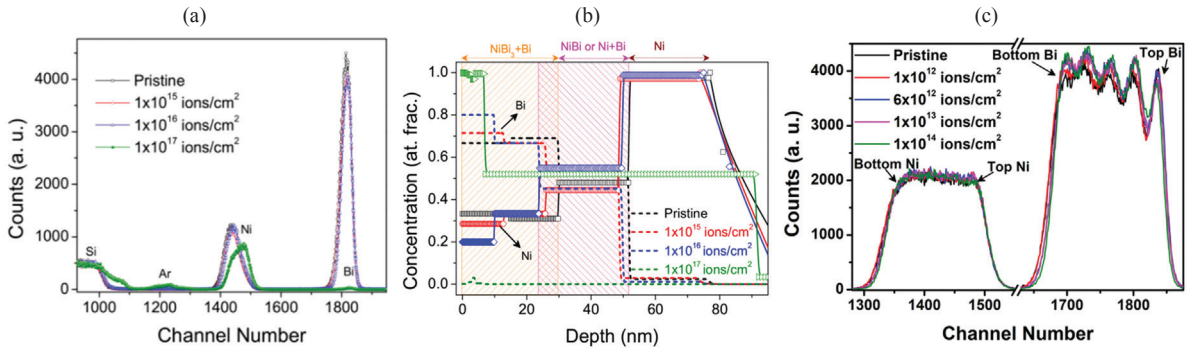

Fig. 1 (a) RBS spectra for the pristine and 200 keV Ar implanted samples in a fluence range of 1×10^{15} to 1×10^{17} ions/cm^2. (b) Depth profiles of Ni (solid lines with symbols) and Bi (dashed lines) for all these samples (c) RBS spectra of the pristine and 100 MeV Au irradiated samples to different fluences from 1×10^{12} to 1×10^{14} ions/cm^2.

REFERENCES

[1] V. Siva, D. P. Datta, S. Chatterjee, S. Varma, D. Kanjilal, P. K. Sahoo, Appl. Surf. Sci. 410 (2017) 519
[2] V. Siva et al., Nucl. Instrum. Methods Phys. Res. Sect. B 409 (2017) 314

5.2.20 Nanopattering of Si (100) using ion beam

Tanuj Kumar[1], Vandana[1], Indra Sulania[1], Sunil Ojha[1], and D.Kanjilal[2]

[1]Department of Nanosciences & Materials, Central University of Jammu, Jammu, India
[2]Inter-University Accelerator Centre, Aruna Asaf Ali Marg, New Delhi - 110 067, India

The self-organized nano-structures growth using ion beam has turned into a highly active research area of surface science. The surface nanopatterns have many technological applications in the field of optoelectronic, electronic, and magnetic devices in variety of fields [1]. Although, the several methods are used to grow nanopatterns like photolithography, sub-lithography, scanning probe tip, ion beam sputtering etc. Among these, ion beam sputtering has been a more versatile, very elegant and one-step approach. The control over ion beam parameters may be used to have surface topography into well-ordered nanostructures like one-dimensional ripples, regular arrays of dots and pits etc.

In this work ripple patterns were created on the Si(100) surface using 100 keV Ar^+ ion beam irradiation for the fluences ranging from 1×10^{17} ions/cm^2 to 1×10^{18} ions/cm^2. Atomic force microscopic (AFM) technique is used to see ripple patterns growth (Fig. 1). It is found that the orientation of ripples is perpendicular to the surface projection of ion beam. The amplitude of ripples and wavelength of ripples are found to be fluence dependent and according to the linear continuum/hydrodynamic models of surface patterning [2, 3]. Contact angle measurement demonstrates the possibility of engineering the hydrophilicity of ripple patterned Si (100) surface. Further, the RBS channeling has been used to estimate the defects formation in near surface.

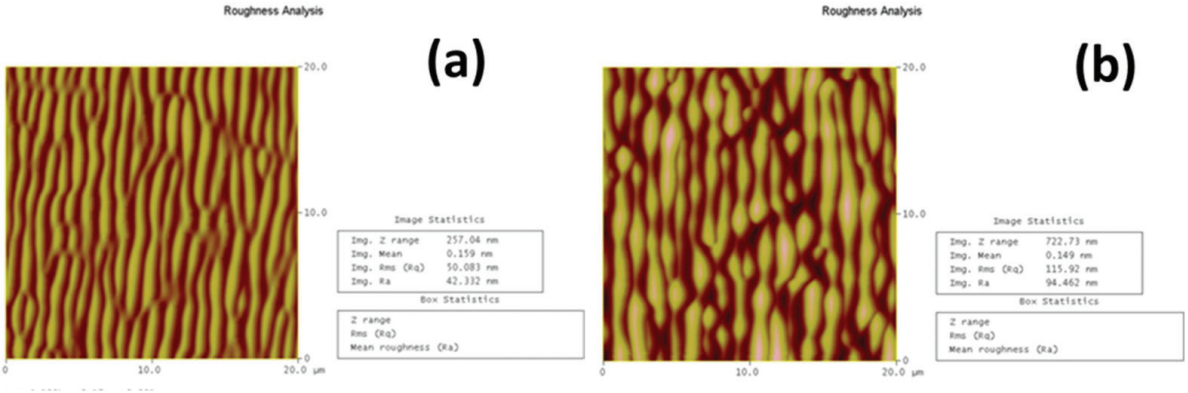

Fig. 1 Ripple formation at two different fluences (a) 9×10^{17} ions/cm^2 and (b) 3×10^{18} ions/cm^2

REFERENCES

[1] Y.C. Tseng, A.U. Mane, J.W. Elam, S.B. Darling, Advanced Materials 24 (2012) 2608
[2] R.M. Bradley, J.M. Harper, J. of Vacuum Sci. & Tech. A: Vacuum, Surfaces, and Films 6 (1988) 2390
[3] M. Castro, R. Cuerno, Appl. Surf. Sci. 258 (2012) 4171

5.2.21 Amorphization studies of crystalline-Si with energetic Si ions

Gurupada Maity[1], Shiv P. Patel[1*], Sunil Ojha[2], S. Chopra[2] and D. Kanjilal[2]

[1]Department of Pure & Applied Physics, Guru Ghasidas Vishwavidyalaya (A Central University) Bilaspur-495 009
[2]Inter-University Accelerator Centre, Aruna Asaf Ali Marg, New Delhi - 110 067, India

The ion induced amorphization of crystalline-Si (*c*-Si) has attracted significant interest since the beginning of the use of ion beam technology for the fabrication of high quality Si devices. A number of theoretical calculations and experiments have been designed to provide a better understanding of the mechanisms behind the crystal-to-amorphous transition in Si. In Si, amorphization occurs under ion irradiation when the free energy of the damaged crystalline phase is higher than that of the amorphous phase [1]. Our recent interest to fabricate amorphized-Si (*a*-Si) by ion irradiation is for the recrystallization of *a*-Si in contact with metal for obtaining high quality polycrystalline Si which are very important for solar cells [2].

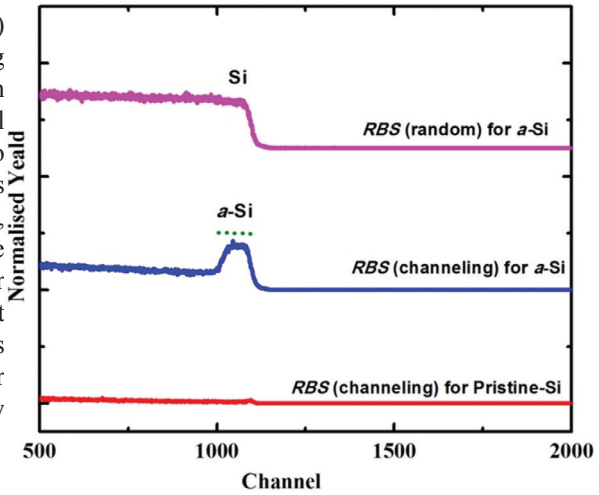

Figure 1: RBS (random and channeling) spectra of pristine- and a-Si using 100 keV Si ions to a fixed fluence of 2.0×10^{15} ions-cm^{-2}.

In this work, low energy ion beam facilities (LEIBF) at IUAC was used to implant Si ions with different energy of 35 keV, 50 keV, 75 keV, and 100 keV at a fixed fluence of 2×10^{15} ions-cm^{-2} for the amorphization of *c*-Si. RBS-channeling experiment was performed at IUAC, New Delhi by taking 1.8 MeV He ions, to confirm the amorphization of *c*-Si.

Figure 1 show the RBS spectra of pristine- and irradiated-Si substrates with 100 keV Si ions to fluence of 2×10^{15} ions-cm^{-2}. The RBS spectra clearly depicts that the c-Si substrates irradiatedwith Si ions get amorphized with a controlled amorphous thickness of 130 nm. The thicknesses of the a-Si have been controlled by choosing appropriate energy of the ions. For further characterizations, the Raman measurement was performed with 514 nm excitation which also confirms the amorphization of *c*-Si. Figure 2 shows the Raman spectra of pristine- and *a*-Si irradiated with Si ions of different energy. The Raman intensity corresponding to the Si is found to be reduced drastically in comparison to the pristine at 35 keV Si ion irradiations. Moreover, the Raman peaks completely disappears for the case of 50 keV, 75 keV, and 100 keV Si ion irradiations. Since the thickness of a-Si with 35 keV Si ions is about 50 nm and the penetration depth of visible light may be more than the thickness, Raman spectra for 35 keV Si ions show a small peak corresponding to the c-Si.

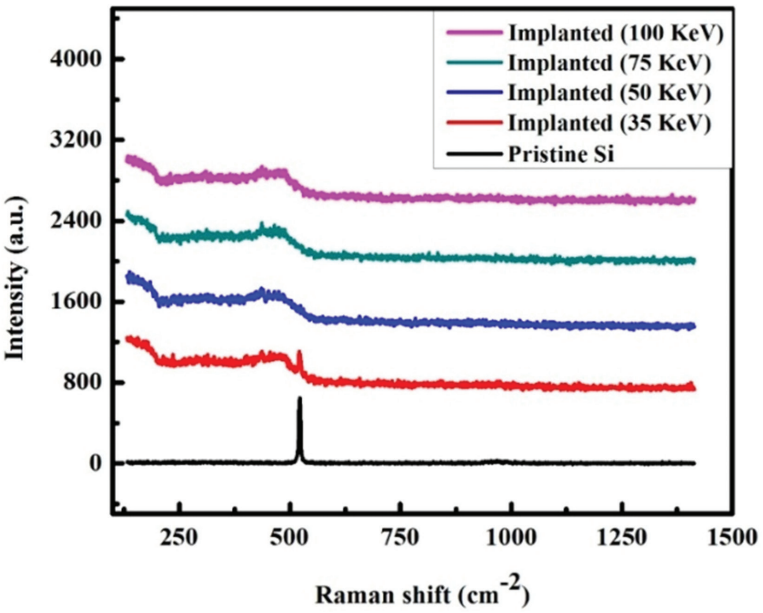

Figure 2: Raman spectra of pristine- and a-silicon substrate. The amorphization has been induced using Si ion with different energy at fixed fluence of 2.0×10^{15} ions-cm^{-2}.

REFERENCES

[1] Lourdes Pelaz, Luis A. Marqués, Juan Barbolla, J. Appl. Phys. 96 (2004) 5947

[2] D.V. Gestel, I. Gordon, J. Poortmans, Solar Ener. Mater. & Solar Cell 119 (2013) 261

5.2.22 Study the effect of silicon negative ion implantation in gallium arsenide

S. K. Dubey[1], Ajay Yaday[1], R. L. Dubey[1], S.Vishwakarma[1], Indra Sulania[2] and D. Kanjilal[2]

[1]Department of Physics, University of Mumbai, Mumbai- 400 098, India
[2]Inter-University Accelerator Centre, Aruna Asaf Ali Marg, New Delhi - 110 067, India

The negative-ion implantation technique remarkably ameliorates various problems such as charging problem, since the incoming negative charge of implanted negative ions is easily balanced by the outgoing negative charge as a part of secondary electron [1]. Silicon ion implantation in gallium arsenide is used to modify the structural, optical and electrical properties. It finds various applications in optoelectronic devices such as light emitting diode, laser diodes etc.

In the present work, semi-insulating undoped GaAs wafers were implanted with 100 keV silicon negative ions (Si^{-1}) with various fluences varying between 1×10^{15} and 2×10^{17} ions cm^{-2} at room temperature using MC-SNICS ion source at Low energy ion beam accelerator facility in IUAC, New Delhi. Implanted samples were characterized using AFM, XRD, Raman spectroscopy and UV-Vis.-NIR Spectroscopy.

The 3-Dimensional AFM image of non-implanted GaAs sample showed a smooth micrograph with root mean square surface roughness of 0.987 nm, whereas for all the implanted samples, the r.m.s surface roughness was found to increase with ion fluence. Fig.1 shows the representative 3D AFM image (2µm×2µm) of GaAs sample surface implanted with silicon negative ion at 100 keV with fluence of 5×10^{16} ions cm^{-2}.

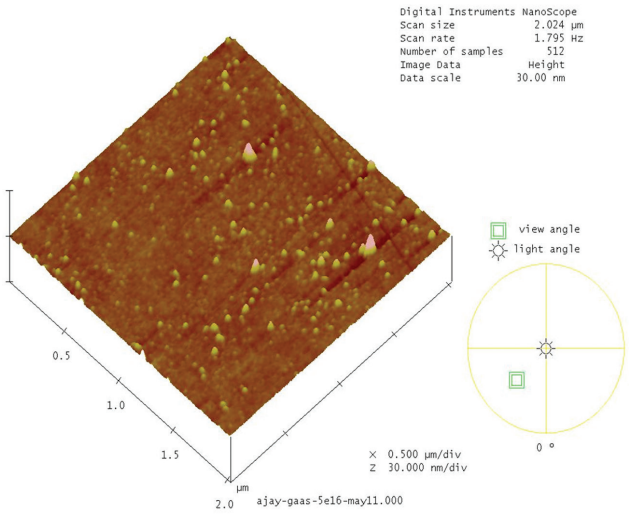

Figure 1. 3 D AFM image (2µm×2µm) for GaAs implanted with 5 ×10^{16} ions cm^{-2}

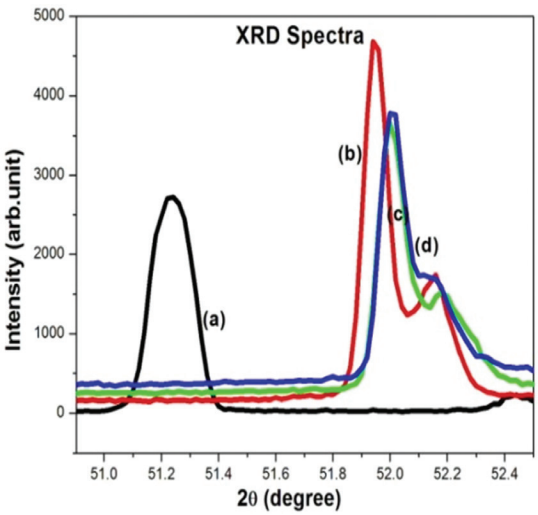

Figure 2. X-ray diffraction patterns of GaAs (a) non-implanted and implanted with silicon negative ion with fluencies of (b) 5×10^{16} (c) 1×10^{17} (d) 2×10^{17} ions cm^{-2}

Figure 2 shows the X-ray diffraction spectra for non-implanted and silicon ion implanted GaAs samples. The shift of the X-ray diffraction peak towards higher angle side for the implanted GaAs samples indicates the change in the lattice parameter. The size of crystallites estimated from the FWHM was found to vary between 136.0 nm and 56.0 nm for ion fluence 5×10^{16} to 2×10^{17} ions cm^{-2} respectively. UV-Vis-NIR transmission spectra of GaAs samples implanted with Si^{-1} ions showed the increase in absorption with respect to ion fluence. Raman spectroscopy measurements and I-V measurements have also been carried out and the analysis of the same is under process.

REFERENCES

[1] J. Ishikawa et al., Nucl. Instr. and Meth. B 96 (1995) 7-12

5.2.23 Metal-semiconductor composite nanodot evolution on insulator surface by ion beam dewetting

D. P. Datta[1], V. Siva[1], A. Singh[1], S. Varma[2], D. Kanjilal[3] and P. K. Sahoo[1]

[1]School of Physical Sciences, National Institute of Science Education and Research (NISER) Bhubaneswar, Jatni 752050, India
[2]Institute of Physics, Sachivalaya Marg, Bhubaneswar-751005, India
[3]Inter-University Accelerator Centre, Aruna Asaf Ali Marg, New Delhi - 110 067, India

Elemental metal or semiconductor as well as metal-semiconductor hybrid nanostructures exhibit unique physiochemical properties which make them promising for a wide range of applications including microelectronics and optoelectronics, sensors, catalysis, or photovoltaics. In this study, the self-organized evolution of a metal semiconductor bilayer, viz. Au and Si thin films, on SiO_2 under ion irradiation is shown. Ion energy deposition leads to development of Au rich silicide nanodot array on the insulator surface. The depositions of Si and Au thin films on SiO_2 were carried out using e-beam evaporation. The samples were irradiated by 500 keV Xe^{2+} ions at Low Energy Ion Beam Facility at IUAC, New Delhi. The evolution is shown in Figure 1. The process leads to an increasing

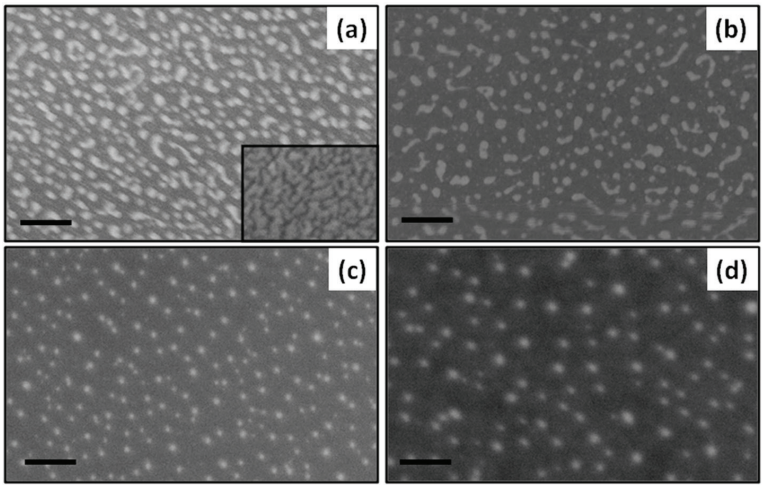

Figure 1: SEM images showing the morphological evolution of the Au-Si bi-layer after 500 keV Xe-ion irradiation to fluences of (a) 5×10^{14} (b) 1×10^{15} (c) 5×10^{15} and (d) 1×10^{16} ions cm^{-2}. The scale bar shown is 200 nm. The inset in (a) shows the morphology of as-deposited bilayer.

amount of silicide in the composite nanodot structures with increasing fluence. The morphological and compositional analyses reveal that a combined effect of dewetting, sputtering, and mixing results in evolution of nanodot array through different stages. Thus, our study indicates controllability over nanostructure shape, size and composition by ion beam processing. Further, it is found to be a general process for self-organized fabrication of such composite nanodots.

REFERENCES

[1] D. P Datta, V. Siva, S. Varma, D. Kanjilal, P. K. Sahoo, Phys. Chem. Chemical Phys. 18 (2016) 29955
[2] D. P. Datta, V. Siva, A. Singh, S. R. Joshi, D. Kanjilal, P. K. Sahoo, Nucl. Instr. &Meth. B 379 (2016) 48

5.2.24 Investigation of Electrical and Optical Properties of N and Li co-implanted ZnO samples

Apu Mondal[1], S. Pal[1], D. Jana[1], A. Sarkar[2], D. Kanjilal[3], P. Kumar[3], S.K. Ray[4] and A. Singha[5]

[1]Department of Physics, University of Calcutta, 92, Acharya Prafulla Chandra Road, Kolkata 700 009, India
[2]Department of Physics, Bangabasi Morning College, 19, R. C. Sarani, Kolkata 700 009, India
[3]Inter-University Accelerator Centre, Aruna Asaf Ali Marg, New Delhi - 110 067, India
[4]S. N. Bose National Centre for Basic Sciences, Salt Lake City, Kolkata 700 098, India.
[5]Department of Physics, Bose Institute, 93/1, Acharya Prafulla Chandra Road, Kolkata 700009, India.

Commercially available high purity ZnO polycrystalline powder (99.99% pure, Sigma-Aldrich, Germany) has been pelletized and thereafter annealed at 500ºC for four hours. Removal of unwanted organic samples or any H_2 or H_2O molecules was the main objective of pre-irradiation annealing [1]. After annealing, 50 keV N-ion and 50keV Li-ion have been implanted on those samples with fluence varying from 10^{15} to 10^{16}ions/cm^2 using Low Energy Ion Beam Facility (LEIBF) at Inter University Accelerating Centre (IUAC), New Delhi, India. After implantation, generally crystalline property of samples decrease but the XRD pattern reveals that (101) peak intensity gets increased after implantation compare to un-implanted one. The most intense (101) peak is observed in nitrogen implanted ZnO. The room temperature Raman spectroscopy (fig.1) shows that peaks around 100 cm^{-1} get broadened due to implantation whereas peak around 439 cm^{-1} gets diminished after implantation suggesting the generation of native defects like oxygen and zinc vacancies in the samples. A new peak appeared at 275 cm^{-1} in N implanted and Li-N co-implanted samples only. Hence, it is expected that the origin of this peak must be N related.

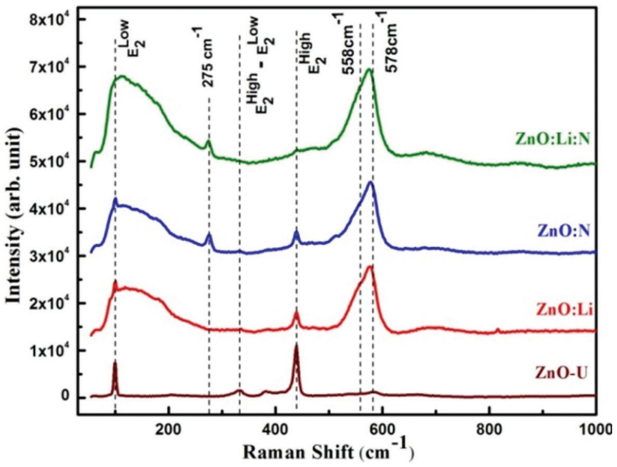

Fig.1: RT Raman spectra

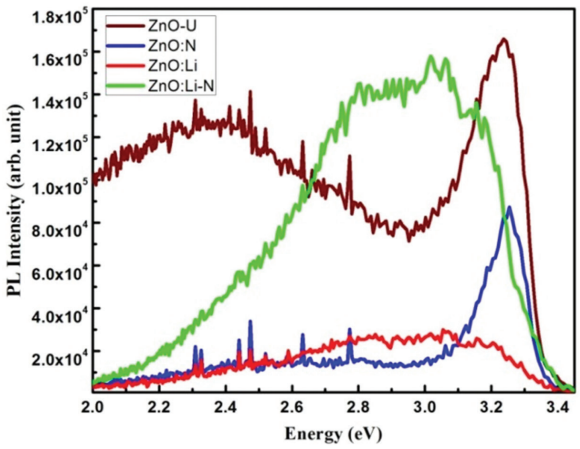

Fig. 2: RT PL spectra

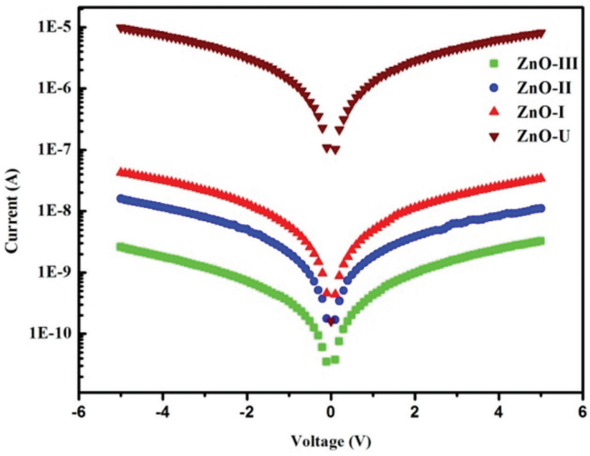

Fig. 3: I-V relationship

It has been reported that this 275 cm^{-1} peak appears due to I_{Zn}-N_O type of complex defect state in N doped ZnO. In all implanted samples, a broad intense peak 520-600 cm_{-1} has been observed which is a composition of two Gaussian peaks centred around 558 and 580 cm^{-1}. The first one is due to zinc interstitial (Zn_i) and the latter one is due to oxygen vacancies (VO) [2]. The PL intensity of the samples at room temperature heavily quenches after implantation with Li and N cases whereas in the case of co-doped samples a bright blue-violet luminescence has been observed (Figure 2). The origin of this might be related to zinc interstitial type of defects. A drastic increase in resistivity has been observed in implanted samples as shown in Fig. 3.

REFERENCES

[1] S. Pal, T. Rakshit, S.S. Singha, K. Asokan, S. Dutta, D. Jana, A. Sarkar, J. Alloy Comp. 703 (2017) 26
[2] Z. Wang, S. Su, F. C. C. Ling, W. Anwand, A. Wagner, J. Appl. Phys. 116 (2014) 033508

5.2.25 Fabrication of p–n junctions in ZnO nanorods by O^+ ion implantation

Avanendra Singh[1], K. Senapati[1], D. P. Datta[1], R. Singh[2], T. Som[2], S. Bhunia[3], D. Kanjilal[4], Pratap K. Sahoo[1]

[1]School of Physical Sciences, National Institute of Science Education and Research, HBNI, Jatni 752050, India
[2]Institute of Physics, Sachivalaya Marg, Bhubaneswar, Odisha 751005, India
[3]Saha Institute of Nuclear Physics, Bidhannagar, Kolkata 700064, India
[4]Inter-University Accelerator Centre, Aruna Asaf Ali Marg, New Delhi - 110 067, India

C-axis oriented Zinc Oxide nanorods (NRs) were reproducibly grown on 30 nm ZnO film coated Si substrates using wet chemical technique (Figure 1(a)). For fabricating p–n junctions in a single ZnO NRs, samples were irradiated by low energy O^+ ions using the low energy ion facility of IUAC New Delhi. The room temperature PL measurements of irradiated samples showed the recovery of near band edge (NBE) emission upon annealing; while an additional dominant deep level emission is also observed (Figure 1(b)). Deconvolution analysis shows that these peaks originate from Oxygen interstitials (O_i) and may contribute to p-type conductivity in ZnO NRs. Such oxygen rich implanted NRs, may be suitable for green emissions and p-type conductivity [2].

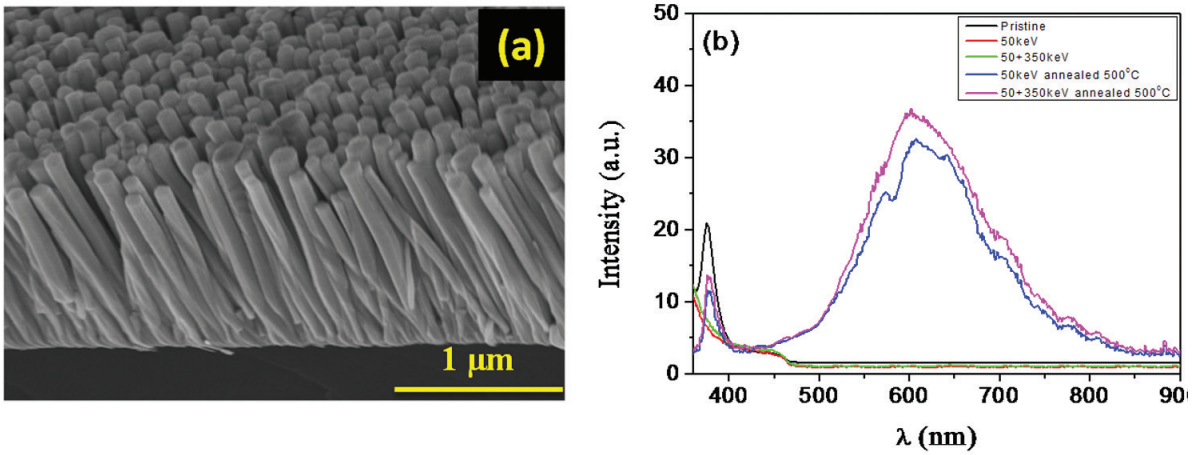

Figure 1: (a) FESEM image of ZnO nanorods, (b) PL spectra from NRs after annealing.

ZnO NRs were successively implanted with O^+ ions having energies of 50 and 350 keV. The nonradiative transition centres completely eliminate the NBE emission in implanted samples while annealing manifests the broad deep level emission along with NBE. Deconvolution analysis reveals dominating O_i followed by red emission. Since O_i forms acceptor levels, it can be concluded that O^+ ion implantation leads to formation of O rich p–n–p–n tandem in ZnO nanorods. The current maps of post-annealed samples show that side facets of NRs have more conductance than top facets. This can be attributed to trapping of more free charge carriers in top facets in defect states created by implantation. The recorded I–V characteristics measured by C-AFM indicate the formation of Schottky like junctions between C-AFM tip and NRs.

REFERENCES

[1] Avanendra Singh et al.,Nucl. Instr. and Meth. B 409 (2017) 143
[2] U. Ilyas et al., J. Appl. Phys. 110 (2011) 093522

5.2.26 500 keV argon ion implantation induced structural modifications in Glass RPC detector materials: A Positron Lifetime study

K.V. Aneesh Kumar[1], K. Asokan[2], H.B. Ravikumar[1]

[1]Department of Studies in Physics, University of Mysore, Manasagangotri, Mysuru-570006, India
[2]Inter-University Accelerator Centre, Aruna Asaf Ali Marg, New Delhi - 110 067, India

The studies on argon ion implantation induced effects with varying energies and fluences provide useful information on RPC detector fabrication for the India Based Neutrino Observatory (INO) [1] project. 500 keV Ar ion implantation induced structural modifications at diverse fluences in Asahi and Saint Gobain float glass RPC detector [1] materials were explored. The low energy ion beam (LEIB) facility available at IUAC, New Delhi is used to implant 500 keV argon ions to 1×10^{13} to 1×10^{16} ions cm^{-2}. The microstructural characterization of argon ion implanted glass samples were performed using one of the well-established technique viz., Positron Annihilation Lifetime Spectroscopy (PALS) [2]. Positron annihilation lifetime spectra of as received and 500 keVargon ion implanted Asahi and Saint Gobain float glass samples were acquired by fast-fast coincidence lifetime spectrometer with BaF_2 scintillators. Consistently reproducible PALS spectra were analyzed into three lifetime components with the help of a computer program PATFIT-88[3] with proper source and background corrections. The dc electrical conductivity of glass samples of dimension 1cm × 1cm × 0.28 cm was measured using Keithley 2636A system Source Meter. The detailed theory and measurements of positron lifetime and electrical conductivity can be found elsewhere [2, 4].

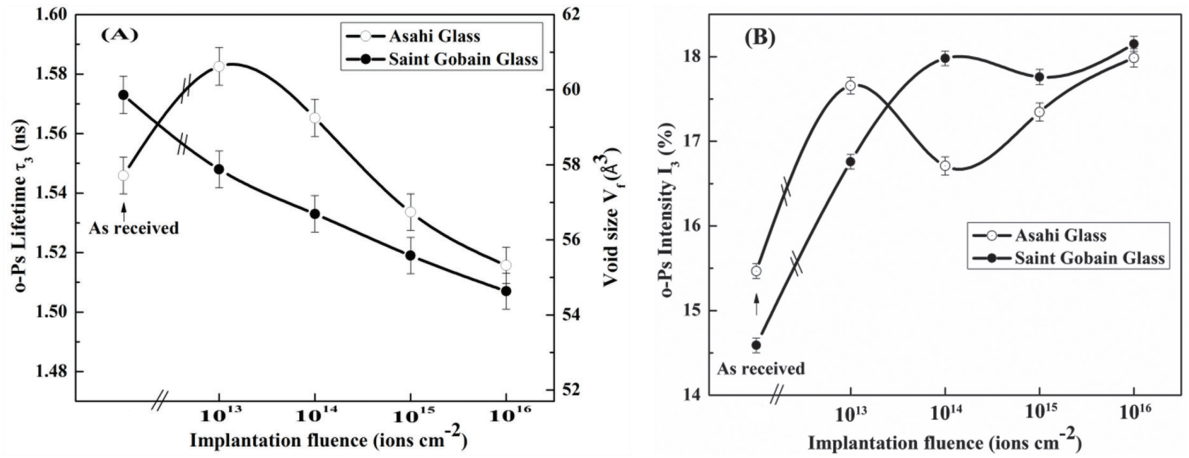

Figure 1. (A) The variation of o-Ps Lifetime (τ_3) and void size (V_f), (B) o-Ps Intensity (I_3) of argon ion implanted Asahi and Saint Gobain glass samples as a function of implantation fluences.

The variation of *o*-Ps lifetime (τ_3), void size (V_f) and o-Ps intensity (I_3) of 500 keV argonion implanted Asahi and Saint Gobain glass samples with different fluences are shown in Figure 1(A &,B). The increase of about 37 ps in *o*-Ps lifetime (τ_3) corresponding to 3.01 Å3 in void size (V_f) from 57.62 Å3 to 60.63 Å3 at the implantation fluence of 10^{13} ions cm^{-2} was observed upon argon ion implanted Asahi glass samples. Consequently, there is a marginal decrease of about 67 ps in *o*-Ps lifetime (τ_3) and 5.44 $Å^3$ void size (V_f) upon implantation of 10^{16} ions cm^{-2}. Due to the presence of more SiO_2 concentration in Saint Gobain glass sample compare to Asahi glass, the *o*-Ps lifetime (τ_3) of SG glass is 1.573 ns, which is 28 ps more than Asahi glass [5]. The argon ion implanted Saint Gobain glass samples exhibit 66 ps reduction in *o*-Ps lifetime (τ_3) and 5.31 $Å^3$ in void size (V_f) at the implantation fluence of 10^{16} ions cm^{-2}.

The slight increase in void size in Asahi glass sample at lower implantation fluences is attributed to the breakage of Si-O bonds and the formation of interior ion tracks in the glass network upon high energy ions. Therefore, the increased void (V_f) size in Asahi glass at lower fluences is attributed to the cleavage of Si-O bonds [6], the formation of free radicals and electrons. The decreased *o*-Ps lifetime (τ_3) and void size (V_f) upon higher implantation fluences is due to the increased local temperature induced diffusion followed by trapping of ions in the interior glass voids. The argon ion implanted Asahi glass samples exhibit about 2.51 % (15.47 %-17.98 %) and Saint Gobain glass samples shows 3.56 % (14.59 %-18.15 %) increase in *o*-Ps intensity (I3) at 10^{16} ions cm-2 fluences. The increased *o*-Ps intensity (I3) is probably due to oxygen enrichment of the trapping sites and annihilation of positrons at negative charged oxygen-related defects as evidenced by the decreased o-Ps lifetime (τ_3) [7].

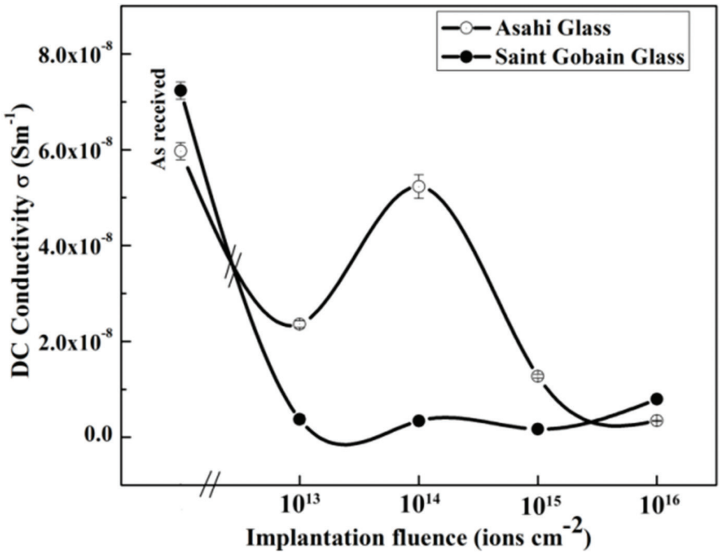

Figure 2. The variation of dc conductivity of as received and argon ion implanted Asahi and Saint Gobain glass samples as a function of ion implantation fluences.

The calculated dc conductivity of as-received Asahi and Saint Gobain glasses are 5.974×10^{-8} Sm^{-1} and 7.235×10^{-8} Sm^{-1} respectively. From Figure 2, it is observed that 500 keV argon ion implanted Asahi and Saint Gobain glass samples exhibit less conductivity at higher implantation fluences compared to as received samples. The reduced dc conductivity of both Asahi and Saint Gobain glass samples upon implantation of argon ions attributed to the increased bond energy of SiO_4 tetrahedral glass network. At higher implantation fluences, network close packing hinders the movement of chains in the glassy matrix and hence the electrical conductivity. The dc conductivity of argon ion implanted Saint Gobain glass samples are less compared to Asahi glasses indicate the extent of close packing in the glass network. This is also evident by the reduced void size from the PALS results. We expect that the appropriate energy and fluence of argon ion implantation enhances the strength and performance of glass RPC detectors.

REFERENCES

[1] A. Kumar et al., Pramana-J. Phys. 88 (2017) 1
[2] K.V. Aneesh Kumar et al., J. Appl. Polym. Sci.134 (2017) 4496
[3] P. Kirkegaard et al., Riso Nat. Lab. Reports, Denmark, RISO-M-274 (1989)
[4] K.V. Aneesh Kumar et al., IEEE Trans. Nucl. Sci. 62 (2015) 306
[5] R. Suzuki et al., Radiat. Phys. Chem. 68 (2003) 339
[6] M. Mohapatra et al., Nucl. Instrum. Methods B 269 (2011) 2057
[7] R.S. Brusa et al., Nucl. Instrum. Methods B 268 (2010) 3186

5.2.27 Superconducting $Ba(Fe,Co)_2As_2$ crystals and their surface damage by 1.5 MeV Ar-beam

K R Sahu[1], D Sanyal[2], Th. Wolf[3], F Singh[4], P K Kulriya[4], S A Khan[4], S Ojha[4], A Saha[5], D Kanjilal[4], Udayan De[6]

[1]Physics Dept., Egra S.S.B. College, Egra, PurbaMedinipur, W Bengal, India 721429
[2]Variable Energy Cyclotron Center, 1/AF Bidhannagar, Kolkata 700064, India
[3]Forschungszentrum Karlsruhe, Institut fur TechnischePhysik, Postfach 3640, D-76021 Karlsruhe, Germany
[4]Inter-University Accelerator Centre, Aruna Asaf Ali Marg, New Delhi - 110 067, India
[5]UGC-DAE CSR, Kolkata Centre, Sector III, LB-8, Bidhan Nagar, Kolkata 700 098, India
[6]Calcutta Inst. of Engineering & Management, 24/1A Chandi Ghosh Road, Kolkata; India 700040

High temperature (up to 56 K) superconductivity found in last few years in magnetic compounds like Fe pnictides, has shattered the textbook idea that magnetic impurities always destroy superconductivity. For example, $BeFe_2As_2$ becomes superconducting by Co-"doping" [1], and roughly represents all 4 groups of Fe-superconductors. Fairly high critical current density and possibility of easier fabrication into wires make these attractive for developing superconducting wires.

Ion irradiation damage investigation is desirable in these materials - partly for theoretical understanding and greatly because of the potential of using such superconducting magnets in radiation environments of fusion

devices and accelerators. Here, $Ba(Fe_{1-x}Co_x)_2As_2$ for x = 0.000 (non-superconducting), and x = 0.057 & 0.102 (superconducting [1]) samples have been produced in thin Single Crystal (SXL) form suitable for (a) bulk radiation damage study by 50 MeV Li-ions in a sister project, and (b) present surface damage by 1.5 MeV Ar-beam. We have characterized the crystal samples first in Ur (Un-radiated) condition. We next report 1.5 MeV Ar-irradiations and on-going damage investigations by XRD (Fig.1 etc), Micro-Raman Spectroscopy (Fig.2 etc), SEM EDAX, RBS (Fig.3 etc), UV-Vis Photoluminescence (Fig.4 etc). Superconducting transition temperature and positron annihilation parameters have also been measured.

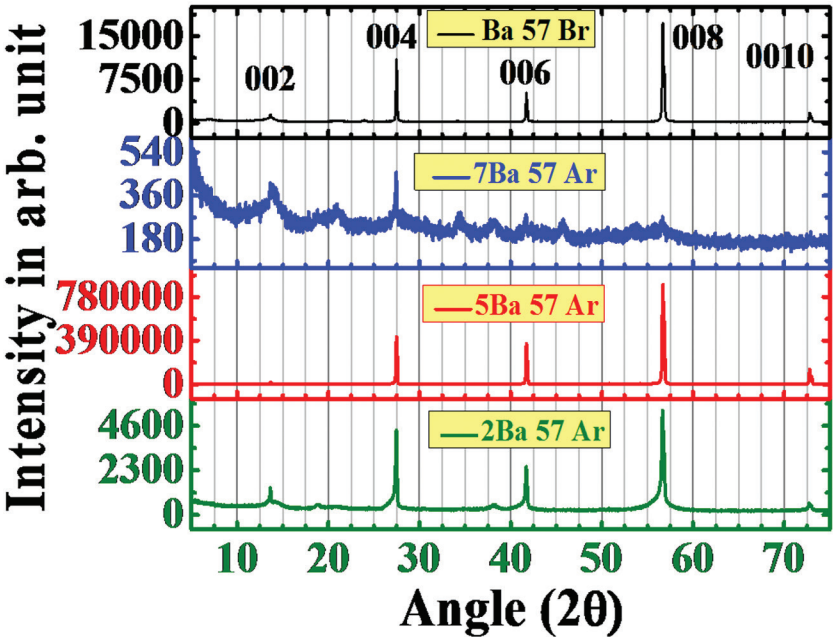

Fig.1: XRD (x-ray diffraction) pattern of plate-like Single Crystal $Ba(Fe_{1-x}Co_x)_2As_2$, x = 0.057 or 5.7% samples showing only 00l reflections – in Br (Before radiation) &Ar (After radiations, by 1.5 MeV Ar-beam). Sharp peaks in unirradiated Ba122 sample (called "Ba 57 Br") become progressively broader after irradiation fluences 0.2×10^{15} (sample "2Ba 57 Ar"), 2.5×10^{15} (sample "5Ba 57 Ar") and 10×10^{15} ions/cm^2. (sample "7Ba 57 Ar").

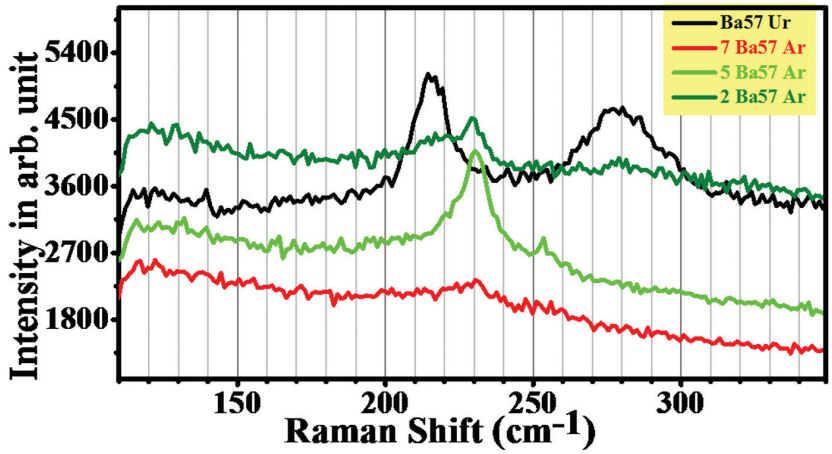

Fig.2: Raman spectroscopy of plate-like Single Crystal $Ba(Fe_{1-x}Cox)_2As_2$, x = 0.057 or 5.7% samples – in Ur (Un-radiated) &Ar (After radiations, by 1.5 MeV Ar-beam). Sample numbers 2, 5 & 7 indicate increasing irradiation doses as given Fig.1 caption.

XRD patterns other than Fig.1 here, show positional shifts of the XRD peaks to prove gradual decrease of the lattice parameter c due to increasing Co-substitution: c =13.0314 Å for x=0.000, c = 12.999 Å for x=0.057 & 12.988 Å for x=0.102. Raman shifts due to these low energy heavy ion irradiations (Fig.2) have been significant. EDX (Energy Dispersive X-ray) Analysis of elemental composition appear to give reasonable results: for example, the x = 0.057 sample irradiated by 2×10^{14} Ar-ions /cm^2 shows 12.55 at% Ba, 18.56 at% As, 20.11 at% Fe & 46.80 at% Oxygen. Ignoring the O-contamination, approximate Ba122 composition is, therefore, confirmed. From our preliminary Rutherford Backscattering (RBS) using 2 MeV He^+ions, Fig.3 shows data for a 10.2 at% Co-doped Ba122 un-irradiated crystal. Three steps corresponding to the three elements have been reproduced by a simulation. This and SEM EDX analysis are expected to detect irradiation-induced composition changes, if any. PLA or Photoluminescence Analysis (Fig.4) should reveal ion radiation damage to chemical bonding of the atoms of the $Ba(Fe,Co)_2As_2$ superconductors.

A more complete picture and understanding are expected from next irradiations and data interpretation.

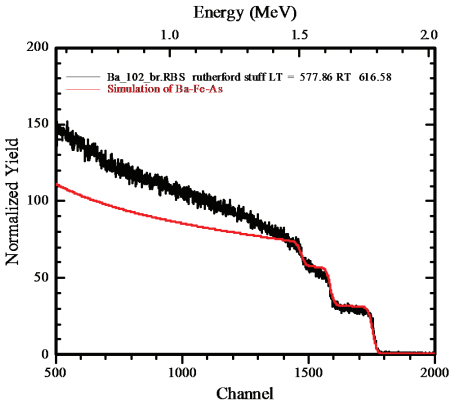

Fig.3: Backscattered ions yield vs. channel number denoting energy of the backscattered ion in RBS.

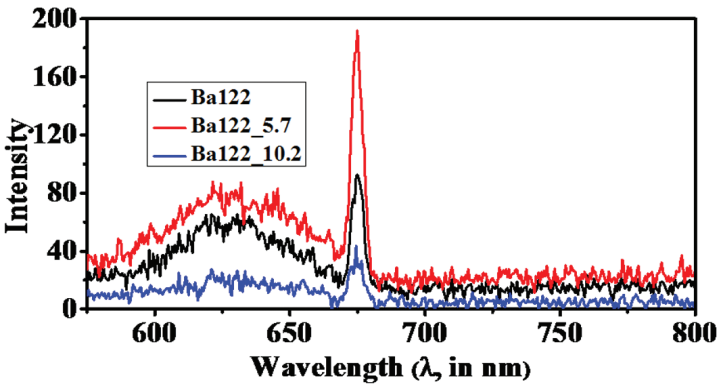

Fig. 4: PLA Emission peaks have been identified at (674.84 ∓ 0.05) nm for Ba122 sample, at (675.06 ∓ 0.06) nm for Ba122_5.7% Co-doped sample and at (674.57 ∓ 0.17) nm for Ba122_10.2% Co-doped sample.

REFERENCES

[1] D. Sanyal, T. Wolf, M. Chakrabarti, U. De, Solid St. Comm. 180 (2014) 35-38

5.2.28 Study of thermoluminescence property of C^+ ion doped anodized alumina

S. Bhowmick[1], D. Das[1], J. Asirvatham[1], S.A. Khan[2], D. Sen[2], R. Huebner[3], D. Kanjilal[2] and A. Kanjilal[1]

[1]Department of Physics, School of Natural Sciences, Shiv Nadar University, NH-91, Tehsil Dadri, Gautam Buddha Nagar, Uttar Pradesh 201314, India
[2]Inter-University Accelerator Centre, Aruna Asaf Ali Marg, New Delhi - 110 067, India
[3]Electron Microscopy Laboratory, Helmholtz-Zentrum Dresden-Rossendorf (HZDR), PO Box 51 01 19, 01314 Dresden, Germany

The application of thermoluminescence (TL) has created immense interest due to their potential to determine radiation doses for food-safety, radiation therapy, personal dosimetry, environmental monitoring, etc. However, the performance of a phosphor relies on thermally stimulated light emission from luminescent centres created during the exposure to an ionizing radiation. Aluminum oxide (Al_2O_3) is one of the promising materials for dosimetry. Although this material was forgotten for a long time due to its low sensibility compared with that of TLD-100, it recently regained interest owing to the development of anion defects in Al_2O_3:C single crystals. It was reported to be highly sensitive, even more than TLD-100, though conventional crystal growth technique requires high temperature in the presence of a high tumbling atmosphere. Nevertheless, the TL sensitivity of crystalline Al_2O_3 can be enhanced by doping with carbon, but this is only good for low dose radiation monitoring (typically 0.1-100 Gy). Interestingly, a prominent TL sensitivity can be achieved from nanocrystals with increasing surface-to-volume ratio because of increasing surface states. Therefore, judicial use of Al_2O_3 nanocrystallites will give a fertile ground for offline dose monitoring. The nanotrenches of anodized alumina in this respect can also give additional path for improving efficiency, which can be enhanced further by controlled introduction of C in Al_2O_3 matrix. Since ion beam implantation is known to be a powerful method because of its ability to control over distribution of dopants and residual defects, it is therefore important to understand the impact of C^+ ions in controlling the formation of traps in anodized alumina and also to explore its suitability for ion beam dosimetry by following the TL glow curves with increasing fluence (i.e. ions/cm^2).

To execute this plan, after optimizing the porosity, the penetration depth of C+ ions in Al_2O_3 layers have been calculated by SRIM. Typical porous structure in the present set of samples is shown in Figs. 1 and 2. Based on this understanding, the anodized alumina has been exposed to 50 keV C^+ ions in the fluence range of 2.33×10^{15} to 1.3×10^{16} ions/cm^2. Following the initial structural analysis by XRD, TL response of the ion irradiated samples was characterized, showing a systematic rise in intensity with increasing fluence (Figure 3). For understanding of the underlying process, the anodized alumina before and after irradiation have now been studied by various techniques, like SEM, TEM, XRD, RBS, and XPS.

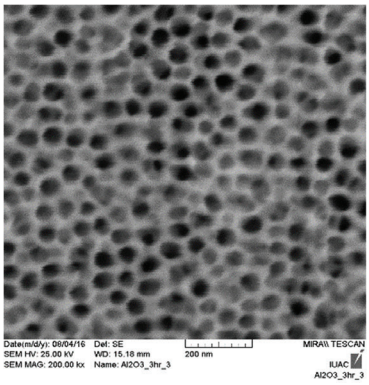

Fig. 1: Plan-view SEM image showing porous anodized alumina

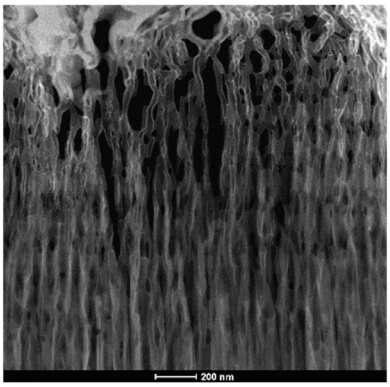

Fig. 2: Cross-sectional HAADF image showing trenches in anodized alumina

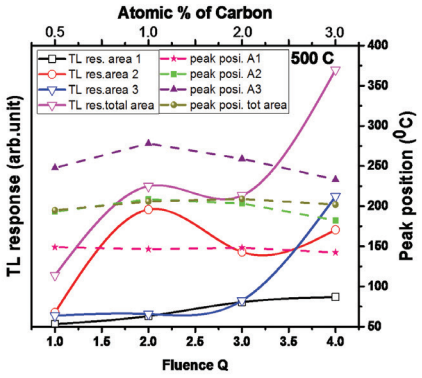

Fig. 3: TL response (superimposed with fitted data) after C+ implantation with various fluences (Q in ions/cm2).

5.2.29 Tailoring Optical Properties of ITO thin films by Au implantation Followed by Gamma Irradiation

A.H. Sofi[1], M. A. Shah[1] and K. Asokan[2]

[1]Department of Physics, NIT-Srinagar, Jammu and Kashmir-190006, India
[2]Inter-University Accelerator Centre, Aruna Asaf Ali Marg, New Delhi - 110 067, India

Transparent conductive oxide thin films (TCO thin films) have provoked enormous interest due to their prospective applications in different fields because of their intriguing properties and structural diversity. Among these transparent conducting oxides, indium tin oxide displays superior performance and exceptional applications due to its good adhesion to substrates, chemical stability and photochemical properties resulting from its n-type highly degenerate semiconductive behavior and a wide band gap ranging from 3.5 – 4.3 eV upon miniaturizing it to the nanoscale, thereby significantly affecting its structural, morphological, topographical, optical and electrical properties [1-3].

50 keV Au ions were implanted into ITO thin films deposited on glass substrate to fluences of 5×10^{14}, 2×10^{15} and 5×10^{15} ions/cm^2. The films were then irradiated with 100 kGy gamma radiation using Co60 source. This implantation brings changes in the optical and electrical properties [3] which are of interest for various applications, such as transparent electrodes in ferroelectric photoconductor storage devices, photovoltaic cells, gas sensors when less conductive, liquid crystal displays, transparent electric heaters for aircraft windows, antistatic coating on instrument panels, coating electrodes in optoelectronic devices (flat panel displays), solar cells, photo-detectors, and electroluminescent devices [4-5].

The Au ion implanted films and irradiated with gamma radiation were characterized by various characterization techniques. XRD analysis demonstrates that both the films are polycrystalline and comprised of BCC cubical phase. Crystallite size decreases on implantation followed by irradiation. SEM analysis also demonstrates

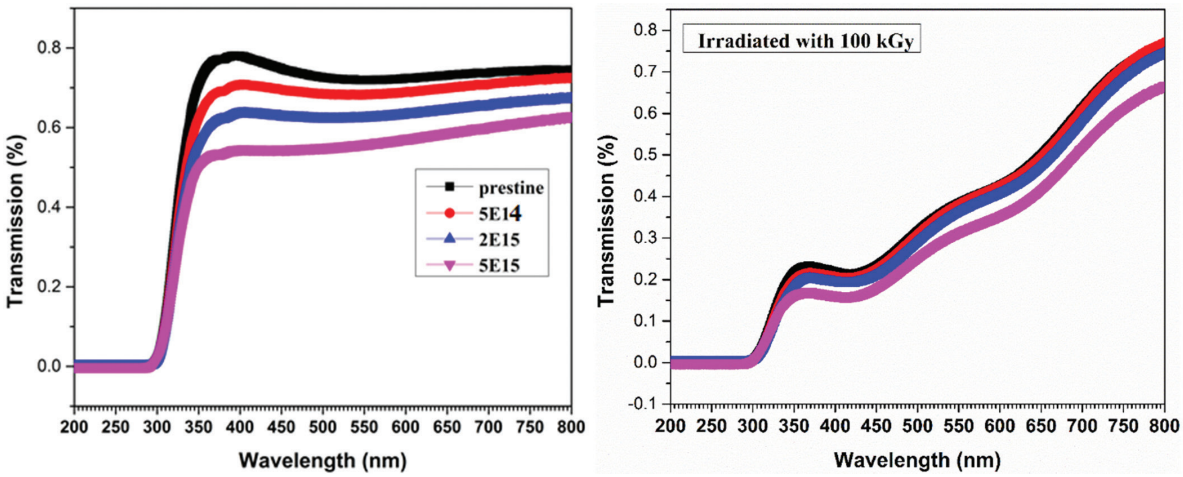

Figure: 1 (a) Transmission spectra of ITO thin films implanted with Au ions. (b. Transmission spectra of ITO thin films implanted with gold and irradiated with 100 kGy gamma radiation.

the variation in grain size with Au ion implantation followed by gamma irradiation. To evaluate the electrical properties ITO thin films, implanted and gamma irradiated, electrical measurements of the films were procured from van der Pauw-style Hall measurements (Ecopia Hall effect measurement system HMS-3000) at room temperature. The carrier concentration of the films increases by the order of 10 upon irradiation. Fig.1 shows the variation of transmission of implanted and gamma irradiated thin films in the 200-800 nm. The transmission of the films show a remarkable change in optical transparency after gamma irradiation. The transmission in implanted films decreases from 80-60% at 350 nm. The variation in transmission may be due to decrease in crystallinity and in increase in scattering effects. However, upon irradiation with 100 kGy gamma radiation the transmission lies in the range 25-15% as shown in figure 1(b). The variation in transmission upon gamma irradiation may be due to the bunching of gold nanoparticles in the thin films as visualized from AFM.

REFERENCES

[1] H. R. Fallah, M. Ghasemi, A. Hassanzadeh,Physica E 39 (2007) 69-74
[2] M. J. Alam, D. C. Cameron, Thin Solid Films 455 (2000) 377-378
[3] J. F. Smith, A. J. Aronson, D. Chen, W. H. Class, Thin Solid Films 469 (1980) 72
[4] K. Daoudi et al., Materials Science and Engineering C 21 (2002) 313–317
[5] B. J. Chen, X. W. Sun, B. K. Tay, Materials Science and Engineering B 106 (2004) 300-304

5.3 RADIATION BIOLOGY RESEARCH

5.3.1 High LET radiation induced effects on signaling pathways in human prostate cancer cell line

Pallavi Srivastava[1], Chandra Mohini Chaturvedi[1] and Asitikantha Sarma[2]

[1]Department of Zoology, Banaras Hindu University, Varanasi
[2]Radiation Biology Lab, Inter-University Accelerator Centre, New Delhi

High LET Radiation (Carbon Ion Radiation) has significant biological advantages and in combination with radiomodulators, may result in further enhancement in the efficiency as well as cost effectiveness. Radiomodulators are intended to enhance tumor cell death by altering one or more of the “5 Rs of radiotherapy”: Inherent cellular radiosensitivity, repair, reassortment, repopulation & reoxygenation.

In this study, we are trying to suppress the DNA repair process by using PNKP inhibitor A12B4C3 (A12B4C3, Sigma Aldrich) in Prostate cancer cell line (PC-3) which may enhance the radiosensitivity by accelerating the apoptosis (Kramer et al. 2006, Hunt et al. 2012). One of the important reason for the use of charged particle beam in tumour radiotherapy is that it can three dimensionally deliver a large dose to the tumor, and allow the sparing of surrounding normal tissues (Chatterjee et al. 2013).

Apoptotic bodies were observed under flurorescence microscope after staining with Prolong^{R} Gold Antofade reagent with DAPI as shown in Fig. (5.3.1A). % of apoptotic bodies were counted (approx. 150 cells at each dose) and represented as bar diagram in fig. 5.3.1B. Apoptotic body formation was significantly higher in cells which were treated with PNKP inhibitor in combination with carbon ion irradiation as compared to only C beam irradiated cells and control cells.

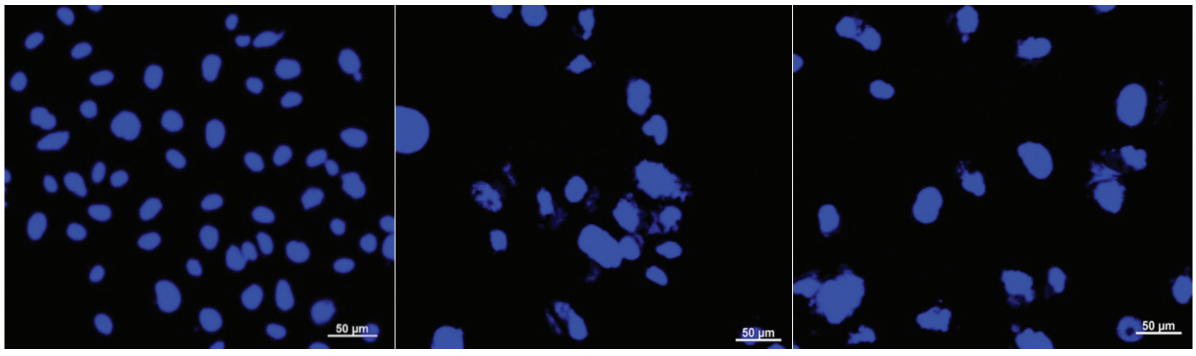

Control Cells | Radiation Dose (Gy) | Radiation Dose (Gy) + Treatment (µM)

Fig. 5.3.1A Morphological studies of apoptotic body formation by carbon ion irridiation and with PNKP inhibitor.

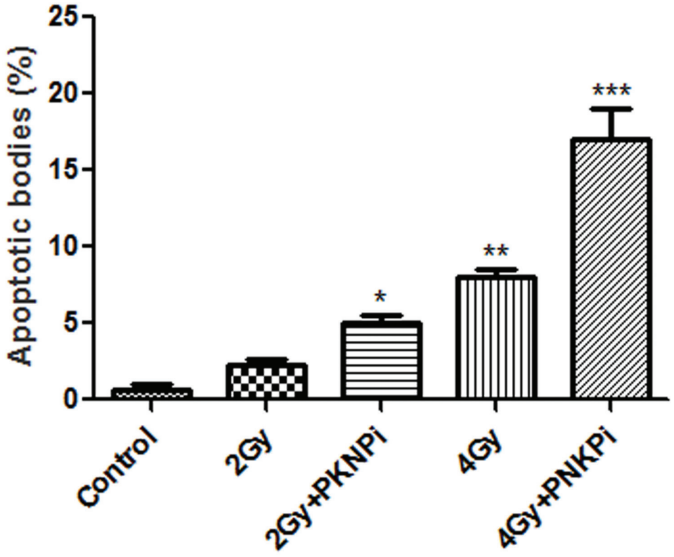

Fig. 5.3.1B % apoptotic bodies were counted randomly taking at least 150 cells at each dose group. *Bar diagram* represents apoptotic body increased in the presence of PNKP inhibitor as compare to control. Experiments in these graphs were done in triplicates, and similar results were obtained. The asterisks indicate significance of difference ***p<0.001, **p<0.01; *p<0.05 in comparison with control.

A distinctive feature of apoptosis is nuclear fragmentation and it is associated with the fragmentation of chromosomal DNA into multiples of the 180bp nuclesomal unit, known as DNA laddering. DNA ladder is hallmark of apoptosis. When irridiation dose (2Gy and 4Gy) is combined with PNKP inhibitor, a clear and more distinct ladder were formed as compared to control (fig. 5.3.2).

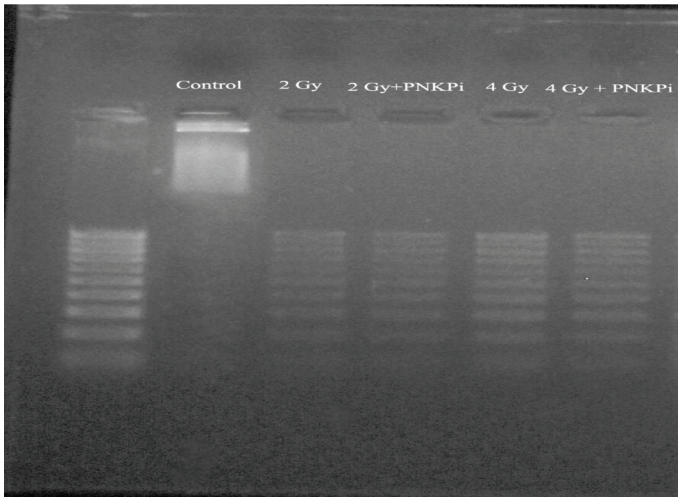

Fig. 5.3.2 Gel image of nucleosomal ladder assay formation after staining with ehidium bromide. Distinct ladders were formed when PC-3 cells were treated with Carbon ion irradiation in the presence of PNKP inhibitor as compared to control.

Prostate cancer cells (PC-3) exposed to carbon ion irradiation in the presence of PNKP inhibitor, a significant cell cycle arrest at G2/M phase was observed as compared to only C beam irradiated cells and control cells (Fig. 5.3.3).

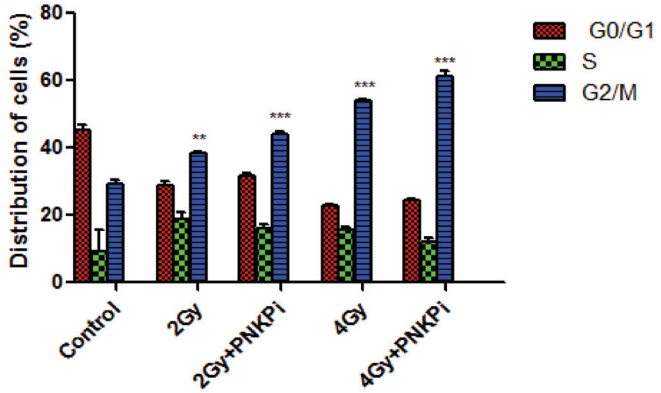

Fig. 5.3.3 Cell cycle arrest was examined by FACS. G2/M phase arrest was enhanced in PNKP inhibitor treated group as comapre with control cells. All experiments were done in triplicates and same result was found. The asterisks indicate significance of difference ***p<0.001, **p<0.01 in comparison with control.

Further, we are trying to investigate the pathway responsible for cell death, which is under investigation.

REFERENCES

[1] Chatterjee, P., Choudhary, G. S., Sharma, A., Singh, K., Heston, W. D., Ciezki, J., Klein, E. A., and Almasan, A. PARP inhibition sensitizes to low dose-rate radiation TMPRSS2-ERG Fusion Gene-Expressing and PTEN deficient prostate cancer cells. Plos One, 8:4, 2013.

[2] Hunt, C. R., Gupta, A., and Horikoshi, N. Does PTEN Loss Impair DNA Double-Strand Break Repair by Homologous Recombination? Clin Cancer Res., 18:920-922, 2012.

[3] Kramer, M.andScholz, M. Rapid calculation of biological effects in ion radiotherapy. Phys. Med. Biol., 51:1959-1970, 2006.

5.3.2 Investigation of DNA repair pathways and cross-talk between PARP-1 and p53 after carbon ion beam irradiation in cultured Human Cells

Priyanka Chowdhury[1], Asitikantha Sarma[2] and Utpal Ghosh[1]

[1]Department of Biochemistry & Biophysics, University of Kalyani, Kalyani 741235
[2]Inter-University Accelerator Center, Aruna Asaf Ali Marg, New Delhi 110067

High linear energy transfer (LET) carbon ion beam (CIB) is becoming one of the promising tools for killing tumors, especially radio-resistant tumors and deep seated tumors. It has been found to be more effective than gamma or X rays, because charged particles especially carbon ion beam deposits its maximum energy near the end of Bragg's peak, thereby keeping normal healthy cells at the entry point of the beam less affected. CIB has been found to be more effective than gamma radiation in producing DNA break and consequently cell death by apoptosis. DNA double stranded breaks (DSBs) are produced when cells are irradiated by high LET CIB. These DSBs are more deleterious than single strand breaks (SSBs) if they remain unrepaired. Basically, there are two double stranded break repair pathways in mammalian system namely classical non-homologous end-joining (C-NHEJ) and homologous recombination (HR). In C-NHEJ pathway, Ku70/80 heterodimer plays a crucial role by binding to the site of DSBs and thereby initiating repair process. There are several others essential proteins involved in C-NHEJ pathway which are activated and recruited to the breaking ends such as DNA-dependent protein kinase catalytic subunit (DNA-PKcs), XRCC4, XLF and ligase IV (Hefferin et. al. 2005). HR pathway is recruited by MRN (comprised of MRE11, Rad50 & NBS1) complex, along with the help of other essential proteins like CtIP, Exonuclease 1 (EXO1), nuclease/helicase DNA2, Rad51, Rad52, BRCA1. There is another DSBs repair pathway, known as called back-up NHEJ (B-NHEJ) or alternative end-joining (Alt-EJ) where ligase III, ligase I, XRCC1 and PARP-1 are involved.

In addition, carbon ion beam has been also used to effectively suppress the metastatic potential of cancer cells. Ogata et. al. 2005, have shown that CIB suppresses the potential of invasion, migration and adhesion to ECM in Fibrosarcoma cells. However, how this metastatic potential is being inhibited, what are the genes and proteins involved whose functions are altered in this suppression is still not clear. Here, we are taking an approach to study the mechanism underlying this metastatic suppression by treating cells with CIB in combination with PARP1 inhibitor.

- **Cell Proliferation assay:** Cells were irradiated with CIB in combination with or without PARP-1 inhibitor, DPQ in A549 cells. CIB irradiation was given at IUAC, New Delhi, in 15UD Pelletron using 85 MeV energy. The dose in Gray was calculated from the particle fluence using the following relation: Dose [Gray] = 1.6 X 10^{-9} X LET [keV/lm] X Fluence [particles/cm^2] X 1/density [gm/cc] (Ghorai et al. 2015). After 24 hours of incubation the irradiated cells were collected by trypsinization and 10^3 cells in culture medium with 10% FBS were seeded in 96 wells culture plates and incubated at 37°C. After 24, 48, 72 and 96 hours, 1mg/ml MTT were added and incubated at 37°C for another 4 hours. After incubation absorbance of the coloured formed after MTT addition was taken using Victor X5 (PerkinElmer).

- **Cell Migration assay:** A549 cells were grown in culture medium with 2% FBS and incubated at 37°C for 24 hours. After incubation, cells were irradiated with CIB with or withoutPARP-1 inhibitor. Following irradiation, cells were washed thrice with PBS and then 2 x 10^6 cells were seeded on the upper chamber ThinCert tissue culture insert multi-well plates containing serum free medium. The lower chamber of the plates was filled with 10% serum containing medium. The plates were incubated at 37°C for 16-20 hours. After incubation, cells migrated to the lower chamber were collected by trypsinization and counted using a hemocytometer.

- **RNA extraction and Q RT-PCR:** Total RNA was isolated from cells irradiated with CIB with or without PARP-1 inhibitor using TRIzol Reagent (Invitrogen; life technologies) following standard protocol. The RNA was treated with RNase free DNase (Sigma) for 1hr at 37°C to avoid the DNA contamination. cDNA was prepared from 1µg of RNA from all samples using M-MLV reverse transcriptase (NEB) and random hexamer (NEB). The quantitative PCR analysis was done on StepOnePlus™ Real-Time PCR System (Applied Biosystem; Life Technologies). Expression of MMP2 and MMP9 were done using SYBR green (Invitrogen).

Cell Proliferation assay & cell migration assay

We have compared cell proliferation of cells irradiated with CIB with and without PARP-1 inhibitor. We observed that cell proliferation ability was decreased with increase dose of CIB. Combined treatment of PARP-1 inhibitor and CIB reduced cell proliferation significantly as show in Fig 5.3.4. The migration was decreased significantly at each dose of CIB used as shown in Fig 5.3.4. We observed that only PARP-1 inhibitor (DPQ) treatment without any irradiation decreased migration significantly as shown in fig 5.5.5 and further CIB exposure along with DPQ showed synergistic reduction of cell proliferation.

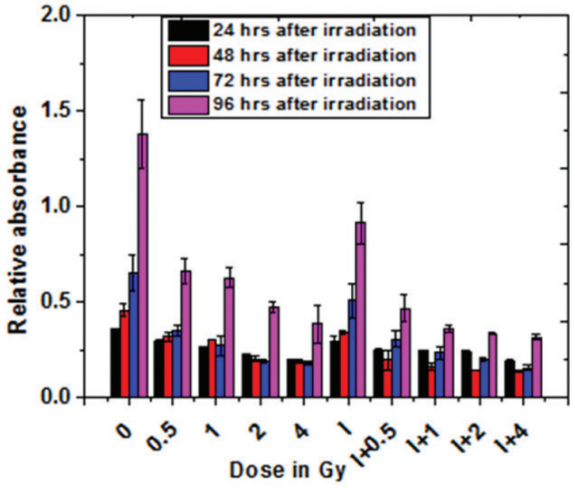

Fig. 5.3.4 A549 Cell proliferation ability after exposure with CIB in combination with PARP-1 inhibitor.

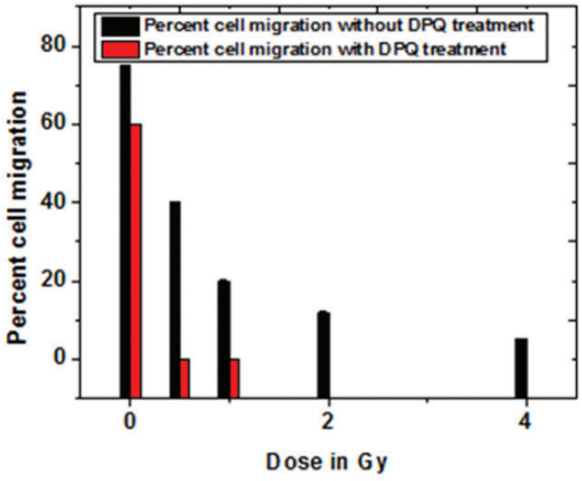

Fig. 5.3.5 Percentage cell migration with and without DPQ treatment.

Cell migration assay:

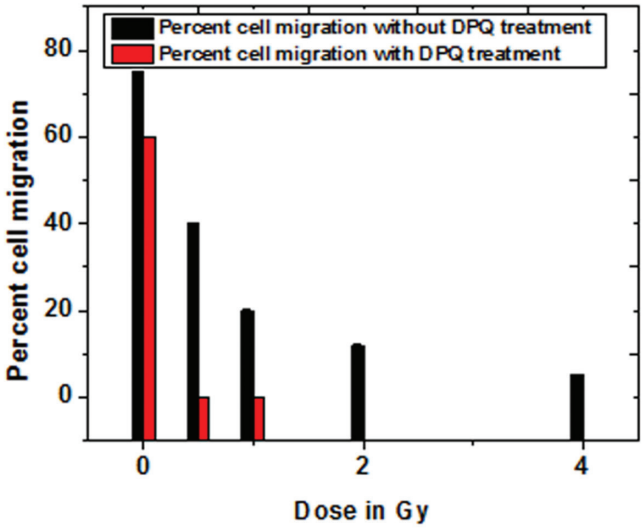

Fig. 5.3.6 A549 cell migration percentage was determined after CIB exposure with or without DPQ treatment

Expression of MMP2 and MMP9 genes:

Matrix-metalloproteinases (MMPs) play critical role in metastasis and cell migration. So, we monitored expression of MMP-2 and MMP-9 after CIB exposure with and without PARP-1 inhibition. We observed that both MMP-2 and MMP-9 were down-regulated dose-dependently with CIB as shown in Fig 5.3.6. Only PARP-1 inhibitor was capable of reducing expression of MMPs and further CIB exposure reduced more. This data implicates that combining PARP-1 inhibitor with CIB gives promising result in controlling highly metastatic cancer cells like A549.

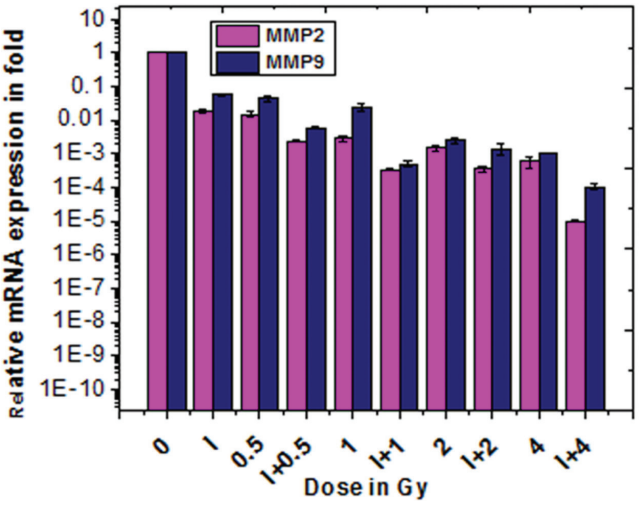

Fig. 5.3.6 MMP2 and MMP9 expression was studied after CIB irradiation in combination with PARP-1 inhibitor, DPQ. Here 'I' designates the inhibitor concentration of 1μM and I+0.5 designates CIB irradiation with a dose of 0.5 Gy in combination with 1μM DPQ.

5.4 ATOMIC PHYSICS RESEARCH

5.4.1 Problem with theoretical calculation for charge state distributions for ion-solid collisions at low energies

D. K. Swami and T. Nandi

Inter University Accelerator Centre, Aruna Asaf Ali Marg, New Delhi 110067

The ab initio theory such as ETACHA23 code [1] has been developed to estimate the evaluation of the whole charge state distribution of the projectile ions colliding with the solid target. However, this code exhibits often

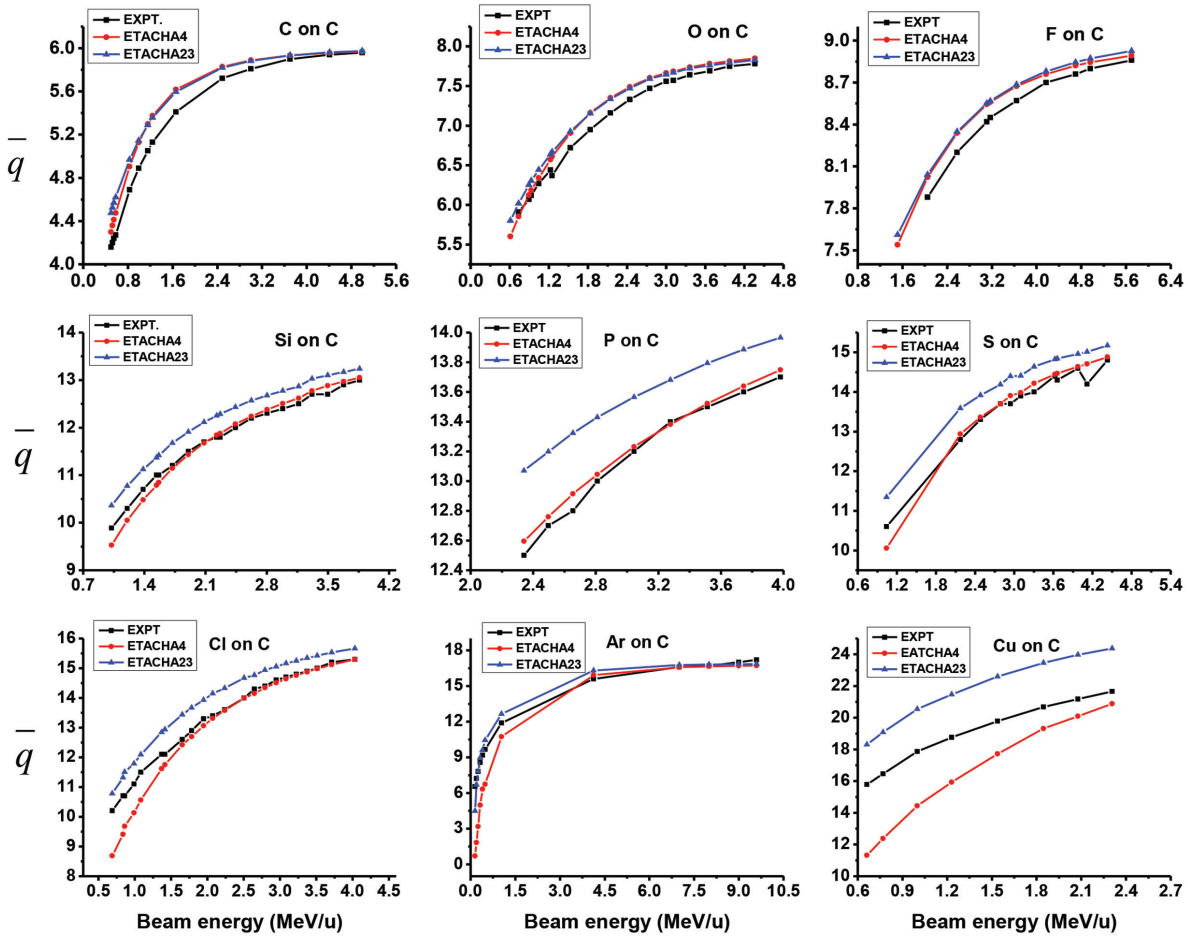

Fig. 5.4.1: Mean equilibrium charge state $\bar{q}$ vs beam energy plot fors different projectiles on the carbon target. Experimental data are taken from [3]. Solid lines are just to guide the eye.

disagreement with the experimental results in the low energy side. In order to circumvent this problem, this code has been extended as ETACHA4 code [2] to have better results in the low energy regime < 10 MeV/u. On the other hand, many experimental studies for the projectiles up to 20 electrons on the carbon target are available. For such projectile ions both the codes can be used. Hence, we compare the experimental results for equilibrium charge state $\bar{q}$ with the predictions of ETACHA23 as well as ETACHA4 in Fig. 5.4.1 to address the current scenario. It is clear from the figure that the ETACHA23 and ETACHA4 estimates agree with each other very well for the projectiles C, O and F, but slightly higher than the experimental data. However, the ETACHA4 predictions start deviating from the ETACHA23 for Si onwards; whereas, the ETACHA4 predictions represent well the experimental data for Si, P and S. Nevertheless, the predictions underestimate the measurements from Cl onwards. In contrast, ETACHA23 data remain little higher than the measured data.

Besides the electron capture processes in the bulk of the foil, certain electron capture processes occur at the exit surface of the foil [e.g. [4]], which can alter every charge state produced in the bulk. Consequently, the charge distribution may shift towards the lower charge states. However, the electron capture processes at the exit surface is not included in the ETACHA codes. As a result the theoretical results ought to be higher than the experimentally observed data as seen in the results of C, O and F projectiles. Nevertheless, in no case theoretical data cannot be less than the measured values that we see in the case of Cl, Ar and Cu. Rather, in these cases ETACHA23 predictions are still higher and that trend is physically possible.

Only difference between the theoretical approaches in ETACHA23 and ETACHA4 is that the former makes use of the plane–wave Born approximation (PWBA) for accounting the ionization and excitation processes; whereas the later applies continuum distorted-wave-eikonal initial state (CDW-EIS) approximation [e.g. [5]]was applied for obtaining the ionization cross sections and the symmetric eikonal (SEIK) model [e.g. [6]] for the excitations cross sections. Hence, CDW-EIS and SEIK certainly underestimate the ionization and excitation cross section, respectively.

REFERENCES

[1] J.P. Rozet, C. Stéphan and D. Vernhet, Nucl. Instrum. Methods Phys. Res., Sect. B**107,** 67 (1996).
[2] E. Lamour, P. D. Fainstein, M. Galassi, C. Prigent, C. A. Ramirez, R. D. Rivarola, J. Rozet,M. Trassinelliand D. Vernhet,Phys. Rev. A**92,** 42703 (2015).
[3] K. Shima and T. Mikumo,At. Data And Nucl. Data Tables **34,** 357 (1986).
[4] M. Day and M. Ebel, Phys. Rev. B**19,** 3434 (1979).
[5] P.D. Fainstein and V.H. Ponce, Phys. Rev. A**36,** 3939 (1987).
[6] G.H. Olivera, C.A. Ramirez, and R.D. Rivarola, Phys. Rev.A**47,** 1000 (1993).

5.4.2 A parameterized model for Coulomb barrier height

D. K. Swami and T Nandi

Inter University Accelerator Centre, Aruna Asaf Ali Marg, New Delhi 110067

The basic characteristics of nuclear reactions are usually described by an interaction consisting of a repulsive Coulomb potential term and a short range attractive nuclear potential term. The resultant potential is a function of the distance between the centres-of-mass of the target and projectile, and it possesses a maximum at a certain distance that works as a barrier for the projectile ions going to shorter distances. This is referred to the Coulomb barrier, which is a basic parameter in describing the nuclear reactions. The kinetic energy of the projectile must be adequate to overcome this barrier in order to enter a pocket at the adjacent to the barrier at a shorter distance, where the nuclei undergo nuclear fusion processes. The barrier is determined by the excitation function measurement of nuclear fusion [1], whereas it is estimated by many theoretical models such as Bass potential model [[2],[3]], Proximity potential model [4], Double folding model [5], Wood Saxon potential model [6] and semi empirical models such as Christenson and Winther model [7], Broglia and Winther model [8], Aage Winther model [9], Denisov potential model [10], Siwek-Wilezyniska and Wilezyniski model [11], Skyrme [12]. On the other hand, many experiments also exist in the literature for the measurements of the Coulomb barrier and interaction barrier using the nuclear fusion and quasi elastic (QE) scatterings. In this work, we have plotted the Coulomb barriers from the fusion reaction experiments [e.g. [13]] alone and the interaction barriers from the QE scattering experiments [e.g. [14]] alone as a function of a dimensionless parameter $z = \frac{Z_p Z_t}{\left(A_p^{\frac{1}{3}} + A_t^{\frac{1}{3}}\right)}$ as shown in Fig.5.4.2. The curves have been fitted with polynomial functions to obtain an empirical formula for estimating each barrier. The empirical formula for the fusion barrier is

$B_{fu} = -1.157 + 0.717 * z + 0.003 * z^2 + 4.560 \times 10^{-6} * z^3; \quad 8 \leq z \leq 278$

and that for the interaction barrier is

B_{int} = -14.800 + 1.302 ∗ z - 0.002 ∗ z^2 + 4.770 × 10^{-6} ∗ z^3; 59 ≤ z ≤ 313

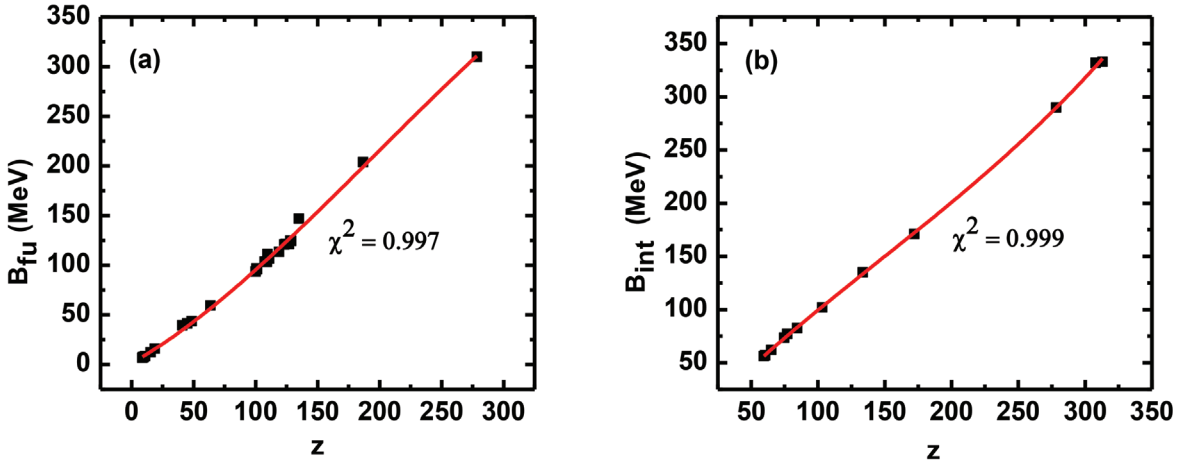

Fig.5.4.2 (a) Fusion barrier and (b) interaction versus dimensionless parameter z.

The comparison of the empirical results so obtained with the predictions from the various models available provides the merits of our formulae over the others. However, this formula is limited within the bounds where experimental data do exist. We noticed that fusion measurements are required for the heavy systems z > 278 and QE measurements are needed for the light z < 59 and heavy systems z > 313.

REFERENCES

[1] B. B. Back, H. Esbensen, C. L. Jiang, and K. E. Rehm, Rev. Mod. Phys. **86,** 317 (2014).
[2] R.Bass, Nucl. Phys. A**231,** 45 (1974).
[3] R. Bass, Phys. Lett. **47B,** 139 (1973).
[4] J. Blocki, J. Rundrup, W.J. Swiatecki and C.F. Tsang, Annals of Phys. **105,** 427 (1977).
[5] G. R. Satchler and W.G. Love, Phys. Reports **55,** 183 (1979).
[6] Roger D. Woods and David S. Saxon, Letter to Editors, (1954).
[7] P. R. Christensen and A. Winther, Phys. Lett. **65B,** 19 (1976).
[8] W. Reisdorf, Nucl. Part. Phys. **20,** 1297 (1994).
[9] A. Winther, Nucl. Phys. A **594,** 203 (1995).
[10] I. Dutt and R. K. Puri, Phys. Rev. C **81,** 044615 (2010).
[11] K. Siwek-Wilezynska and J. Wilczynski, Phys. Rev. C **69,** 024611 (2004).
[12] V. Zanganeh, M. Mirzaei and N. Wang, Commun. Theor. Phys. **64,** 177 (2015).
[13] P. Sperr, T.H. Braid, Y. Eisen, D.G. Kovar, F.W. Prosser, J.P. Schiffer, S.L. Tabor and S.Vigdor, Phys. Rrv. Lett. **37,** 321 (1976).
[14] S. Mitsuoka, H. Ikezoe, K. Nishio, K. Tsuruta, S. C. Jeong, and Y. Watanabe, Phys. Rev. Lett.**99,** 182701 (2007).

5.4.3 Line shape technique: A tool for impact parameter dependent investigations in ion-atom collisions

Sarvesh Kumar[1], D.P. Goyal[1] and T. Nandi[2]

[1]Indira Gandhi University, Meerpur, (Haryana) India.
[2]Inter University Accelerator Center, New Delhi India.

An impact parameter dependent investigation has been a proven key for understanding many fundamental processes in ion-atom collisions since decades. In order to determine the impact parameter dependent probability P(b) of a certain dynamic process, either x ray and particle coincidence for large impact parameters and line shape method for small impact parameters are used [1]. In heavy ion-atom collisions, the width of a line depends on three factors: detector resolution, blending of satellite line and other unresolved lines, and Doppler effects. The Doppler shifted x ray energy E_x in the lab system is given by

$$E_x = E_{xo} \frac{[1-(v_{cm}/c)]^{1/2}}{1-(v_{cm}/c)\cos\alpha} \quad (1)$$

$$\cos\alpha = \cos\psi \cos\theta + \sin\psi \sin\theta \cos\phi \quad (2)$$

Where E_{xo} = photon energy in the rest frame, v_{cm} = center of mass collision velocity, α = observation angle with respect to the direction of the recoiled target atom, ψ = Recoil angle of the target atom in the lab system with respect to the direction of the projectile ions, θ = detector angle with respect to the direction of the projectile ions, and ϕ = azimuthal angle of the recoiled target atom. According to Rutherford scattering formula, the impact parameter is as follows

$$b = \alpha_0 \cot(\theta_{cm}/2) \quad (3)$$

Where θ_{cm} = projectile scattering angle in center of mass frame and α_0 = half the distance of closest approach in head on collisions as given below

$$\alpha_0 = \frac{Z_1 Z_2 e^2}{2E_{cm}} = \frac{Z_1 Z_2 e^2}{2E_2}, \frac{A_1 A_2}{A_2} \quad (4)$$

Impact parameter dependent investigations using the line shape method were first reported by Greenberg et al.[2]. Kinematic analysis of Doppler Broadened x ray lines was used to determine the impact parameter dependence of the probability for K shell vacancy production in heavy-ion collision systems for b ≤ 40 fm. Doppler shift is given by

$$\Delta E_x = E_{xo} \frac{v_{cm}}{c}[1 + (-1)^{i+1} K_i \cos\theta_{cm}) \quad (5)$$

Where, v_{cm} = center of mass velocity and $K_i = A_i/A_2$; i = 1, 2, for projectile and target, respectively. Supposing $\theta_{cm} = \theta$ and using trigonometric relations, we get

$$\cot(\theta/2) = \sqrt{(1 + \cos\theta) / (1-\cos\theta)} \quad (6)$$

Equation (3) can be written as

$$\cot(\theta/2) = b/\alpha_o \quad (7)$$

Using equation (6) and (7)

$$cos\theta \quad \frac{b^1-\alpha_o^2}{b^2-\alpha_o^2} \quad (8)$$

Substituting equation (8) in equation (5), we get Doppler shift as a function of impact parameter b as below

$$\Delta E_x = E_{xo} \frac{v_{cm}}{c}[1 + (-1)^{i+1} \left(\frac{b^2-\alpha_o^2}{b^2+\alpha_o^2}\right)] \quad (9)$$

Substituting , we get

$$\Delta E_x = \beta E_{xo} [1 + (-1)^{i+1} K_i \left(\frac{b^2-\alpha_o^2}{b^2+\alpha_o^2}\right)] \quad (10)$$

Hence, x ray line shifts observed in such collisions can be used to investigate impact parameter dependences of collision dynamics[3].

I. Case of projectile x ray lines: i=1; $K_i = A_i/A_2 = A_1/A_2$; on substituting these values in equation (10), Doppler shift turns out to be as follows

$$\Delta E_x = E_{xo} \frac{v_{cm}}{c}[1 + \frac{A_1}{A_2} \left(\frac{b^2-\alpha_o^2}{b^2+\alpha_o^2}\right)] \quad (11)$$

Equation (11) can be written as

$$b^2 = \frac{\alpha_o^2 [\beta E_{xo}(A_1-A_2) + \Delta E_x A_2]}{\beta E_{xo}(A_1+A_2) + \Delta E_x A_2} \Longrightarrow b = \alpha_o \sqrt{\frac{[\beta E_{xo}(A_1-A_2) + \Delta E_x A_2]}{\beta E_{xo}(A_1+A_2) + \Delta E_x A_2}} \quad (12)$$

II. Case of target x ray lines: i=2 , $K_i = A_i/A_2 = A_2/A_2$ =1; substituting these values in equation (10) we get the Doppler shift ΔE_x of target x ray line in terms of impact parameter b as

$$\Delta E_x = \beta E_{xo} [1 - \left(\frac{b^2-\alpha_o^2}{b^2+\alpha_o^2}\right)] \quad (13)$$

Equation (13) can be written as

$$b^2 = \frac{\alpha_o^z [2\beta E_{xo} - \Delta E_x]}{\Delta E_x} \Longrightarrow b = \alpha_o \sqrt{\frac{[2\beta E_{xo} - \Delta E_x]}{\Delta E_x}} \quad (14)$$

Obviously, b is a function of ΔE_x and thus the general form of the line shape [ ] can be given by

$$\frac{d[N(\Delta E_x)]}{d(\Delta E_x)} = \frac{2\pi c}{E_{xo} v_{cm} K_i} P[b(\Delta E_x)] \frac{\alpha_o^z}{4} \left[1 + \left(\frac{b(\Delta E_x)}{\alpha_o}\right)^2\right]^2 \left(\frac{E_x}{E_{xo}}\right)^2 \xi(E_x) \qquad (15)$$

Where $\xi(E_x)$ = photon frequency response of the detector[4] at $E_{xo}+\Delta E_x$. By putting equation (12) in equation (15), we get the line shape equation[5] for the case of projectile x rays and equation (14) in equation (15) for target x-ray lines. Left hand side is obtained from derivative of the observed spectrum and thus only unknown quantity left with $P[b(\Delta E_x)]$ can be determined as a function of $b(\Delta E_x)$

REFERENCES

[1] P.H. Moklar and D. Liesen, Progress *in Atomic Spectroscopy Part* C. Springer Verlag, 1984.
[2] J. S. Greenberg et al., Phys. Rev. Lett. 39, 1404 (1977).
[3] W. Greiner, B. Müller, and J. Rafelski, "Quantum Electrodynamics of Strong Fields," vol. 219, 1985.
[4] K. J. Chun, S. H. Hah, H. M. Kim, and G. H. Yoo, *J. Radiat. Res.* 47, 27 (2006).
[5] D. Schwalm et al., Nucl. Physics A 192, 449 (1972).

5.4.4 Alignment and Orientation Effects in Ionisation of Small Molecules

Bhas Bapat[1], Deepak Sharma[1], C P Safvan[2] and Pragya Bhatt[2]

[1]Indian Institute of Science Education and Research Pune, Homi Bhabha Road, Pune – 411008
[2]Inter University Accelerator Centre, Aruna Asaf Ali Marg, New Delhi – 110067

Since molecules are not spherically symmetric, the outcome of a collision between an ion and an atom should depend on the alignment of the molecule with the direction of the projectile [1,2]. Although gas molecules are randomly oriented in space, it would be possible to determine their orientation from backward reconstruction of the momenta of the fragments resulting from the dissociative ionisation process, especially in the case of diatomic molecules. It should be noted that for homonuclear diatomics, alignment, but not orientation, is a meaningful parameter, while for heteronuclear diatomics, orientation is a meaningful parameter. Orientation effects are quantified in terms of the β parameters in the angular distribution of the fragment ions $N(\theta) = N_0 [1+ \beta_1 P_1(\cos\theta) + \beta_2 P_2(\cos\theta)] \sin\theta$, where θ is the angle with respect to the projectile velocity. For isotropic fragmentation, both β_1 and β_2 are zero, while for homonuclear diatomics, β_1 is zero.

We have performed experiments to study the effect of alignment on the dissociative ionisation of small molecules under the impact of ions of varying charge and velocity. The experiment consists of an ion beam colliding with a jet of molecules under single collision conditions. Collision products (ions and electrons) are analysed by a combination of coincidence momentum imaging of ions based on time-of-flight and position of arrival detection of ions, triggered by the detection of the electron(s) ejected in the ionisation event. Ion detection is done using a large area position resolving microchannel detector with a delay line anode. The post-collision analyser allows separation of electron capture and direct ionisation channels. Experiments have been performed using protons, argon and xenon ions of different charge *(q)* and velocities *(v)*. In terms of the perturbation strength *q/v*, our experiments span the weak, intermediate and strong perturbation regimes, $0.1 < q/v < 24$ (in atomic units).

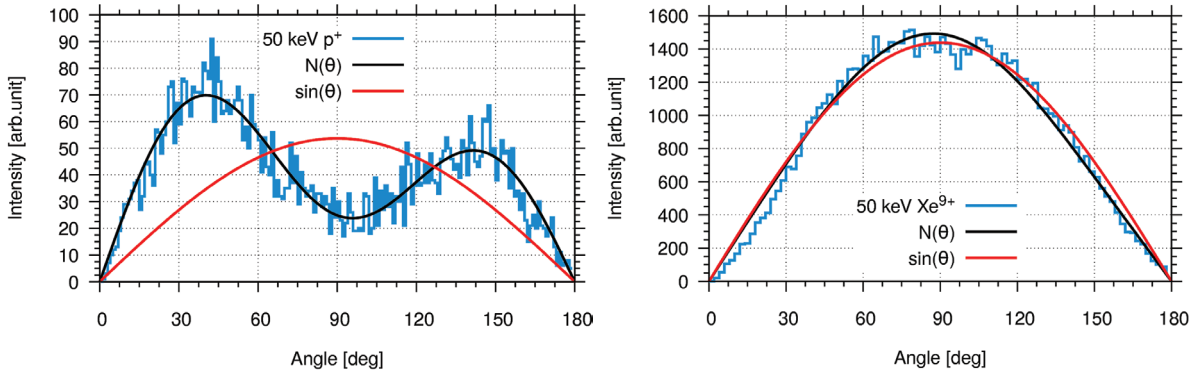

Fig. 5.4.3 Angular distributions of fragments arising from CO^{4+} formed by ion impact on CO: [*above,* 50 keV p+] strong anisotropy and orientation effect, [*below,* 50 keV Xe^{9+}] near isotropy.

Our results show that by-and-large, for weak perturbations orientation effects are strong even for low ionisation states, while for strong perturbations, the orientation effects are weak, even though the ionisation probability itself is higher. Some of the features are in agreement with previous predictions [3].

REFERENCES
[1] B. Siegmann et al., Physical Review A **65** 010704R (2001)
[2] C. Caraby et al., Physical Review A **55** 2450 (1997)
[3] Z. Kaliman and N. Orlić, Phys. Rev. A **65** 012708 (2001)

5.5 ACCELERATOR MASS SPECTROMETRY

5.5.1 AMS ^{14}C dating of Deep sea marine core sediments from eastern part of Arabian Sea to reconstruct paleoclimate

Neelavannan Kannaiyan[1], S.M. Hussain[1], S. Balakrishnan[2], Pankaj Kumar[3] and S. Chopra[3]

[1]Department of Geology, University of Madras, Chennai, Tamil Nadu- 600 025, India
[2]Department of Earth Science, Pondicherry University, Puducherry 605 014, India
[3]Inter-University Accelerator Centre, Aruna Asaf Ali Marg, New Delhi 110067, India

Continental margin's shelf and slope are very active oceanic regions. Those of the eastern Arabian Sea, namely west coast of India experience seasonally changing monsoon driven-coastal circulation, upwelling, river discharges, anthropogenic inputs etc [1]. Lithogenic material to the Arabian Sea is received through many sources of aeolian and fluvial nature [2]. Arabian Sea circulation strongly influenced by southwest monsoon in summer (June-September) and northeast in winter monsoon (December - February). The intermediate waters ~200 to ~1000 m. of the eastern Arabian Sea are perennially anoxic and intense denitrification is reported in the area north of ~ 15˚N [3] [4]. The present study has been undertaken in selected areas of shelf and slope region of eastern part of the Arabian Sea, to delineate the past climate and paleoenvironmental changes and to establish a precise chronostratigraphy.

Two core sediment samples GC1 and GC2 were collected using a gravity core sampler from off Lakshadweep islands and off Goa during 2015 by the Ministry of Earth Sciences, research vessel Sagar Kanya, The water depths of these two sampling locations are 2057 m and 517 m, respectively. Based on the total organic carbon (TOC) value we have selected organic rich sediments out of which six samples were dated using AMS under the supervision of radiocarbon team of IUAC, New Delhi. The data will be processed to reconstruct oceanographic changes during the Mid Pleistocene to Holocene that includes last glacial maximum (LGM), deglacial and warm periods.

REFERENCES
[1] Krishnaswami, S., Nair, R.R. (Eds.) 1996. JGOFS (India). Current Science 71, 831-905.
[2] Sirocko, P. and H. Lange, Clay-mineral accumulation rates in the Arabian Sea during the late Quaternary. Marine Geology, 97, 105-119, (1991).
[3] Naqvi SWA. Denitrification process in the Arabian Sea. Proc. Indian Acad. Sci, 103, 279 – 300 (1994).
[4] B.L.K. Somayajulu, R. Bhushan, Ashish Sarkar, G.S. Burr, A.J.T. Jull., Sediment deposition rates on the continental margins of the eastern Arabian Sea using 210Pb, 137Cs and 14C. The Science of the Total Environment, 429 – 439, (1999).

5.5.2 Developing chronological constraints tectonic and climate events in different parts of the Himalaya

C. P. Rajendran[1], Jaishri Sanwal[1], Biju John[2], Kusala Rajendran[3], Pankaj Kumar[4], S. Chopra[4] and K. Anandasabari[1]

[1]Jawaharlal Nehru Centre for Advanced Scientific Research, Bengaluru 560064 India
[2]National Institute of Rock Mechanics, Kolar Gold Fields 563117 India
[3]Indian Institute of Science, Bengaluru 560012 India.
[4]Inter-University Accelerator Centre, New Delhi 110067 India

The Himalayan Mountains, a product of India-Asia collision, is not only the locus of devastating earthquakes but also influences the northern-hemisphere atmospheric circulation and also obstruct the path of the north mid-latitude cold winds owing to its altitude and location. Indian Summer Monsoon (ISM) and Western Disturbances (WDs) are the two main components in Himalayan region. The tectonic and climate together plays an important role to reshape the Himalayan belt.

The last few decades has been witnessed for number of great earthquakes (M>8.0) like the 1934 Bihar-Nepal and the 1950 Upper Assam had devastating impact on the mountainous and alluvial part of the region. The

potential threat of great earthquakes events are the major scientific and societal concern. Two major issues stand out with respect to the Himalayan earthquake sources one, the maximum magnitude earthquake that can be expected, and two, the recurrence pattern of great earthquakes. Our current studies are targeted to resolve these questions which are central to evaluating seismic risk in the Himalaya. We have generated chronological database on the fault displacements from various locations along the Main Frontal Thrust (MFT) in the central Himalaya to understand the last major earthquake and its extent of rupture zone. The evidence suggests a major gap-filling earthquake in 14th century A.D. in the central Himalaya. Further work is ongoing.

The high altitude lakes are extremely sensitive to climate change and provide a promising tool for evaluating past ecosystem with respect to climatic and environmental changes. In such regions the duration of snow cover in the lake and catchment area, which is closely related to temperature, precipitation and solar radiation highly influence the physical, chemical and biological properties of the ecosystems. The proxy indicators, such as diatoms reveals the history of past ecosystem responses to climatic and environmental changes. Here we present the results obtained from the sediment core of Wular Lake using Scanning Electron Microscope in order to identify the siliceous microfossils (diatoms) and Pinus species with higher reliability to reconstruct the Holocene ecological and vegetation history of Wular Lake in the last ~3,000 yrs. The results indicate a wide variety of diatoms in the core sediment at different depths, which providing with more detailed insight into what factors determine the structure of diatom assemblages in the Wular Lake through various time segments determined by radiocarbon dates.

5.5.3 AMS Radiocarbon Dating of two sediment cores from the Great Rann of Kachchh

Abhishek Kumar

Department of Geology, The M. S. University of Baroda, Vadodara-390002.

The Great Rann of Kachchh is a marginal marine basin in western India that dried up in the late Holocene. The basin was filled by mainly Himalayan sediments brought by the now extinct Saraswati River (Khonde et al., In press). The present study comprised AMS radiocarbon dating of the two cores (60 m and 50 m in length) obtained from the Great Rann (Maurya et al., 2013). The purpose of the study was to obtain high resolution chronology of the cores to understand the sedimentation pattern and delineate the paleoenvironments. A total of 30 bulk sediment samples (17 from Dhordo core and 13 from Berada core) were selected for AMS dating which carried out in April, 2017.

The AMS dating was carried out under the supervision of Radiocarbon team of IUAC, New Delhi. The samples were dried at 50 °C and were hand crushed to make unconsolidated sediments, the samples were then analyzed under microscope for making them free of any rootlets this was done considering the fact that inclusion of any such material will give the recent age or will lower the average age of samples. Samples were weighted to around 10-15 grams which were treated through ABA (Acid Base Acid) HYDROCHLORIC ACID (HCl) concentration 10% and Base SODIUM HYDROXIDE (NaOH) which was used to remove the carbonate from the samples and only organic carbon was used for the dating after every time the samples went through treatment they were centrifuged and the precipitated samples were collected and the supernatant were discarded. They were neutralized with distilled water till the ph reached neutral 7. The process was repeated every time they were treated through ABA process. The samples were dried and used for the preparation of small samples which were used as target samples by the use of 'boats'. The target prepared was then loaded in the instrument called AGE. Firstly the carbon content were analysed and based on content of carbon the weight of the sample to be taken for the dating in AGE were determined. Minimum 1000 µg of carbon was taken. The carbon was collected in the tube attached to the AGE and the tube was then loaded in the Accelerator which fetched data. The data provided is being analysed further in conjunction with the sedimentary characteristics, sea level changes and palaeoenvironmental changes.

REFERENCE

[1] Maurya D.M., Khonde N, Das Archana, Chowksey V. and Chamyal., L. S., Subsurface sediment characteristics of The Great Rann of Kachchh, Western India based on preliminary evaluation of textural analysis of two continuous sediment cores ,Current Science, 104 (2013) 1071-1077.

[2] Khonde N., Singh, S. K., Maurya, D. M., Rai, V. K., Chamyal, L. S. and Giosan, L., Tracing the Vedic Saraswati in the Great Rann of Kachchh. Scientific Reports, 7 (2017) 5476.

5.5.4 Chronology development for the Late Quaternary vegetation and climate reconstruction of the Himalayan region

Parminder Singh Ranhotra and Ipsita Roy

Birbal Sahni Institute of Palaeosciences, 53, University Road, Lucknow - 226007

For the reconstruction of past vegetation and climatic changes from the Himalayan region based on various organic and inorganic proxy analysis of the subsurface sediments, the absolute dates play an important role as they provide chronology to the climatic sequences. Here we are able to provide chronology to our studied subsurface sediment profiles by the 14_C dates generated by the accelerated mass spectrometry (AMS) method from the Inter University Accelerator Center (IUAC), New Delhi.

A total of 30 samples were processed for the dating that comprised of peat and organic rich sediments collected at various depths within different subsurface sedimentary profiles from the Dokriani and Gangotri glacier valleys of Uttarakhand, western Himalayan region. The samples were processed by crush drying the samples followed by the acid-base-acid method to remove the unwanted inorganic carbonate and humus. These samples were treated with acid-base-acid to remove the inorganic carbonates and humic acid. Finally the samples were washed using the milliqu water to get rid of the acid effect. To remove the moisture totally from the sediments the washed samples were the freeze-dried overnight. The dried samples were finally graphitized in the Elementary auto-sampler and graphitizer. Amongst the 30 processed samples, few samples with negligible amount of organic carbon could not be successfully graphitized. The graphitized samples were loaded in the cathode wheel for their measurement in the mass accelerator. The sample pre-treatment, graphitization and measurement of the AMS C-14 ages are done at the AMS lab of Inter-University Accelerator Centre (IUAC), New Delhi.

The ^{14}C (AMS) dates thus produced from IUAC has enabled to provide chronologies to the past climatic episodes in the Himalayan areas studied. These sediments have also been studied for other climate proxies' viz. Pollen, stable carbon isotopes and magnetic susceptibility. The various proxy analysis along with the provided time-frame would help in understanding the temporal vegetation and climatic changes of the western Himalayan region and can also be correlated with the glacial episodes of the area.

Table 1: Sampling locations with the AMS C-14 dates

Sr. No.	Sampling site	No. of samples Dated	Age range covered in years BP
1	One sedimentary profile from Nachiketa area at 2500 m amsl in Uttarakhand	3	Late Holocene time (~3,000 to recent)
2	Two sedimentary profiles from Dokriani glacier valley at 3500 m amsl in Uttarakhand	16	Late Pleistocene to Holocene (~14000 to recent)
3	One sedimentary profile from Gangotri glacier valley at 4000 m amsl in Uttarakhand	3	Mid to late Holocene (~4352 to recent)
4	One sedimentary profile Central Tibet	4	Late Holocene (~2769 to recent)